

**Thermal transport properties of selected
ferroelectrics, mixed valance perovskites and
dielectric ceramics using photopyroelectric
technique**

Thesis submitted to
COCHIN UNIVERSITY OF SCIENCE AND TECHNOLOGY
in partial fulfillment of the requirements
for the award of the degree of
DOCTOR OF PHILOSOPHY

Manjusha M.V.

**Department of Instrumentation
Cochin University of Science and Technology
Cochin-682022, Kerala, India**

May 2008



CERTIFICATE

Certified that the work presented in this thesis is based on the bono fide work done by Ms. Manjusha M. V. under my guidance in the Department of Instrumentation, Cochin University of Science and Technology, as has not been included in any other thesis submitted previously for the award of any degree.

Cochin – 682022

30th May 2008



A handwritten signature in black ink, appearing to read "Dr. Jacob Philip".

Dr. Jacob Philip

Supervising Guide
Dr. Jacob Philip


DIRECTOR

Sophisticated Test and Instrumentation Centre
Cochin University of Science & Technology, Cochin-682 022

DECLARATION

Certified that the work presented in this thesis is based on the original work done by me under the guidance of Dr. Jacob Philip, Director, Sophisticated Test and Instrumentation Centre (STIC) Cochin University of Science and Technology, as has not been included in any other thesis submitted previously for the award of any degree.

Cochin – 682022
30th May 2008


Manjusha M.V.

Dedicated to My Dearest Mother

Contents

<i>Preface</i>	<i>i</i>
<i>Acknowledgements</i>	<i>I</i>
Chapter 1: Photothermal techniques to measure thermal properties of solids	
1.1 Introduction	1
1.2 Photothermal spectroscopy methods	7
1.2.1 Photoacoustic Spectroscopy	11
1.2.2 Photothermal Deflection	14
1.2.3 Photothermal Interferometry	16
1.2.4 Photopyroelectric Effect	18
1.2.5 Theory of Photopyroelectric Effect in Solids	27
1.3 Applications of photopyroelectric spectroscopy	41
1.3.1 PPE Spectroscopy in Semiconductors	41
1.3.2 PPE Spectroscopy in Paramagnetic and Ferromagnetic Materials	42
1.3.3 PPE Spectroscopy in Liquid Crystals	43
1.3.4 PPE Spectroscopy to Investigative Ferroelectric Phase Transitions	44
1.3.5 PPE Gas Sensors	45
1.4 Work Presented in the Thesis	46
References	47
Chapter 2: Experimental Methods	
2.1 Introduction	56
2.2 Photothermal Methods	59
2.2.1 Photo Thermal Deflection Effect	59
2.2.2 Photoacoustic Spectroscopy	60
2.2.3 The Photopyroelectric Spectroscopy	63
2.3 Experimental Techniques Adopted in the Work	68
2.3.1 Photopyroelectric method	68
2.3.2 Thermal Analysis- TG/DTA and DSC	69
2.3.3 Fourier Transform Infrared Spectroscopy	71
2.3.4 X-Ray Powder Diffraction	71
2.4 The photopyroelectric spectrometer	72
2.4.1 Radiation Source	73
2.4.2 Modulation	73

2.4.3	PPE Detector	74
2.4.4	Signal Processing	75
2.4.5	The Complete PPE Spectrometer	75
2.5	Low Temperature PPE measurement setup	77
2.6	PPE Measurements with Magnetic Field	78
2.6.1	Magnetic field Measurement Setup	78
2.7	Measurement methodology	81
	Reference	82
Chapter 3: Thermal transport properties of Di Calcium Lead Propionate		
3.1	Introduction	86
3.2	Sample Preparation	88
3.3	Experimental Method	90
3.3.1	Photopyroelectric thermal wave measurements	90
3.3.2	Thermal analysis of DLP Crystals	97
3.3.3	FT-IR Spectrum	99
3.4	Results and Discussion	99
3.4.1	Thermal conductivity During Phase Transitions	99
3.4.2	Thermal conductivity Ellipsoids	101
3.4.3	Other Results	102
	References	105
Chapter 4: Thermal transport properties across the Incommensurate phase in Potassium Selenate		
4.1	Introduction	106
4.2	Sample Preparation	111
4.3	Experimental methods	113
4.3.1	Photo-pyroelectric thermal wave measurements	113
4.3.2	Differential Scanning Calorimetric Measurements	114
4.4	Results and Discussion	115
	References	126
Chapter 5: Thermal transport properties of $\text{La}_{(1-x)}\text{Te}_x\text{MnO}_3$ ($x= 0, 0.1, 0.15, 0.2$) exhibiting giant magneto resistance		
5.1	Introduction	129
5.1.1.	Giant magneto resistance	129
5.1.2	Manganese oxides	136
5.1.3	Electron doped manganese oxides	140
5.2.	Sample preparation	141
5.3	Experimental methods and Results	142
5.3.1	Photo-pyroelectric thermal wave measurements	142

5.3.2 DSC measurements	157
5.4 Discussion of results	160
5.4.1 X-Ray diffraction	160
5.4.2 PPE Measurements with Magnetic field	161
Reference	168

Chapter 6: Thermal transport properties of $ZnAl_2O_4$ - TiO_2 (ZAT)

Ceramics

6.1 Introduction	170
6.2 Sample Preparation	173
6.3 Experimental method	175
6.4 Results and Discussion	178
References	182

Chapter 7: Thermal transport properties of Polytetrafluoroethylene / $Sr_2Ce_2Ti_5O_{16}$ Polymer/Ceramic Composites

7.1 Introduction	184
7.2 Sample Preparation	186
7.3 Experimental method	187
7.4 Results and Discussion	192
References	196

Chapter 8: Summary and conclusions

197

PREFACE

In recent years there has been an increasing interest in optically excited thermal processes, known as photothermal effects, which use lasers as optical heat sources. The photothermal effect in a material is a consequence of the deposition of heat in the sample following absorption of a light beam and subsequent thermal deexcitations, or other nonthermal deexcitation processes, which result in the indirect heating of the sample. If the excitation is modulated, the corresponding temperature variations developed in the sample gives rise to a variety of different effects and most directly, to periodic temperature variations of the sample, which constitute the basis for a distinct experimental technique, known as photopyroelectric (PPE) effect.

The PPE technique involves measurement of the temperature variations in the sample due to absorption of radiation, by placing a pyroelectric detector in thermal contact with the sample. The PPE technique is the only technique based on the direct detection of photothermal heating, and therefore has a number of advantages over other detection schemes involving secondary mechanisms (like photoacoustic technique). A PPE experiment is rather simple to design and the materials that can be investigated range from weakly absorbing solids like thin films or liquids, to strongly absorbing solids and liquids or highly diffusing materials.

Even though much progress has been made on both theoretical and experimental fronts, enough efforts have not been made to exploit the advantages of the photopyroelectric technique in the measurement of thermal parameters, like thermal diffusivity (α), thermal effusivity (e), thermal conductivity (K) and heat capacity (c_p) of solid samples. The technique is particularly useful to study thermal properties of samples undergoing transitions such as ferroelectric phase transitions, metal-insulator transitions etc. In this thesis we present the results of our systematic investigation of the

variations in the thermal parameters across phase transitions in selected systems employing photopyroelectric technique.

Para-ferroelectric phase transitions are always associated with atomic rearrangements or structural changes. The change of structure during a phase transition can occur in two distinct ways. Firstly, there are transitions where the atoms of a solid reconstruct a new lattice as in the case of an amorphous solid changing to a crystalline state. Secondly, there are transitions where a regular lattice is distorted slightly without disrupting the linkage of the network. This can occur as a result of small displacements in the lattice position of single atoms or groups, or the ordering of molecules among various equivalent positions. Most of the ferroelectric phase transitions belong to the second group.

Since all the phase transitions involve configurational changes, one can identify a physical quantity that is characteristic of the new ordered configuration. Such a concept of order parameter was introduced by Landau. In a ferroelectric transition the order parameter is the spontaneous polarization and he expanded the Gibbs free energy in powers of the order parameter in the vicinity of a transition where the value of order parameter is very small. Accordingly, a transition is said to be of the same order as the derivative of the Gibb's function, which shows a discontinuous change at the transition. If there is a discontinuity in quantities such as volume and entropy, which are first order derivatives of Gibb's function, the transition is said to be of first order. If specific heat, compressibility, thermal expansion etc. are quantities undergoing discontinuity, which are second order derivatives of Gibb's free energy function, the transition is said to be second order. Our aim has been to study the variations of heat capacity and thermal conductivity of selected ferroelectrics and analyze the nature of phase transitions associated with it.

The phenomenon of magnetoresistance (*MR*) is defined as the change in electrical resistance (*R*) of a material in response to an externally applied magnetic field (*H*). Mathematically, it is written as $MR = [R(H) - R(0)]/R(0)$, where *R*(*H*) and *R*(0) are the resistances of the material in the presence of applied magnetic field and zero fields, respectively. In the year 1857, W. Thomson (Lord Kelvin) discovered a new phenomenon when he was measuring the resistance of iron and nickel in the presence of a magnetic field. This phenomenon is known as anisotropic magnetoresistance (*AMR*). It originates from anisotropic spin-orbit interaction and causes the resistance to depend on the relative orientation of electric current and magnetization. The 151-year-old *AMR* remained as the main source of magnetoresistance in ferromagnets till 1988, and there was hardly any improvement in the performance of magneto resistive material with time. The general consensus in 1980s was that it was not possible to significantly improve the performance of magnetic sensors based on magneto resistive effect. In 1988, there was an upsurge in the field of magnetoresistance as Fert's group discovered that the application of magnetic field to a Fe/Cr multilayer results in a huge reduction of electrical resistance, which was found to be much higher than *OMR* and *AMR* and named it as giant magnetoresistance (*GMR*). A similar effect in Fe/Cr/Fe trilayer structure was simultaneously discovered by Grünberg's group. Albert Fert and Peter Grünberg were awarded the Nobel Prize in 2007 for their independent discovery of *GMR*.

In this thesis, we have taken up work on photopyroelectric investigation of thermal parameters of ferroelectric crystals such as Di Calcium lead propionate (*DLP*), Potassium selenate, mixed valence perovskite samples such as Tellurium doped Lanthanum Manganate ($La_{1-x}Te_xMnO_3$) and ZnAl₂O₄-TiO₂ (*ZAT*) Ceramics and Polytetrafluoroethylene / Sr₂Ce₂Ti₅O₁₆ Polymer / Ceramic Composites which are used in electronic packaging.

The thesis is organized into eight chapters as outlined in the following paragraphs. To place the work in a better perspective, a detailed review of the different photo thermal techniques and their application in different area are discussed in detail in the first chapter.

In the second chapter we present an improved photopyroelectric technique, which we have developed, for the simultaneous determination of thermal parameters using a pyroelectric transducer kept in contact with a thermally thick backing medium. The principle of the technique, measurement technique is described in detail in this chapter. The new setup which is used for the study of variation of the thermal parameters of the materials showing properties like GMR is also described in this chapter.

Chapter 3 highlights the studies carried out on ferroelectric Di Calcium lead propionate (DLP) single crystals. The crystal has a tetragonal structure and is reported to have a para-ferroelectric phase transition at 333K K. There is a second phase transition at 191K which is associated with the methyl group. Details of crystal growth, identification of crystal morphology, sample preparation and measurement of all the four thermal parameters (thermal diffusivity, thermal effusivity, heat capacity and thermal conductivity) of DLP are outlined in this chapter. The measurements have been carried down to a temperature of 150 K. The variations of thermal conductivity along the three principal axes are interpreted in terms of phonon contribution. Detailed thermal analysis is done by TG/DTA and DSC techniques and FTIR spectrum is also taken to understand the chemical bonds and their motions in the crystal.

A detailed photopyroelectric investigation of the thermal conductivity anisotropy along the three principal directions in single crystals of potassium selenate and its variation with temperature are presented in Chapter 4 of the thesis. Potassium selenate is known to exist in four different phases between 745K and 77 K. At a higher temperature 745K (T_1) it

crystallizes in to a centrosymmetric orthorhombic structure. At $T_2 = 129$ K, there is a transition to an incommensurate phase and at $T_3 = 93$ K, it transforms to a commensurate form which is ferroelectric. Details of crystal growth, identification of the morphology of the grown crystal and preparation of the specimen for the measurements are described in detail. The variations of thermal parameters along the three principal directions are measured and the results are discussed in this chapter. The XRD and DSC measurements are also done and the specific heat of this sample at the higher transition temperature is calculated from the DSC measurements.

Chapter 5 is a treatise on the thermal characterization of mixed valence perovskite samples – $\text{La}_{(1-x)}\text{Te}_x\text{MnO}_3$ where $x = 0, 0.1, 0.15, 0.2$ – by varying magnetic field using PPE technique. The system is known to exhibit GMR properties and under goes transition at temperatures 140K, 240K and 255K respectively. The sample with $x=0.2$ doesn't show any phase transition. Electrical resistivity and thermoelectric power undergo anomalous variations in this temperature range. It is seen that the thermal conductivity undergoes anomalous variations in the same temperature range. Details of sample preparation, experimental method and results obtained are described in this chapter.

A systematic study of the thermal properties of three samples of $\text{ZnAl}_2\text{O}_4\text{-TiO}_2$ (ZAT) Ceramics using the photopyroelectric technique. This constitutes Chapter 6 of the thesis. Details of sample preparation and the results of the measurement are given. A discussion of the results is given towards the end of the chapter.

Chapter 7 reports our investigations on thermal properties of Poly-tetrafluoroethylene / $\text{Sr}_2\text{Ce}_2\text{Ti}_5\text{O}_{16}$ Polymer/Ceramic Composites which is reported to be a suitable material for electronic packaging, and investigations of its thermal parameters are interesting from this point of view. The results are explained in terms of existing models and presented in this chapter.

Chapter 8 is the concluding chapter of the thesis. This chapter discusses the general aspects of the results obtained on the above five samples. It also reviews the scope for future studies on thermal properties of samples, which undergo ferroelectric or M-I transition. Scope for doing further work using photopyroelectric effect is also outlined in this chapter.

The following papers have been published/ accepted for publication / presented in various journals / symposia.

1. A compact photopyroelectric set up for the determination of temperature variation of the thermal conductivity and heat capacity of solids
Journal of Instrument Society of India
2. A low loss, dielectric substrate in ZnAl₂O₄-TiO₂ system for microelectronic applications.
Journal of Applied Physics **98** (2005) 44101
3. Thermal Properties of Polytetrafluoroethylene / Sr₂Ce₂Ti₅O₁₆ Polymer / Ceramic Composites.
Journal of Applied Polymer Science, **108** (2008) 1716
4. Thermal transport across Incommensurate phase in Potassium Selenate: Photo-pyroelectric and calorimetric measurements
Journal of Physical society of Japan (Accepted)
5. Thermal properties of Dicalcium Lead Propionate across the prominent transition temperatures (communicated).
6. Thermal properties of Dicalcium lead propionate crystals using photothermal technique
Proceedings of the DAE Solid State Physics Symposium (2007)
7. Thermal transport properties of potassium selenate –a Photopyroelectric study
Proceedings of the Kerala Science Congress (2008)
8. Transient photoconduction in Te doped LaMnO₃ in the ceramic phase
Proceedings of International seminar on non-oxide glasses (2005)

Acknowledgements

This thesis arose in part out of years of research and by that time I have worked with a great number of people whose contributions in assorted ways to the research and the making of this thesis deserves a special mention. It is a pleasure to convey my gratitude to them all in my humble acknowledgment.

First and foremost, I wish to express my profound sense of gratitude to my research guide, Dr. Jacob Philip, Professor, Department of Instrumentation for his gentle and inspiring guidance. I am deeply indebted to him for his invaluable suggestions, forbearance, constant encouragement and support. Working with him has been a very informative and wonderful experience.

I would like to extend my deep sense of gratitude to the Head of the Dept. of Instrumentation, Dr. K. N. Madhusoodanan and former Head Dr. Stephen Rodriguez for allowing me to use the facilities of the department. Thanks are due to the present and past Heads of Department of Physics, for granting me the permission to use library facilities for my research work. I also extend my deep sense of gratitude to Dr. Prethapan Sreedharan of Department of Chemistry, for the timely help extended.

I am highly obliged by the help and cooperation of all the staff of our departmental office and workshop. Mr. Murali, Mr. Gopi Menon, Mr. Sukumaran, Mr. Jose, Mr. Jose Jacob, Mr. Casmir and Mr. Joshy are gratefully acknowledged for all their timely help. I extend my sincere thanks for the timely help from the office staff of the department. I also remember the staffs of STIC and SAIF for their kind co-operation during my research time.

With intense pleasure I acknowledge Dr. Johny Isaac, my M.Sc. project coordinator for the start of my research carrier. I express deep sense of gratitude to Dr. M. T. Sebastian, Scientist, R.R.L. for allowing me to do part of my work there. With a sense of gratitude, I remember all the faculty members, especially Dr. M. A. Ittiyachan, Dr. N.V. Unnikrishnan and Dr. L. Godfrey, of School of Pure and Applied Physics, M. G. university whose inspiration and guidance enabled me to embark upon research.

I express my heartfelt thanks to all my lab mates – Nisha R., Anu, Viji, Maju, Uma and Nisha M.R. for all the timely help extended when needed. I owe a special sense of gratitude to my seniors - Dr. R. Rajesh, Dr. Preethy Menon, Dr. A.V.Alex, Dr. Alex Mthew, Dr. Viamala George, Dr. Raghu O., and Dr. Nelson Rodrigues. I fondly recall all the little, nameless, unremembered acts of kindness and love of my dear friend – Rehana. I would like to thank Mr. V. M. Peter for his unreserved help at various stages.

I thank Cochin University of Science and Technology for the financial support offered during the course of research.

My family deserves the ultimate accolades for their selfless support, encouragement and patience. The largest debt of gratitude I owe is to my loving Achan, Amma, Chettan, Swapna and Gawrikutty. Much of what I am, cannot have been but for my understanding parents and my dear brother. My amma was the pillar of strength behind all my achievements in life. I deeply remember all members at tharavadu especially Ammomma, Chitta, Chittappan, Vava and Sowmya for their help and support all these years. Achan, Amma, Manu Chettan and Chettahiyamma are the special ones to whom I should thank for all their support given since I came there after my marriage. I extend my thanks to Dr. Satheesh and Renjini chechi for relieving down my tensions about Madhav's diseases.

I owe my husband Mahesh and our family a lot for their unstinting support and encouragement. As a true friend and partner, he has inspired and motivated me during my research life. He has provided me with the vital support without which this endeavor would not have had its successful culmination. I cannot forget my little ones. They are the one who releved my tensions and problems by their chirpiness at home. Thanks a lot to Maluooty and Madhavan. I also extend my deep love and thanks to my scooty –pep for the entire service it has given me. With out my vehicle this thesis would have remained a dream for me.

Finally I convey my sincere thanks to my entire well - wishers and friends who have directly or indirectly helped me.

And above all, into thy hands I lay all my works.

Manjusha M.V.

Chapter 1

Photothermal techniques to measure thermal properties of solids

1.1 INTRODUCTION

Photothermal spectroscopy is a group of high sensitivity methods used to measure optical absorption and thermal characteristics of a sample. The basis of photothermal spectroscopy is a photo-induced change in the thermal state of the sample. Light energy absorbed by the sample results in sample heating. This heating results in a temperature change as well as temperature – induced changes in thermodynamic parameters of the sample which are related to temperature. Measurements of the temperature, pressure, or density changes that occur due to optical absorption are ultimately the basis for the photothermal spectroscopic methods. Photothermal process is a more direct measure of optical absorption than optical transmission based spectroscopies. Sample heating is a direct consequence of optical absorption and so photothermal signals are directly dependent on light absorption. Scattering and reflection losses do not give rise to photothermal signals. Consequently photothermal spectroscopy more accurately measures optical absorption in scattering solutions, in solids, and at interfaces. This aspect makes it particularly attractive for application to surface and solid absorption studies, and studies in scattering media [1-8].

The basic processes responsible for photothermal signal generation are shown in Figure 1.1.

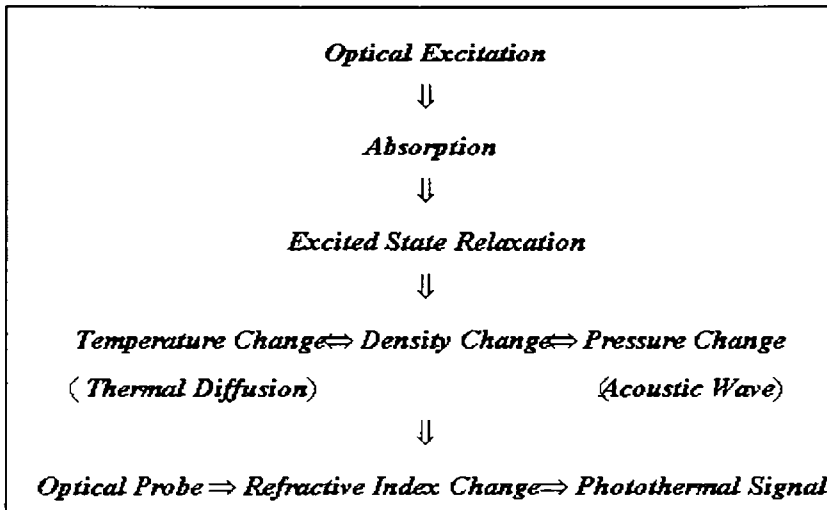


Fig.1.1: Processes involved in photothermal spectroscopy. Absorption of radiation from the excitation source followed by non-radiative excited state relaxation results changes in the sample temperature, pressure, and density.

Optical radiation, usually from a laser, is used to excite a sample. The sample absorbs some of this radiation resulting in an increase in the internal energy. The internal energy is dispersed in two different modes of hydrodynamic relaxation. The increased internal energy results in a temperature change in the sample or the coupling fluid placed next to the sample. This temperature change results in a change in sample or coupling fluid density. If the photothermal induced temperature change occurs faster than the time required for the fluid to expand or in a few cases contract, then the rapid temperature change will result in a pressure change. The pressure perturbation will disperse as an acoustic wave. Once the pressure has relaxed to the equilibrium pressure, a density change proportional to the temperature will remain. In either case there will be a change in temperature induced by the absorption of optical energy. This temperature change will in turn result in a density change in the sample. In combination, temperature and density

changes affect other properties of the sample. Photothermal spectroscopy is based on a measurement of these properties [9-15, 19, 20].

There are three main areas that must be considered while attempting to obtain a quantitative description of the photothermal spectroscopy signal. The first is a description of the optical absorption and excited state relaxation processes. Optical excitation followed by excited state relaxation results in sample heating. The rates and amounts of excited state excitation and relaxation will control the rate and magnitude of heat production. The energy transfer steps that need to be accounted for are shown in Fig. 1.2. Energy can be transferred to the sample by optical absorption and inelastic scattering process such as Raman Scattering is inefficient and the amount of energy lost to sample is usually small enough to be neglected. After absorption, the molecules are in an excited state. Excited state relaxation transfers energy to the solvent or sample matrix. Radiative relaxation does not result in complete loss of the absorbed energy to the sample. Some of the energy is lost in the form of the radiated light. Thermal relaxation transfers the energy to the sample matrix and results in sample heating. Excited species may also form long lived metastable states that trap energy and prevent further optical absorption. This will result in a delayed heating of the sample. The excited state species may also participate in photochemical reactions. Photochemical reaction can produce heat but also produce new chemical.

These relaxation processes may all produce excess energy in the form of heat. The heat increases the internal energy of the sample. The sample will respond to this increased energy [16, 17]. The second area is that of the hydrodynamic relaxation. After optical heating, the sample is not in thermal equilibrium with itself or with the surrounding environment during a measurement. Heat generated by the optical excitation and relaxation processes will result in thermal gradients between the excited sample and the surroundings. The thermal gradients result in heat transport. Heat is

transferred within the sample in such a fashion as to move toward thermal equilibrium. Hydrodynamic relaxation produces changes in the temperature, pressure, and density of the sample.

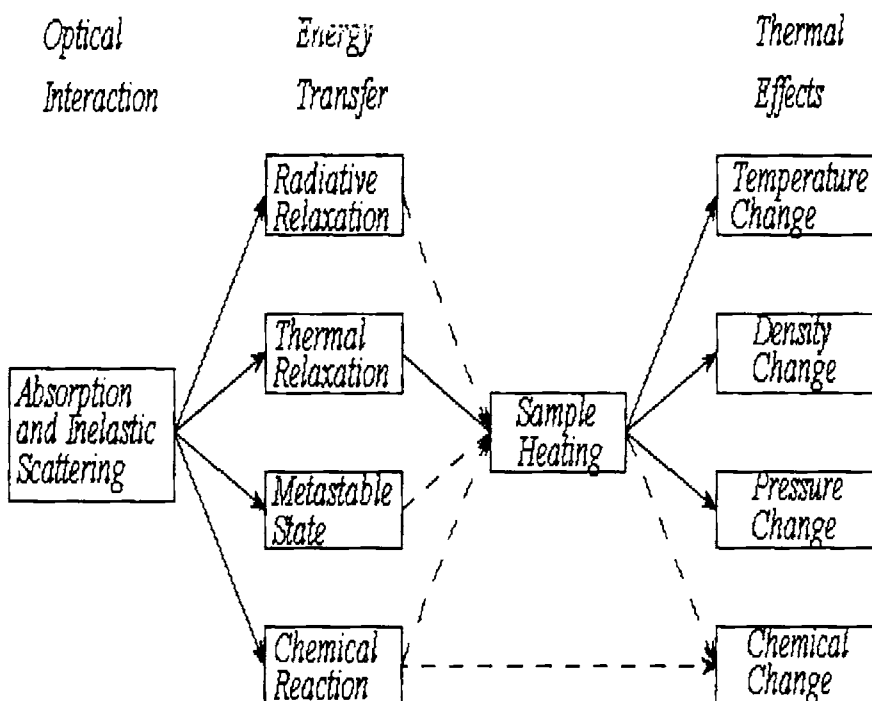


Fig.1.2: Several of the mechanisms for excited state relaxation are illustrated. The main steps are optical interaction, energy transfer, sample heating, and thermal effects. Radiative relaxation, metastable state production, and photochemical reaction may result in some sample heating. Energy transfer step may result in fast or slow kinetic energy production

The third area is that of the signal generation process. Photothermal spectroscopy signals are based on changes in sample temperature or related thermodynamic properties of the sample. These are usually monitored through the corresponding change in the refractive index of the sample or a

thermal coupling fluid placed in contact with the sample. Several properties may affect the refractive index of the medium [21-34]. The most common is the density. However, the refractive index may also change with temperature, population in optically excited states, and with chemical composition if photochemical reaction occurs. There are a variety of instrumental methods used to probe the changes in the sample's refractive index. Other instrumental methods used for photothermal spectroscopy directly probe the temperature or related thermodynamic properties, but the most sensitive methods probe the spatial or temporal gradients of these properties.

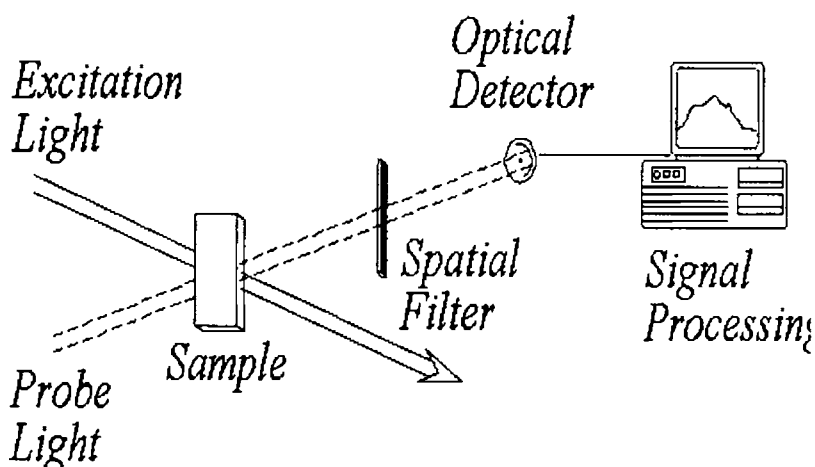


Fig.1.3: A generic photothermal spectrometer showing essential features.

A schematic diagram illustrating the main components used for photothermal measurements is shown in Figure 1.3. The experimental modules consist of the following six main components;

1. sample
2. light source used for sample excitation

3. light used to monitor refractive index perturbations
4. a mask, aperture, or other form of spatial filter for the probe light
5. an optical detector used to detect the optically filtered probe light
6. electronic signal processing equipment

The excitation light heats the sample. The probe light monitors changes in the refractive index of the sample resulting from heating. The spatial and propagation characteristics of the probe light will be altered by the refractive index. The spatial filter selects those components of the altered probe light that change with the sample's refractive index. The optical detector monitors changes in the probe light power past the spatial filter. In some experimental arrangements, a spatial filter and a single channel detector are combined using an image detector. Signals generated by the photo detector are processed to enhance the signal to noise ratio [35-45].

In addition, an apparatus may also be equipped with detectors to monitor the excitation and probe light power, a thermostatic sample holder, and optical spatial filters to control the spatial profiles of the excitation and probe light. This additional equipment is used to control the experimental environment and to measure the optical power required to accurately quantify changes that occur in the sample. These components are necessary when the data must be used to determine absolute absorption of the sample.

In theory, the photothermal spectroscopy signal can be accurately calculated based on knowledge of the experimental set up, the parameters that characterize light propagation, and the optical parameters of the sample. The following steps must be followed for in the calculations;

1. determine the optical absorption resulting in sample heating
2. determine the rate of heat production
3. determine the temporal and spatial temperature and density change

4. relate the refractive index change to the temperature or density change using the thermal-optical parameters of the sample
5. calculate the strength of the optical element formed from the spatial-dependent refractive index change
6. calculate the optical and electronic output signals resulting from passage of light through apertures or using specialized detectors.

1.2 PHOTOTHERMAL SPECTROSCOPY METHODS

There are a variety of methods used to monitor the thermal state of the analytical sample (29, 151, 17). Direct calorimetric or thermometric methods use temperature transducers to measure analytical sample temperature. Pressure transducers are used to monitor the pressure wave associated with rapid sample heating. Photothermal interferometry, photothermal deflection spectroscopy, photothermal lensing spectroscopy (also known as thermal lens spectroscopy), photothermal diffraction spectroscopy, and methods based on sample reflection changes are all based on monitoring refractive index changes associated with sample heating. Infrared detectors can be used to monitor changes in the sample's infrared emission associated with heating. Each of these methods is based on a measurement of temperature change associated with increase in the internal energy of the analytical sample [41, 43, 46-60].

Photo thermal methods have been reported by individuals working in several areas of science and technology. Subsequently, there are several names that the particular methods are known by. The temperature changes resulting from the photothermal effect can be detected using a variety of methods. These methods are summarized in Table 1.1.

Table 1.1 Common detection techniques used in photothermal spectroscopy

Thermodynamic Parameter	Measured Property	Detection Technique
<i>Temperature</i>	<i>Temperature</i>	<i>Calorimetry</i>
	<i>Infrared Emission</i>	<i>Photothermal Radiometry</i>
<i>Pressure</i>	<i>Acoustic Wave</i>	<i>Photoacoustic Spectroscopy</i>
<i>Density</i>	<i>Refractive Index</i>	<i>Photothermal Lens</i> <i>Photothermal Interferometry</i> <i>Photothermal Deflection</i> <i>Photothermal Refraction</i> <i>Photothermal Diffraction</i>
	<i>Surface Deformation</i>	<i>Surface Deflection</i>

Temperature can be directly measured using thermocouples, thermistors, or pyroelectric devices in the method of photothermal calorimetry. Temperature changes can also be indirectly measured using methods which monitor infrared emission since the thermal infrared emission is related to sample temperature. The method of thermal emission or photothermal radiometry of infrared radiation can be used to monitor relatively large temperature changes that occur as a consequence of optical absorption. Although not very sensitive, this method has great potential for application in nondestructive materials analysis and testing. Using infrared sensitive cameras, it can be used for imaging the thermal properties of large samples.

Two other temperature dependent thermodynamic parameters that are commonly exploited in photothermal spectroscopy are pressure and density. The pressure changes that occur upon periodic or pulsed sample

heating can be detected using a microphone or other pressure transducer to monitor the acoustic wave. The method of optoacoustic or photoacoustic spectroscopy is based on the measurement of this pressure wave.

Under steady-state, an isobaric condition, the density is related to the temperature through the volume expansion coefficient. Temperature dependent density changes are difficult to measure directly. But density changes can affect the sample in several different ways. In solid samples, the density change alters physical dimensions at sample surfaces. Sample dimension changes give rise to two optical methods for monitoring the temperature change based on surface deformation. A homogeneous deformation (expansion or contraction) displaces the surface of the sample. Interferometry can be used on reflective samples. Since small displacements, on the order of a few parts-per-million of the wavelength of probe beam light, can be measured using interferometry, this method may be used for sensitive measurement of solid sample absorption. Spatially heterogeneous expansion (or contraction) can also cause the surface angle to change. A probe beam reflected from the surface will change angle when heterogeneous expansion occurs. Measurement of the probe beam angle gives rise to the method of photothermal surface deflection spectroscopy [61-73].

The optical path length changes that occur due to the photothermal induced refractive index change can be measured with interferometry. Using interferometry, the phase of the monochromatic light passing through the heated sample, relative to the phase passing through the reference arm, results in a change in power at a photoelectric detector. There are several different interferometry schemes that can be used to detect changes in the optical path length induced by the photothermal effect. These methods may all be classified as being under photothermal interferometry.

Spatial gradients in refractive index result in a direction change in the propagation of a beam of light. Thus light will exit a medium at an angle relative to the incident beam when there is a refractive index gradient in the sample. This bending of light path is commonly called photothermal deflection and is the basis of Photothermal Deflection Spectroscopy (PDS).

Spatial dependent refractive index profiles can also result in focusing or defocusing of light. This occurs when the refractive index profiles are curved. Thus the thermally perturbed sample can act as a lens. Light transmitted through an aperture placed beyond the photothermal lens will vary with the strength of the lens. Photothermal methods based on measurement of the strength of this lens are called photothermal lensing spectroscopy. Some experimental methods measure a signal that is due to the combined effects of deflection and lensing. These may be generally classified as photothermal refraction spectroscopy methods.

Lastly, a periodic spatial refractive index modulation results in a volume phase diffraction grating. The grating will diffract light at an angle that meets requirements from Bragg's Law. The amount of light diffracted is proportional to the refractive index change. The diffracted light is measured with a photoelectric detector. Methods used to measure spectroscopic signals based on volume phase diffraction gratings formed by the photothermal effects are called photothermal diffraction spectroscopy [74-88].

Tanaka [106] has described the advantages of the photothermal diffraction technique in great detail. These advantages can be summarized as follows:

1. High accuracy not required for measuring small absorptions
2. Signal-to-noise ratio (SNR) increased by increasing the light intensity incident on the sample because the absorbed radiation energy is proportional to the light intensity

3. Thermal-wave techniques mostly insensitive to light scattering
4. Useful in a wide-photon-energy range, thanks to their sensitive detection system
5. Simple and direct detection measurements
6. No need for critical alignment of optical components

1.2.1 Photoacoustic Spectroscopy

The photoacoustic spectroscopy has evolved over the past two-three decades as a powerful method to study those materials that are unsuitable for study by conventional spectroscopic techniques [90-92]. This technique is based on the photoacoustic effect, originally detected by Alexander Graham Bell in 1880 [4, 5]. It possesses some unique features, mainly due to the fact that, even though the incident energy is in the form of photons, the interaction of these photons with the sample is studied not through the subsequent detection and analysis of photons, but through a direct measurement of the energy absorbed by the material as a result of its interaction with the incident photon beam.

The photoacoustic (PA) effect is the generation of an acoustic signal when the sample under investigation, placed inside an enclosed chamber, is irradiated by an intensity modulated beam of light. In case of gaseous or liquid samples, the sample fills the entire volume of the cell and acoustic signals are detected by a microphone or a piezo electric transducer. In the case of solids, the samples fill only a portion of the cell and the remaining volume of the cell is filled with a non-absorbing gas like air. The PA signal is detected using a sensitive microphone suitably placed inside the cell. The absorption of the incident radiation will excite the internal energy levels of the sample and upon subsequent deexcitation, all or part of the absorbed photon energy is converted into heat through non-radiative deexcitation

processes. In the case of gas and liquid samples, which fill the entire volume of the sample chamber, this internal heating causes pressure fluctuations having the same frequency as that of the modulation frequency of the incident radiation and can be detected using an acoustic transducer kept in intimate contact with the sample. In the case of solid samples which fill only a portion of the sample chamber, the periodic heating of the sample results in a periodic heat flow from the interior of the sample to the surrounding non-absorbing gas medium which in turn produces pressure fluctuations in the gas and detected as an acoustic signal by a microphone, suitably placed in the chamber. It is also possible to measure the heat generated in a bulk solid sample through the subsequent pressure or stress variations in the sample itself by means of a piezoelectric detector in intimate contact with the sample. Even though the sensitivity in this case is better, it is not always possible to employ a piezoelectric detector due to the limitations imposed by the nature of the sample. Also, the use of piezoelectric transducers is very difficult for PA measurements that involve variations of the sample temperature over a wide range.

A schematic diagram of photoacoustic detection process is shown in Fig.1.4 During a photo acoustic measurement the sample is enclosed in a small, tightly closed sample compartment called photoacoustic cell (usually cylindrical in shape).The photoacoustic effect is based on the sensitive detection of acoustic waves launched by the absorption of pulsed or modulated laser radiation via transient localized heating and expansion in a gas, liquid, or solid. When the laser hits the sample, some of the energy is absorbed by the molecules in the samples resulting in a region of higher temperature. The rise in temperature will generate an expanding region and a

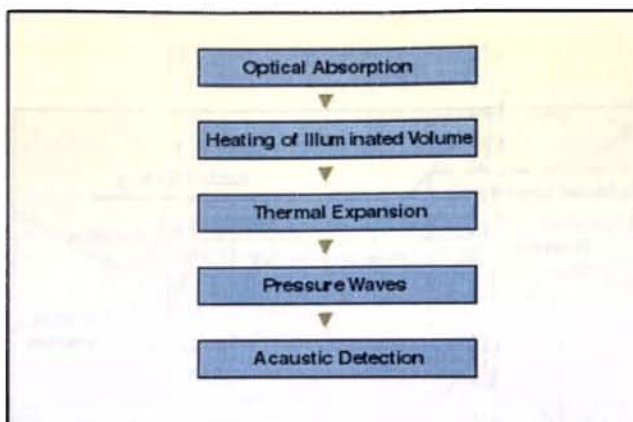


Fig.1.4: Diagram showing the generation of acoustic waves and their detection

pressure wave will propagate away from the heat source. The periodic pressure wave can be detected using a pressure transducer in contact with sample (piezo electric) or in contact with contact gas (microphone) in the photoacoustic cell. Fig.1.5 shows the details of the cell and signal generation process. The pressure transducer signal is proportional to the amplitude of the pressure wave.

Spectroscopy is however; only one of the several applications of PA effect. In the spectroscopic regime itself, photo acoustics can be used to measure the absorption and excitation spectra, the life time of excited states and the quantum yield of radiative processes. In addition to this, the calorimetric or thermal aspects associated with the PA effect offers a wide range of applications to study the thermal and elastic properties of materials. In such studies, the calorimetric or acoustic aspect of photoacoustics plays the dominant role, while the optical part is simply a convenient mechanism for heat generation. Such applications include measurement of thermal parameters, thermal wave imaging and study of phase transitions in solids

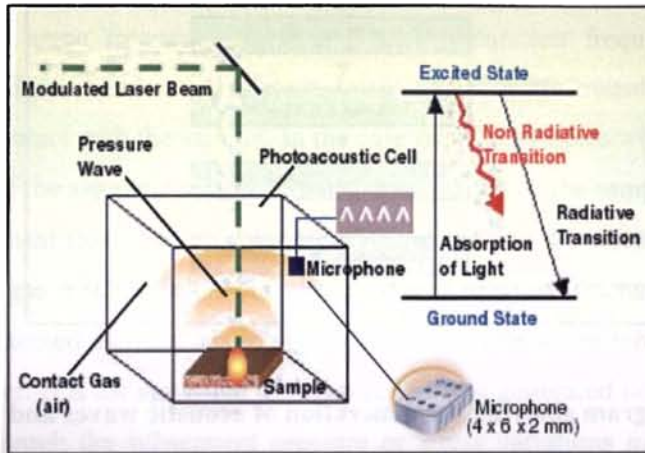


Fig.1.5: Photoacoustic effect from a sample

1.2.2 Photothermal Deflection

Photothermal Deflection Spectroscopy (PDS) was introduced by Boccarda, Fournier, and their collaborators in 1979 [11]. The basic phenomena of PDS are the deflection of a light beam when it travels through a refractive index gradient created due to a temperature gradient in a medium. In PDS, two laser beams are used. One is the probe laser beam which passes through the sample being studied and the other is a modulated pump laser beam, whose wavelength is absorbed by the sample. Fig. 1.6 shows the schematic representation of principle of photothermal deflection spectroscopy.

The modulated pump beam creates a thermal diffusion wave inside the sample. This is due to the conversion of optical energy absorbed from the modulated pump beam into thermal energy. The optically generated thermal oscillation penetrates the surrounding gaseous or fluid medium within a thermal diffusion length and causes a modulated change in its refractive

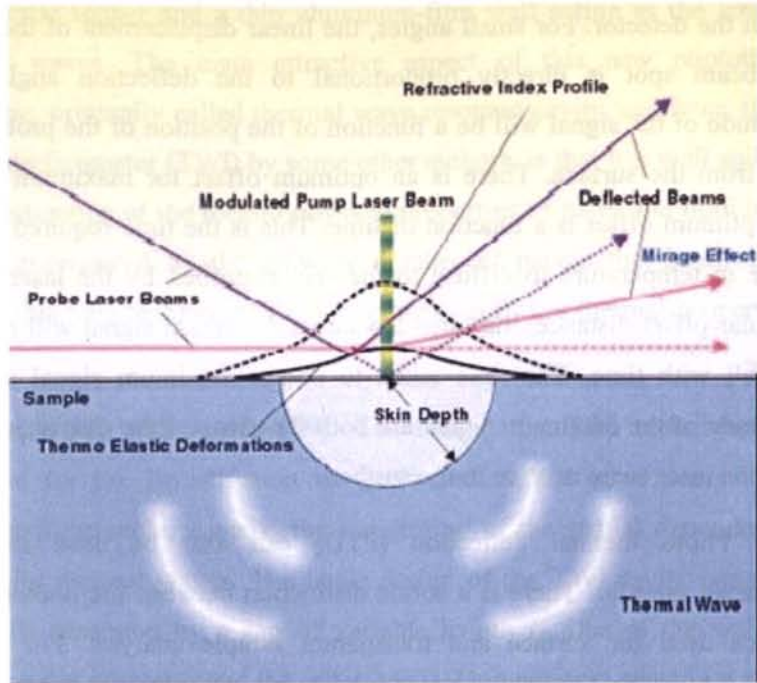


Fig.1.6: Principle of photothermal deflection spectroscopy

index right above the optically pumped region. A probe laser beam traveling parallel to the surface will be deflected harmonically and the phenomenon is known as the mirage effect or photothermal deflection.

The amplitude and phase of the deflected probe beam carry information about the optical and thermo physical properties of the absorbing solid or liquid. Another source of deflection is the thermo elastic deformation bump generated by intermittent laser heating and thermal expansion. A probe laser beam directed at an angle to the surface will be deflected by the bump. The modulated pump beam creates a thermal diffusion wave inside the sample.

The deflection angle of the probe beam is usually measured using a position sensing detector which is placed at a distance from the sample. A change in angle at the sample results in a displacement of the probe laser

spot on the detector. For small angles, the linear displacement of the probe laser beam spot is directly proportional to the deflection angle. The magnitude of the signal will be a function of the position of the probe laser beam from the surface. There is an optimum offset for maximum signal. This optimum offset is a function of time. This is the time required for the change in temperature to diffuse to the region probed by the laser. For a particular offset distance, the time-dependent deflection signal will rise and then fall with time. The time taken to obtain maximum signal and the magnitude of the maximum signal are both functions of the displacement of the probe laser beam relative to the surface

Photo thermal deflection (PTD) can also be used to study transparent samples. There is a subtle distinction between the photothermal methods used for surface and transparent sample analysis. For surface analysis, the probe laser is used to detect a refractive index gradient formed in the media above the surface. In transparent samples, the refractive index is changed within the sample itself. To study these samples, the excitation and probe lasers propagate collinear through the sample. So the deflection angle signal is essentially the same as the pulsed laser photothermal lens inverse focal length. This method is very similar to photothermal lens spectroscopy. Photothermal lens and photothermal deflection methods both rely on the generation of a refractive index gradient in the sample itself. Collectively, they have become known as refractive index gradient detection or photothermal refraction spectroscopy methods.

1.2.3 Photothermal Interferometry

The concept of thermal wave interference introduced by Bennett and Patty [92] in the early 1980s has gained considerable interest in recent years after Shen and Mandelis [93] demonstrated the feasibility of pyroelectric detection of a thermal wave propagating across the air gap formed between a

pyroelectric sensor and a thin aluminum-film wall acting as the source of thermal waves. The main attractive aspect of this new photothermal technique, originally called thermal wave resonant cavity, and later, thermal wave interferometer (TWI) by some other authors, is that it is well suited for the investigation of the thermo physical properties of gases and liquids. This can be appreciated by the growing number of papers that have recently applied this new technique to the investigation of the thermal properties of gases

[94-98] and liquids [99]. The reason the TWI technique is so attractive for the investigation of gases and liquids is evident from its operational principle, namely, the monitoring of the spatial dependence of intracavity thermal waves. The basic design of the TWI cavity consists of two walls separated by a gap of variable length L . One of the walls is a thermal wave generator and the other one is a temperature-sensing wall. The thermal wave generator consists of a thin aluminum foil on which a modulated light beam impinges on its black-painted outer surface, acting, accordingly, as a light absorber. Following the absorption of the modulated light beam, the Al foil temperature varies periodically at the modulation frequency of the incident beam, thereby launching thermal waves into the gap between the two walls. The thermal waves thus generated propagate back and forth between the Al foil and the sensing wall, which consists of a thin-film pyroelectric sensor. The TWI method consists essentially of recording the temperature fluctuation of the pyroelectric sensor as a function of the cavity gap length. The gas or the liquid sample is contained in the cavity. That is, the technique is essentially based on measuring the temperature fluctuation on a sample of variable thickness. This fact renders this technique well suited for gas and liquid samples analysis [100].

A one dimensional geometry of the system is shown in Fig.1.7

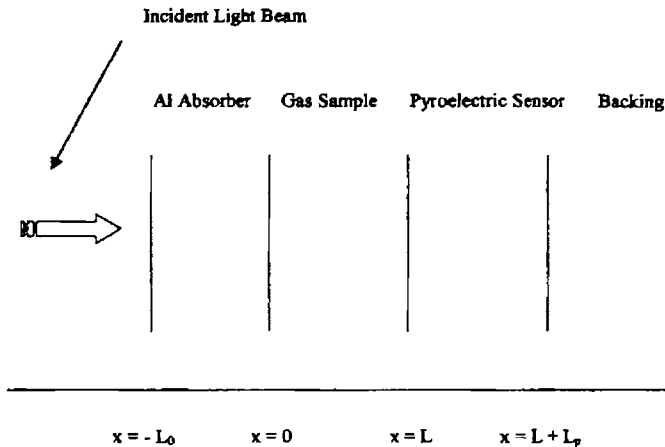


Fig. 1.7: Geometry of the TWI signal generation in which the incident light

1.2.4 Photopyroelectric Effect

The pyroelectric (PE) effect consists in the induction of spontaneous, rapid polarization in a noncentrosymmetric piezo electric crystal as a result of a temperature change in the crystal. The pyroelectric property offers the possibility to use PE materials for a number of applications. PE sensors present five main advantages that make them suitable for many applications.

1. Sensitive in a very large spectral bandwidth
2. Sensitive in very wide range of temperature with out any need for cooling
3. Low power requirements
4. Fast response
5. Generally low cost materials.

At first this effect was mainly employed in the detection of radiation, especially infrared, and in laser power measurements as well as in solar energy technology. During the last few years, the pyroelectric sensors have also found applications in thermal wave tomography for subsurface defect

detection. Recently the pyroelectric phenomenon has also been used for the manufacturing of gas sensors.

Pyroelectricity is the manifestation of the spontaneous polarization dependence on temperature of certain anisotropic solids. This effect is exhibited only by solids that satisfy crystallographic requirements such as no center of symmetry for the crystal lattice and no more than one axis of rotational symmetry for the crystal. A pyroelectric material becomes electrically neutral when in a constant temperature environment for a period of time. If there is a small change of temperature, the pyroelectric material becomes electrically polarized and voltage arises between certain directions in the material. Pyroelectric materials exhibit the property that the polarization vector is function of temperature. As the temperature varies, the surface charge also varies because of dimensional changes in the pyroelectric. This property results in a potential difference between the two opposite surfaces of the material, generally known as pyroelectricity.

Photopyroelectric (PPE) spectroscopy is one of the important photothermal techniques. With PPE spectroscopy the transmitted light generates a strong pyroelectric signal that, in some limits, is easy to distinguish from the signal because of the absorption of light in the sample itself. Or else we can say that PPE spectroscopy is technically less complex and less expensive than PAS: instead of a microphone, a pyroelectric thin film is used for the detection of the thermal wave. Among the advantages of the pyroelectric technique, the important are listed below

1. Possibility of operation over a wide temperature range (10 to 440K)
2. Short response time
3. Less complex configuration for ultrahigh vacuum studies
4. Faithful response in gaseous as well as in liquid media.

PPES has the useful capability of performing Nondestructive evaluation (NDE) and depth-profile analysis of a light absorbing material.

Depending upon the signal generation and detection mode we can have three main types of photopyroelectric analysis.

- Frequency-domain (F-D) scheme : harmonic modulation of the incident light at a single frequency and simple pyroelectric calorimetric detection [126]
- Frequency multiplexed excitation: correlation and spectral analysis of input and output signal channels. [134]
- Time domain measurements: pulsed optical excitation of the sample and PE detection. [135-139]

Figure 1.8 shows generic pyroelectric photothermal instrumentation, including pulsed optical excitation and detection.

Frequency – domain PPE instrumentation is the simplest of the three modes. In fact, the experimental setup of this technique does not present any particular problems. The cost of the instruments is relatively low and the basic parts of the pyroelectric photothermal instrumentation are relatively abundant in quantity in scientific laboratories. Photopyroelectric PVDF thin film detectors yielding high-quality signals are commercially available at a very low cost.

Frequency-domain photopyroelectric measurements can be divided into two main groups: the back detection technique (BDT) and the front detection technique (FDT). This thesis deals with the back detection method, for completeness we first describe the front detection technique.

Marinelli *et al.*, [141] were the first to use the PPE technique in the front detection mode. The configuration of the technique is given in Fig. 1.9. As it is seen in Fig. 1.9, one side of the detector is in contact with the

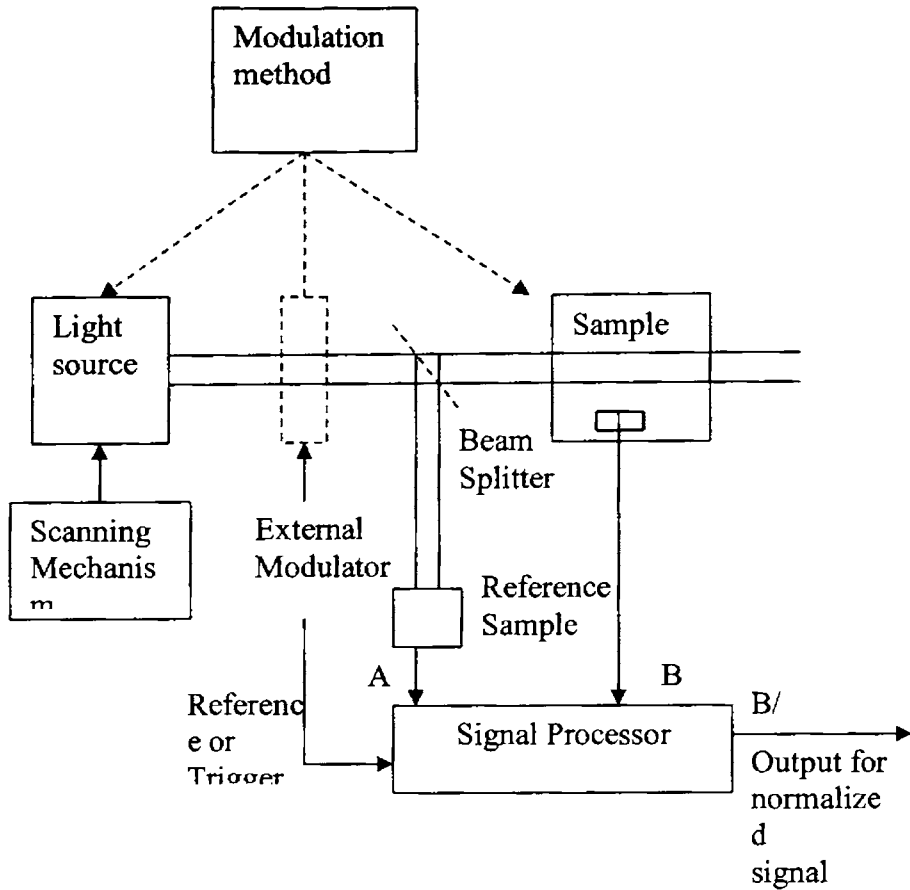


Fig.1.8: Generic pyroelectric photothermal instrumentation, including pulsed optical excitation and detection

sample, while the opposite side is illuminated. In this case, light strikes directly on the detector and not on the sample. In back detection technique, one side of the sample is in contact with the detector, while the opposite side is illuminated. The configuration for the technique is shown in Fig. 1.10. The advantage of the FDT is that it can be used in a wide frequency range and it can attain a large signal at a high frequency limit, which allows a high depth resolution in the sample.

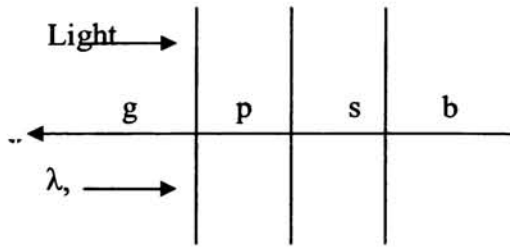


Fig. 1.9 (A): One-dimensional geometry for the photopyroelectric technique in the front detection configuration

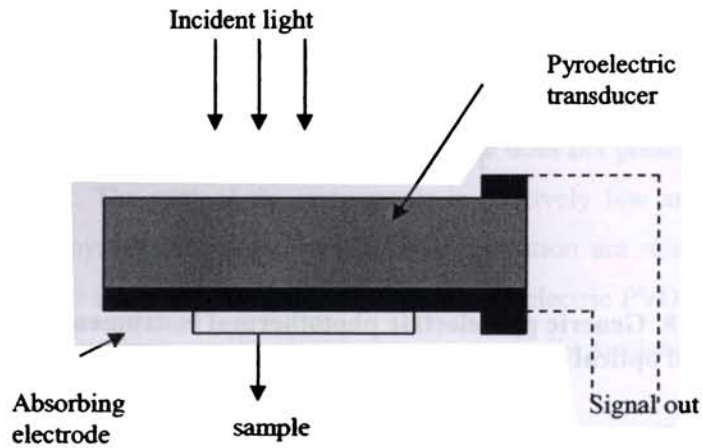


Fig. 1.9(B): Experimental configuration of the sample and detector for photopyroelectric front detection

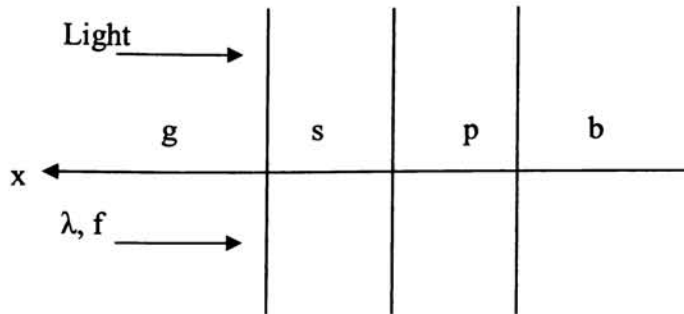


Fig. 1.10 (A): One-dimensional geometry for the photopyroelectric technique in the back detection configuration

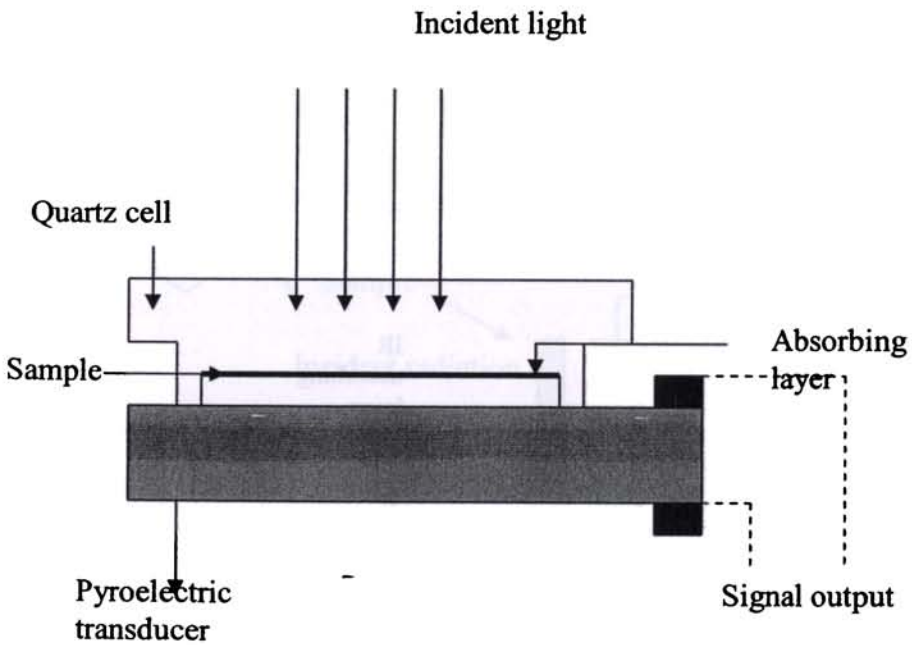


Fig. 1.10 (B): Experimental configuration of the sample and pyroelectric transducer for photopyroelectric back detection

Figures 1.11a and b show methods of construction of a pyroelectric detector by using PVDF thin film. In those figures one can see the IR absorbing layers, the metallic electrodes as well as the PVDF films. In Fig.1.11a the incident radiation is constant and therefore the output voltage, V_0 , is d.c. On the other hand, in figure 1.11b the beam was modulated by a mechanical chopper, and as a result the output voltage, $V(f)$, has an alternative from depending on the modulation frequency f .

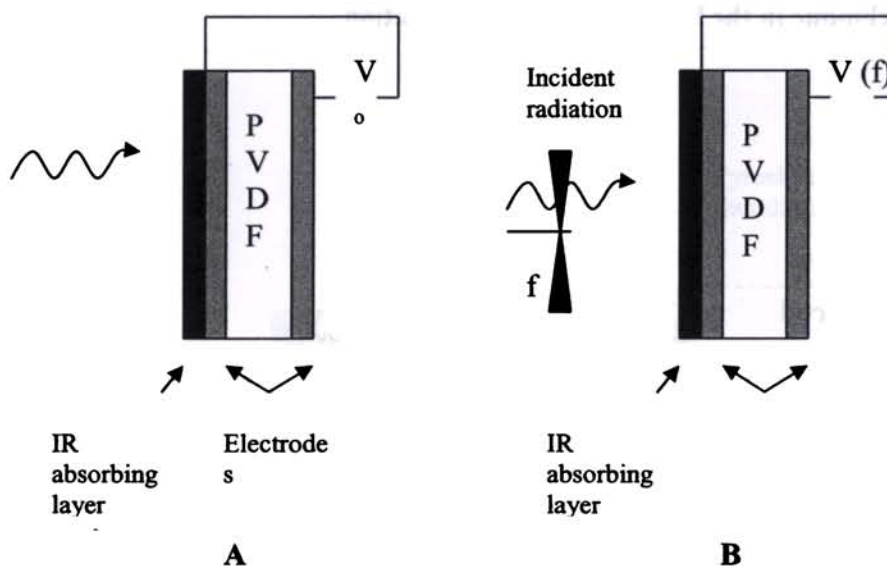


Fig .1.11: The basic idea of the photopyroelectric spectroscopy. (a) d.c. PPE induced voltage. (b) Photothermal modulation and a.c. induced voltage

Figures 1.12a we present the PPE detection in transmission mode. In this case the output voltage depends on the light's wavelength, the frequency, and the optical properties of the sample such as the reflectance, R , and the

absorption coefficient, β . Finally figure 1.12b shows the detection in thermal mode. In this case the sample is directly in contact with the pyroelectric detection. The output voltage in addition to the previous factors, f , λ , R , and β , depends on the thermal properties of the sample such as the thermal diffusivity, α and the nonradiative quantum efficiency η .

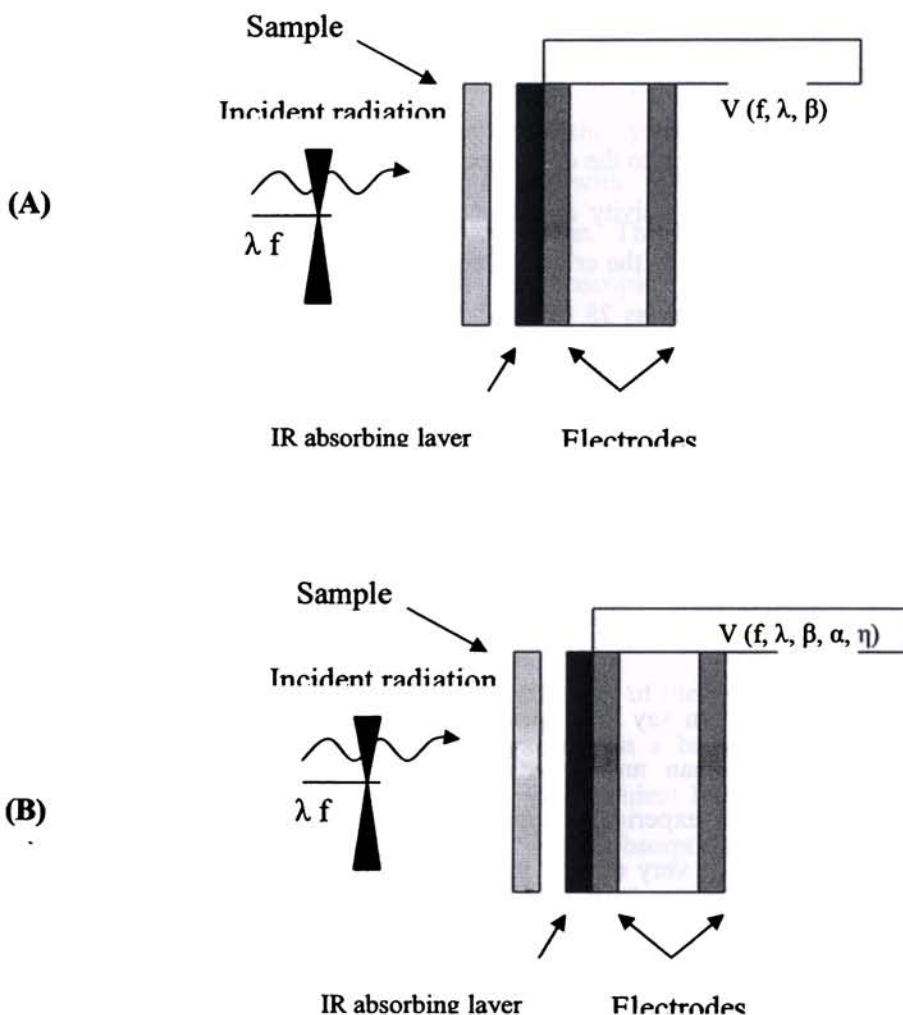


Fig.1.12 (a) PPE detection in transmission mode.
(b) PPE detection in thermal mode

Christofides *et al.* [142] used two different thickness of polyvinylidene difluoride (PVDF) film with two different thickness, 28 μm and 52 μm as pyroelectric detector in order to obtain thermally thick pyroelectric conditions. The thickness of the detector and the modulation frequency must be such that the condition

$$f \gg f_c \equiv \frac{\alpha_p}{\pi L_p^2} \quad (1.1)$$

is satisfied according to the definition of the thermally thick limit. α_p and L_p are the thermal diffusivity and the thickness of the detector respectively [126]. In Eq. (1.1), f_c , the critical frequency equals 22 Hz and 5 Hz for the PVDF film of thickness 28 μm and 52 μm respectively. The thermal time response of the PVDF film depends upon its thickness, since a longer time is needed for a thicker detector to reach thermal equilibrium within the pyroelectric after excitation [128]; yet for a range of low frequencies (0.5 to 600 Hz) this dependence is significant. The frequency response characterization experiment is necessary to work in a frequency range greater than 25 Hz or so in order to satisfy the conditions of the theoretical models.

So we can say PPE spectroscopy is technically less complex and less expensive than any other photo thermal methods. The necessary condition for the experiment depends only on the thermal thickness of the detector, which is very easy to satisfy. However, one disadvantage of PPE spectroscopy is its susceptibility to acoustic noise [91]. This problem can be partially alleviated by isolating the mechanical chopping system from the optical table that supports the rest of the instrumentation.

1.2.5 Theory of Photopyroelectric Effect in Solids

The first successful attempt to derive a general expression for the photopyroelectric signal voltage developed in the pyroelectric detector, in intimate contact with a sample was made by Andreas Mandelis and Martin Zver in 1985 [126]. They put forward a one-dimensional photopyroelectric model of a solid sample in contact with a pyroelectric thin film detector, supported on a backing material. The emphasis is placed on the conditions and / or restrictions imposed on the values of the system parameters so that the technique can produce signals linear with the optical absorption coefficient of the material under investigation. The limits of validity of photopyroelectric spectroscopy as a spectroscopic technique are also identified herewith.

A one-dimensional geometry of a photopyroelectric system, as suggested by Mandelis and Zver, is shown in Fig. 1.13(a). They considered a solid sample of thickness L_s , irradiated by a monochromatic light beam of wavelength λ , whose intensity is modulated at an angular frequency ω_o by a chopper. The sample has optical absorption coefficient $\beta_s(\lambda)$ and is in intimate contact with a pyroelectric detector of thickness L_p . The optical absorption coefficient and pyroelectric coefficient of the detector are $\beta_p(\lambda)$ and p respectively. The detector is supported on a backing material of thickness L_b , large compared to L_s or L_p . The incident light is assumed to illuminate the sample surface uniformly. Light absorption by the sample surface and non-radiative energy conversion to heat causes the temperature increase of the pyroelectric thin film. This temperature increase results in a potential difference between the upper and lower surfaces of the pyroelectric detector. This voltage $V[\omega_o, \beta_s(\lambda)]$ causes an electrical signal, which is measured in the external circuit, through the connections to the pyroelectric detector as in Fig. 1.13(b).

The charge accumulated in the pyroelectric, due to a change ΔT in temperature is given by

$$Q = p \Delta T \quad (1.2)$$

For a pyroelectric film of thickness L_p , the average charge induced due to the pyroelectric effect is

$$\begin{aligned} \langle Q \rangle &= p \Delta T = \left(\frac{p}{L_p} \right) \int_{\text{Thickness } L_p} T(x) e^{i\omega_o t} dx \\ &= \left(\frac{p}{L_p} \right) \text{Re} \left[\left[\int_{L_p} T(x) dx \right] e^{i\omega_o t} \right] \end{aligned} \quad (1.3)$$

The average pyroelectric voltage is then given by

$$V = \frac{\langle Q \rangle}{C} \quad (1.4)$$

where C is the capacitance per unit area of the thin film.

For two parallel charged plates of thickness L_p and dielectric constant K , Eq. (1.4) becomes

$$V(\omega_o) = \left[\frac{p L_p \theta_p(\omega_o)}{K \epsilon_o} \right] \exp(i\omega_o t) \quad (1.5)$$

$$\text{where } \theta_p(\omega_o) = \frac{1}{L_p} \int T_p(\omega_o, x) dx \quad (1.6)$$

Here, ϵ_o is the permittivity constant of vacuum (8.854×10^{-12} C/Vm), $T_p(\omega_o, x)$ is the temperature field in the pyroelectric detector as a result of heat conduction processes through the solid. For the geometry shown in Fig. 1.15 (b), $T_p(\omega_o, x)$ can be found from the solution of one-dimensional

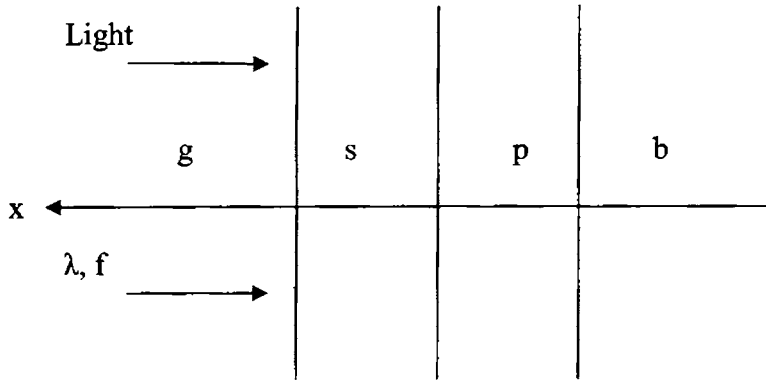


Fig. 1.13 (a): One-dimensional geometry of the photopyroelectric set up. g , s , p and b stand for the gas medium in front of the sample, sample, pyroelectric detector and backing respectively

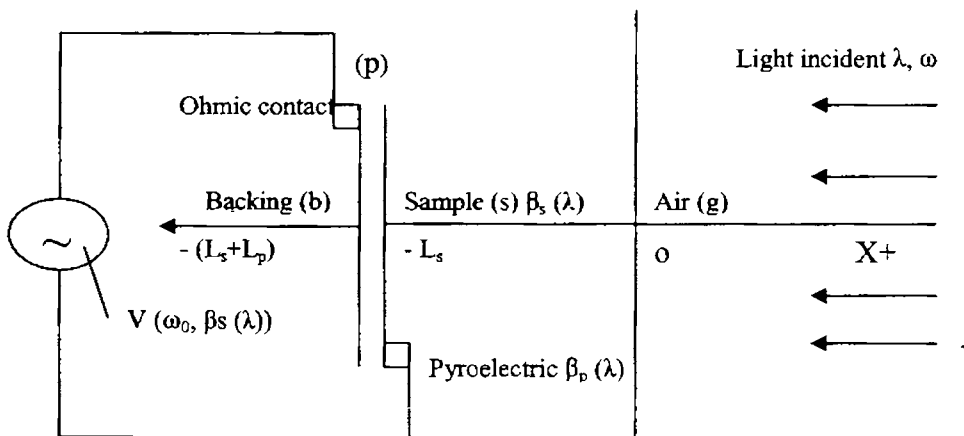


Fig. 1.13 (b): Electrical equivalent circuit of the photopyroelectric set up

thermal transport equations. Assuming that there is negligible optical reflection and radiative heat transfer coefficients on the sample surface and pyroelectric-sample interface, the appropriate heat diffusion equations have the form

$$\left(\frac{\partial^2 T_g(\omega_0, x)}{\partial x^2} \right) - \left(\frac{i\omega_0}{\alpha_g} \right) T_g(\omega_0, x) = 0; \quad x \geq 0$$

(1.7a)

$$\left(\frac{\partial^2 T_s(\omega_0, x)}{\partial x^2} \right) - \left(\frac{i\omega_0}{\alpha_s} \right) T_s(\omega_0, x) = - \left(\frac{I_0 \beta_s \eta_s}{2k_s} \right) \exp(\beta_s x);$$

$$-L_s \leq x \leq 0$$

(1.7b)

$$\left(\frac{\partial^2 T_p(\omega_0, x)}{\partial x^2} \right) - \left(\frac{i\omega_0}{\alpha_p} \right) T_p(\omega_0, x) = - \left(\frac{I_0 \beta_s \eta_p \exp(-\beta_s L_s)}{2k_s} \right) \exp(\beta_p (x + L_s))$$

$$-(L_p + L_s) \leq x \leq -L_s \quad (1.7c)$$

$$\left(\frac{\partial^2 T_b(\omega_0, x)}{\partial x^2} \right) - \left(\frac{i\omega_0}{\alpha_b} \right) T_b(\omega_0, x) = 0; \quad x \leq -(L_p + L_s) \quad (1.7d)$$

The subscript j refer to the respective media $j = s, p, b$ or g as in Fig. 1.15

(a). The various terms in the above equations are defined as follows

I_0 = Intensity of light source

k_j = Thermal conductivity of the respective media j ($= s, p$
 g or b)

α_j = Thermal diffusivity of j

η_s, η_p = Non radiative conversion efficiencies for the absorbing
solid and pyroelectric

The boundary conditions of temperature and heat flux continuity at all interfaces are given by

$$T_i(\omega_0, \text{boundary}) = T_j(\omega_0, \text{boundary})$$

(1.8a)

$$k_i \frac{\partial}{\partial x} T_i(\omega_0, \text{boundary}) = k_j \frac{\partial}{\partial x} T_j(\omega_0, \text{boundary}) \quad (1.8b)$$

So the complex solutions to equations (1.7) are

$$T_g(\omega_0, x) = C_1 \exp(-\sigma_g x) \quad (1.9a)$$

$$T_s(\omega_0, x) = \left(\frac{I_0 \beta_s \eta_s}{2k_s(\sigma_s^2 - \beta_s^2)} \right) \exp(\beta_s x) + C_2 \exp(\sigma_s x) + C_3 \exp(-\sigma_s x) \quad (1.9b)$$

$$T_p(\omega_0, x) = \left[\frac{I_0 \beta_p \eta_p \exp(-\beta_p L_s)}{2k_p(\sigma_p^2 - \beta_p^2)} \right] \exp[\beta_p (x + L_s)] + C_4 \exp(\sigma_p x) \\ + C_5 \exp(-\sigma_p x) \quad (1.9c)$$

$$T_b(\omega_0, x) = C_6 \exp(\sigma_b x) \quad (1.9d)$$

$$\text{where } \sigma_j \equiv (l+i) a_j \text{ and } a_j = \left(\frac{\omega_0}{2\alpha_j} \right)^{1/2} \quad (1.10)$$

and a_j is the thermal diffusion coefficient of the respective media.

The quantity of interest is the function for the temperature variations in the pyroelectric $T_p(\omega_0, x)$. The coefficients in Eq. (1.9c) can be determined using the boundary conditions (1.8a) and (1.8b). So after a considerable amount of algebraic manipulation, the general expression for $\theta_p(\omega_0)$ is obtained as

$$\begin{aligned}
\theta_p(\omega_0) = & \left(\frac{I_0}{2\sigma_p \omega_0} \right) \left\{ \left(\frac{\beta_s \eta_s}{k_s (\beta_s^2 - \sigma_s^2)} \right) \left(\{ [\exp(\sigma_p L_p) - 1](b_{bp} + 1) - [1 - \exp(-\sigma_p L_p)](b_{bp} - 1) \} \right. \right. \\
& \times \{ 2(b_{sg} \gamma_s + 1) - [(\gamma_s + 1)(b_{sg} + 1)\exp(\sigma_s L_s) + (\gamma_s - 1)(b_{sg} - 1)\exp(-\beta_s L_s)] \\
& \left. \left. \exp(-\beta_s L_s) \right\} \right) + \left(\frac{\beta_p \eta_p \exp(-\beta_s L_s)}{k_p (\beta_p^2 - \sigma_p^2)} \right) \left\{ [(\{ [\exp(\sigma_p L_p) - 1](b_{bp} + 1) - \right. \\
& [1 - \exp(-\sigma_p L_p)](b_{bp} - 1)\} (b_{ps} \gamma_p + 1) + \{ [\exp(\sigma_p L_p) - 1](b_{ps} + 1) + \\
& [1 - \exp(-\sigma_p L_p)](b_{ps} - 1)\} (b_{bp} - \gamma_p) \exp(-\beta_p L_p)) - \gamma_p^{-1} \{ (b_{bp} + 1)(b_{ps} + 1) \\
& \exp(\sigma_p L_p) + (b_{bp} - 1)(b_{ps} - 1) \exp(-\sigma_p L_p) \} [1 - \exp(-\beta_p L_p)] \} (b_{sg} + 1) \\
& \exp(\sigma_s L_s) + [(\{ [\exp(\sigma_p L_p) - 1](b_{bp} + 1) - [1 - \exp(-\sigma_p L_p)](b_{bp} - 1)\} \\
& (b_{ps} \gamma_p - 1) + \{ [\exp(\sigma_p L_p) - 1](b_{ps} - 1) + [1 - \exp(-\sigma_p L_p)](b_{ps} + 1)\} \\
& (b_{bp} - \gamma_p) \exp(-\beta_p L_p)) - \gamma_p^{-1} \{ (b_{bp} + 1)(b_{ps} - 1) \exp(\sigma_p L_p) \\
& + (b_{bp} - 1)(b_{ps} + 1) \exp(-\sigma_p L_p) \} [1 - \exp(-\beta_p L_p)] \times (b_{sg} - 1) \exp(-\sigma_s L_s) \} \}
\end{aligned}$$

$$\begin{aligned} & \div ((b_{sg} + 1) [(b_{bp} + 1)(b_{ps} + 1) \exp(\sigma_p L_p) + (b_{bp} - 1)(b_{ps} - 1) \exp(-\sigma_p L_p)] \\ & \exp(\sigma_s L_s) + (b_{sg} - 1) [(b_{bp} + 1)(b_{ps} - 1) \exp(\sigma_p L_p) + (b_{bp} - 1)(b_{ps} + 1) \\ & \exp(-\sigma_p L_p)] \exp(-\sigma_s L_s)) \end{aligned} \quad (1.11)$$

Further, substitution of Eq. (1.11) into Eq. (1.5) gives the expression for the complex pyroelectric voltage as a function of modulation frequency of light and optical, thermal and geometric parameters of the sample/pyroelectric system.

Special cases

Equation (1.11) demonstrates explicitly that the thickness averaged photopyroelectric signal is a function of both the optical and thermal parameters of the sample under investigation. The complicated dependence of the signal on the sample parameters makes it difficult to give a physical interpretation to the general case. Therefore several special cases are considered according to the optical opacity and transparency of the sample. The classification scheme used here is adopted from Rosencwaig and Gersho [127]. All cases considered here have been classified according to the relative magnitudes of three characteristic lengths in the solid and the pyroelectric namely

- i. Thickness, L_s or L_p
- ii. Optical absorption depth, μ_β or μ_{β_p} defined as

$$\mu_{\beta_j} \equiv \beta_j^{-1} \quad (1.12)$$

- iii. Thermal diffusion length, μ_s or μ_p defined as

$$\mu_j = a_j^{-1} = \left(\frac{2\alpha_j}{\omega_0} \right)^{1/2} \quad (1.13)$$

For the special cases of the photopyroelectric signal discussed below, the time dependent factor $\exp(i\omega_0 t)$ in Eq. (1.5) has been omitted, as it does not affect the amplitude or the phase lag of the complex envelope of the signal.

A. Optically opaque and thermally thick pyroelectric

This case occurs experimentally at high chopping frequencies $\omega_0 /$ or for thick detectors.

For this limit $\mu_{\beta_p} \ll L_p$, $\mu_p < L_p$ and $\mu_{\beta_s} < \mu_p$. So in Eq. (1.11), we set

$$\exp(-\beta_p L_p) \cong 0, \exp(-\sigma_p L_p) \cong 0 \text{ and } |\gamma_p| > 1$$

Then

$$\begin{aligned} V(\omega_0, \beta_s) = & \left(\frac{pI_0}{2k\varepsilon_0} \right) l \left(\frac{\beta_s \eta_s}{k_s (\beta_s^2 - \sigma_s^2) \sigma_p} \right) \{ 2(b_{sg} \gamma_s + 1) - l(\gamma_s + 1)(b_{sg} + 1) \exp(\sigma_s L_s) \\ & + (\gamma_s - 1)(b_{sg} - 1) \exp(-\sigma_s L_s) \} \exp(-\beta_s L_s) \} + \left(\frac{\eta_p \exp(-\beta_s L_s)}{k_p \beta_p \sigma_p} \right) \\ & \{ (b_{sg} + 1)(b_{ps} \gamma_p + 1) \exp(\sigma_s L_s) + (b_{sg} - 1)(b_{ps} \gamma_p - 1) \exp(-\sigma_s L_s) \} l \\ & \div [(b_{sg} + 1)(b_{ps} + 1) \exp(\sigma_s L_s) + (b_{sg} - 1)(b_{ps} - 1) \exp(-\sigma_s L_s)] \quad (1.14) \end{aligned}$$

A. 1: Optically opaque sample ($\mu_{\beta_s} \ll L_s$)

In Eq. (1.14), we set $\exp(-\beta_s L_s) \cong 0$

Case A.1(a): Thermally thin sample ($\mu_s \gg L_s$, $\mu_s \gg \mu_{\beta_s}$)

In Eq. (1.14), set $\exp(\pm \sigma_s L_s) \approx 1$ and $|\gamma_s| \gg 1$

$$\text{So } V(\omega_0) = A \left(\frac{\eta_s \alpha_p}{k_p (1 + b_{gp}) \omega_0} \right) \exp(-i\pi/2) \quad (1.15)$$

$$\text{where } A = \frac{pI_0}{2k\varepsilon_0} \quad (1.16)$$

Eq. (1.15) shows that the photopyroelectric signal voltage is independent of β_s . This behaviour is termed as photopyroelectric saturation. The signal depends on the thermal properties of both the gas and the pyroelectric and it varies with the chopping frequency as ω_0^{-1} and its phase lags by 90° to that of the reference signal.

Case A.1 (b): Thermally thick sample ($\mu_s \ll L_s, \mu_s > \mu_{\beta_s}$)

In Eq. (1.14) we set $\exp(-\sigma_s L_s) \cong 0$ and $|\gamma_s| > 1$

Assuming that $|\gamma_s| > b_{gs}$, Eq. (1.14) reduces to

$$V(\omega_0) = A \left(\frac{\eta_s \alpha_p}{k_p (1 + b_{sg}) \omega_0} \right) \exp \left[- \left(\frac{\omega_0}{2\alpha_s} \right)^{1/2} L_s \right] \exp \left[-i \left(\frac{\pi}{2} + \left(\frac{\omega_0}{2\alpha_s} \right)^{1/2} \right) \right] \quad (1.17)$$

In this limit the photopyroelectric signal, initially saturated with respect to the thermal properties of the contact gas, has now been replaced with those of the solid. Eq. (1.17) indicates that in this limit the photopyroelectric signal can be used, in principle to determine its thermal diffusivity α_s if the thickness L_s is known or vice versa.

Case A.1(c): Thermally thick sample ($\mu_s \ll L_s, \mu_s < \mu_{\beta_s}$)

In Eq. (1.14), set $\exp(-\sigma_s L_s) \cong 0$ and $|\gamma_s| < 1$

Here two possibilities can occur

(i) $|\gamma_s| < b_{sg} < 1$, then

$$V(\omega_0, \beta_s) = A\beta_s \left(\frac{\eta_s b_{sg} \alpha_s \sqrt{\alpha_p}}{k_p (1+b_{sp}) \omega_0^{3/2}} \right) \exp \left[- \left(\frac{\omega_0}{2\alpha_s} \right)^{1/2} L_s \right] \exp \left\{ -i \left[\left(\frac{\omega_0}{2\alpha_s} \right)^{1/2} L_s - \pi/4 \right] \right\} \quad (1.18)$$

This is called thermal transmission spectroscopy. As long as $\mu_s < \mu_{\beta_s}$, the exponential tail of the heat wave generated within μ_s in the sample is communicated to the pyroelectric transducer, thus producing a signal linear in β_s and of small magnitude. Therefore, the technique can be used in this limit as a spectroscopy, yielding signal information similar to the absorption spectra.

The other possibility considered is

(ii) $b_{sg} < |\gamma_s| < 1$

So Eq. (1.14) becomes

$$V(\omega_0, \beta_s) = A\beta^2 \left(\frac{\eta_s \alpha_p \alpha_s}{k_p (1+b_{sp}) \omega_0^2} \right) \exp \left[- \left(\frac{\omega_0}{2\alpha_s} \right)^{1/2} L_s \right] \exp \left[-i \left(\frac{\omega_0}{2\alpha_s} \right)^{1/2} L_s \right] \quad (1.19)$$

Eq. (1.18) predicts a spectral nonlinearity. i.e. $V(\omega_0, \beta_s) \propto \beta_s^2$. This dependence will distort the spectral information from the sample. Therefore it is regarded as undesirable.

A. 2: Optically transparent sample ($\mu_{\beta_s} > L_s$)

In this limit, $\exp(-\beta_s L_s) \cong 1 - \beta_s L_s$

Case A. 2(a): Thermally thin sample ($\mu_s \gg L_s, \mu_s > \mu_{\beta_s}$)

In Eq. (1.13), we set $\exp(\pm \sigma_s L_s) \cong 1$ and $|\gamma_s| > 1$

So Eq. (1.13) becomes

$$V(\omega_0, \beta_s) = A \left(\frac{\eta_p + (\eta_s - \eta_p) \beta_s L_s}{k_p (1 + b_{gp}) \omega_0} \right) \exp(-i\pi/2) \quad (1.20)$$

The photopyroelectric voltage is proportional to $\beta_s L_s$, provided that $\eta_s \neq \eta_p$. In the experimentally common case, where $\eta_s \sim \eta_p \sim 1$ and $b_{gp} < 1$, the signal carries neither optical nor thermal information about the samples and it is entirely generated by light absorption in the pyroelectric.

Case A. 2(b): Thermally thin sample ($\mu_s > L_s$, $\mu_s < \mu_{\beta_s}$)

In Eq. (1.14), set $\exp(\pm \sigma_s L_s) \cong 1 \pm \sigma_s L_s$ and $|\gamma_s| < 1$

Further, if we assume that

$$(i) |\gamma_s| \gg |\sigma_s L_s| \text{ i.e., } \mu_s^2 > \mu_{\beta_s} L_s$$

So Eq. (1.13) reduces to

$$V(\omega_0, \beta_s) = A \alpha_p \left(\frac{\eta_p + (\eta_s - \eta_p) \beta_s L_s}{k_p \omega_0} \right) \exp(-i\pi/2) \quad (1.21)$$

This case is similar to **A. 2(a)**, in that for $\eta_s \sim \eta_p \sim 1$, no optical or thermal information about the sample is obtained.

Now, if we assume that

$$(ii) |\gamma_s| \ll |\sigma_s L_s|, \text{ then}$$

$$V(\omega_0, \beta_s) = A \alpha_p \left[\frac{(\eta_p + \eta_s \beta_s L_s)(1 - \beta_s L_s)}{k_p \omega_0} \right] \exp(-i\pi/2) \quad (1.22)$$

Here, if $\eta_s \sim \eta_p \sim 1$, the photopyroelectric output will be proportional to

$[1 - (\beta_s L_s)^2]$ with a ω_0^{-1} frequency dependence. This limit is nonlinear in β_s and the spectral information from the system will be similar to distorted transmission spectra.

Case A. 2 (c): Thermally thick sample ($\mu_s < L_s, \mu_s < \mu_{\beta_s}$)

The approximations in Eq. (1.14) are $\exp(-\sigma_s L_s) \cong 0$ and $|\gamma_s| \ll 1$. The photopyroelectric output is

$$V(\omega_0, \beta_s) = A(1 - \beta_s L_s) \left(\frac{\eta_p}{k_p (1 + b_{sp}) \omega_0} \right) \exp(-i\pi/2) \quad (1.23)$$

In this limit, the technique is equivalent to optical transmission spectroscopy. This is of great experimental interest, because the photopyroelectric signal is proportional to $[1 - \beta_s L_s]$. Therefore the technique can yield information similar to the transmission spectrum.

Cases A. 1 (c, i) and A. 2 (c) are the only spectroscopically important cases which give direct information about the optical absorption coefficient of the sample material as a result of thermal and optical transmission respectively.

B. Optically opaque and thermally thin pyroelectric

This case is likely to occur at low chopping frequencies ω_0 and / or very thin pyroelectric films. Under this condition, $\mu_{\beta_s} \gg L_p$ and $\mu_p \gg \mu_{\beta_s}$.

On setting $\exp(-\beta_p L_p) \cong 0$, $\exp(\pm \sigma_p L_p) \cong 1 \pm \sigma_p L_p$; $|\gamma_p| \gg 1$ in Eq.

(1.14), we get the expression as

$$V(\omega_0, \beta_s) = A \left[\frac{\beta_s \eta_s L_p}{k_s (\beta_s^2 - \sigma_s^2)} \right] \{ 2(b_{sg} \gamma_s + 1) - [(\gamma_s + 1)(b_{sg} + 1) \exp(\sigma_s L_s) + (\gamma_s - 1)(b_{sg} - 1) \exp(-\sigma_s L_s)] \exp(-\beta_s L_s) \} + \left(\frac{\eta_p \exp(-\beta_s L_s)}{k_p \beta_p \sigma_p} \right)$$

$$\begin{aligned}
& \{ (b_{sg} + 1) [(b_{ps} \gamma_p + 1) \sigma_p L_p - \gamma_p^{-1} \{ (b_{bs} + 1) + (b_{ps} + b_{bp}) \sigma_p L_p \}] \exp(\sigma_s L_s) \\
& (b_{sg} - 1) [(b_{ps} \gamma_p - 1) \sigma_p L_p - \gamma_p^{-1} \{ (b_{bs} - 1) + (b_{ps} - b_{bp}) \sigma_p L_p \}] \exp(-\sigma_s L_s) \} \\
& \div \{ (b_{sg} + 1) [(b_{bs} + 1) + (b_{ps} + b_{bp}) \sigma_p L_p] \exp(\sigma_s L_s) + (b_{sg} - 1) [(b_{bs} - 1) \\
& + (b_{ps} - b_{bp}) \sigma_p L_p] \exp(-\sigma_s L_s) \} \quad (1.24)
\end{aligned}$$

There are six spectral limits of Eq. (1.24) involving relationships between μ_s , μ_{β_s} and L_s , identical to cases A.1 and A.2. For each limit, in the case of a thermally thin pyroelectric transducer, the simplified expression for $V(\omega_0, \beta_s)$, which results from Eq. (1.24) is similar to the respective expression in the case of the thermally thick detector previously discussed, with the substitutions $-1/\sigma_p$ replaced by L_p and $k_p \sigma_p$ with $k_b \sigma_b$. According to these substitutions, the cases of spectroscopic interest in the limit of a thermally thin pyroelectric are

Case B.1 (c, i): Thermal transmission mode

$$V(\omega_0, \beta_s) = -A \left(\frac{\eta_s \beta_s L_p b_{sg} \exp(-\sigma_s L_s)}{\sigma_s (k_b \sigma_b + k_s \sigma_s)} \right) \quad (1.25)$$

Case B.2 (c): Optical transmission mode

$$V(\omega_0, \beta_s) = A \left(\frac{\eta_p L_p (1 - \beta_s L_s)}{k_b \sigma_b + k_s \sigma_s} \right) \quad (1.26)$$

The frequency dependence of the photopyroelectric voltage in all cases (B) is consistently with a factor $\omega_0^{-1/2}$ lower than all cases in (A)

The results obtained shows some trends familiar from other thermal wave spectroscopies, such as photoacoustic and photothermal deflection spectroscopy as well as some unique features. The calculations show that the photopyroelectric voltage is governed by the interplay between the optical absorption in the sample and in the pyroelectric transducer itself. This suggests that it is experimentally advantageous to work with optically opaque transducers whose flat (i.e., photopyroelectrically saturated) spectral response does not interfere with the spectral measurements on the sample. Opaqueness can be achieved through coating the photopyroelectric surface with metallic thin layers (e.g. nickel) [128] or black absorbing materials [129].

The present theoretical considerations help to establish photopyroelectric spectroscopy as a valid spectroscopic technique, with high promise in the realm of flexible *in-situ* non-destructive probing of samples and in applications at very high frequencies as piezoelectric or pyroelectric thin films (such as PVF₂) [130]. These features set this technique ahead of photoacoustics and photothermal spectroscopies.

Mandelis, in his theory assumed total absorption of radiation by the pyroelectric sensor. Chirtoc and Mihăilescu in 1989 [131] put forward another theory to understand the role played by the finite reflectance at the sample-pyroelectric interface and the mechanisms responsible for the peak inversions observed in the reflection-mode PPE spectroscopy [132,133] since these questions have found no satisfactory answers in the framework of the former theory. It has been shown that the assumption of an arbitrary value for the reflectance completely changes the physical nature of the PPE effect, featuring simultaneous optical absorption and transmission

characteristics. Hence it creates a very diverse experimental opportunities for optical and thermal investigations of solid, liquid or even gaseous substances.

1.3 APPLICATIONS OF PHOTOPYROELECTRIC SPECTROSCOPY

The pyroelectric (PE) property offers the possibility to use PE materials for a number of applications. In fact PE sensors present five main advantages that make them suitable for many applications as has been described already.

The advantages of PE detectors make the photopyroelectric technique an ideal one for the thermal and optical characterization of samples ranging from metals to insulators. Now we will discuss some of the important applications of the photopyroelectric technique.

1.3.1. PPE Spectroscopy in Semiconductors

In 1984, Coufal and Mandelis [101, 102] used for the first time, thin polyvinylidene difluoride (PVDF) films for photothermal wave spectroscopic detection. Shortly thereafter, Coufal showed that photopyroelectric spectroscopy can be a very sensitive qualitative tool for thin film spectroscopic applications [103]. Mandelis *et al.* [104] used the PPE spectroscopy for electronic defect center characterization of crystalline n-CdS. These authors performed several experiments in open circuit as well as in conjunction with photocurrent spectroscopy in the presence of a.c. or d.c. transverse electric field. This study [105] showed the potential of the technique to give information concerning non-radiative de-excitation mechanisms at defect centers. Tanaka [144] and Tanaka *et al.* [105] showed that frequency domain PPE spectroscopy is also very promising for qualitative analysis.

PPE spectroscopy was also used for the characterization of thin semiconducting films. Mandelis *et al.* [105] have performed spectroscopic measurements of an α -Si: H thin film on quartz. These authors further compared their experimental PPE spectra with similar spectra obtained by conventional widely used photothermal deflection spectroscopy (PDS). It was shown that PPE spectroscopy has the ability for easy and consistent experimental acquisition of non-radiative quantum efficiency spectra, a property not shown by PDS. It is the necessity for a coupling fluid that is partly the cause of the lack of spectroscopic applications of PDS at cryogenic temperatures. Another disadvantage is the pump-probe beam alignment requirement for PDS detection. This frequently led to the need for three-dimensional models to interpret the data quantitatively. The consideration of these advantages led to the development of PPE spectroscopy.

PPE technique has been used to study the thermal properties of In-Te glasses during electrical switching by Rajesh *et.al.* [146] Lot more studies are done on semiconducting glasses by Rajesh *et.al* [145, 147, 148].

1.3.2. PPE Spectroscopy in Paramagnetic and Ferromagnetic Materials

In 1982, Melcher and Arbach [107] reported the use of pyroelectric sensors to detect the temperature gradients associated with magnetic resonance absorption in thin films and layers of paramagnetic and ferromagnetic materials. Photopyroelectric technique to study the magnetic phase transitions in ferroelectrics and itinerant electron antiferromagnetic materials were first done by Dădarlat *et al.*, [108] in 1990. In their paper these authors have reported the application of PPE technique for the study of magnetic phase transitions in $\text{Ni}_{100-x}\text{Cu}_x$ alloys with $x = 28$ to 33%. The samples were found to exhibit magnetic phase transitions (ferromagnetic-

paramagnetic). According to Dâdarlat *et al.*, [108] due to the features of the PPE method, the high signal to noise ratios that were obtained allowed higher sensitivities for monitoring phase transitions in itinerant electron antiferromagnets than classical magnetic and electronic measurements.

In another work, Dâdarlat *et al.*, [109] demonstrated the ability of the PPE method to detect the phase transitions in solids. He made measurements on TGS, which exhibited a ferroelectric-paraelectric phase transition at 49 °C and NiCu₃₀ had a ferromagnetic-paramagnetic phase transition at 50 °C. It has shown that the PPE voltage amplitude clearly reflects the phase transition. He made the inference that the thermally thin and thick conditions largely influence the results.

1.3.3. PPE Spectroscopy in Liquid Crystals

Marinelli *et al.* [110] used the photothermal front detection configuration (Fig. 1.4) to perform measurements on liquid crystal samples in the range 0.2 Hz to 200 kHz. The sample was 9CB liquid crystal and the author studied the PPE signal as a function of modulation frequency. It has been proved that with the PPE technique, it is possible, at a given frequency, to obtain the temperature dependence on the thermal parameters of the sample, which is particularly interesting in the case of phase transition studies.

Marinelli *et al.* [111] have also performed several experiments comparing the photoacoustic and photopyroelectric technique for the characterization of liquid crystal second order phase transitions. In their measurements they evaluated simultaneously thermal conductivity, specific heat and thermal diffusivity of 9CB liquid crystal that undergoes a second order phase transition at 47.9 °C from Smectic-A (SA) to Nematic (N) phase [112]. The variation of PPE signal amplitude and phase as a function of temperature for the liquid crystal sample has been plotted. It is seen that in the plot, the obtained dip for the PPE phase at the phase transition

temperature, because of the “critical slowing down” of thermal fluctuations [111, 113] is about 160^0 , while in PA it was only 4^0 . This proves the superior sensitivity of the PPE technique over PA. Apart from the sensitivity factor, the PPE technique presents a better signal-to-noise (SNR) ratio, which makes this an ideal one for studies in liquid crystals.

1.3.4. PPE Spectroscopy to Investigative Ferroelectric Phase Transitions

Phase transitions are always associated with configurational changes within the system. Magnetic phase transitions are driven by the alignment of unpaired spins in a specified direction and one usually does not observe any changes in the atomic configuration. On the other hand, several other types of phase transitions like para-ferroelectric transitions are generally associated with atomic rearrangement or structural changes. The change of structure at a phase transition in a solid can occur in two distinct ways. Firstly, there are transitions where the atoms of a solid reconstruct a new lattice as in the case of amorphous solid to crystalline state. Secondly, there are transitions where a regular lattice is distorted slightly without in any way disrupting the linkage of the networks. This can occur as a result of small displacements in the lattice position of single atoms or molecular groups or the ordering of atoms or molecules among various equivalent positions. Most of the ferroelectric phase transitions belong to the second group. The displacive type transitions are often driven by the freezing out of a vibrational mode called soft mode. In the case of ferroelectric transition, the soft mode is an optical phonon belonging to the centre of the Brillouin zone while in the case of an antiferroelectric transition, is a zone boundary phonon. Soft acoustic phonons are associated with ferroelastic transitions.

The PPE technique has been employed by different authors for the study of phase transitions in solids [11, 12, 42, and 103]. The para to –

ferroelectric phase transition of triglycine sulfate is studied using PPE technique [150]. Incommensurate phase transition which is an interesting phenomena is also studied using PPE technique by C. P. Menon *et.al.* [151]

1.3.5 PPE Gas Sensors

Photo thermal and photo acoustic techniques have been used successfully in optical and thermo physical characterization of solids [114-118]. Recent developments in monitoring and measuring the properties of gases using photothermal techniques have attracted much attention for environmental quality control and manufacturing safety reasons [119-122]. Christofides and Mandelis [123] used the photopyroelectric gas sensor, a new type of solid-state devices for the detection of minute concentrations of hydrogen gas under environmental flow-through conditions. The sensor was made with PVDF film sputter coated with Pd. An infrared beam from a semiconductor laser diode was coupled to an optical fiber and irradiated the PVDF, thus generating a carrier wave a.c. photopyroelectric voltage. Sensitivity to exposures in a hydrogen partial pressure has been demonstrated down to concentrations as small as 40 ppm, in a flowing H₂ + N₂ mixture.

A newly developed [122] thermal wave resonant cavity (TWRC) sensor using a pyroelectric thin film transducer (pvdf), proved to offer a powerful method for measuring thermal diffusivities of gases with very high precision and gas species resolution [121, 122, 124].

_ This section on photopyroelectric effect would not be complete if we did not emphasize the fact that high sensitivity of the PPE detector in temperature change is a great challenge for instrumentalists. Juhl and Bimberg [125] have recently proved that with calorimetric absorption and transmission spectroscopy one can achieve spectroscopic sensitivities of $\beta = 10^{-8}$. So we can say that from an experimental and instrumental point of

view, the progress of the experimental technique has been consistent and encouraging. However, the full potentiality of the PPE technique for optical and thermal material characterization remains to be demonstrated by future experiments.

1.4 WORK PRESENTED IN THE THESIS

In this thesis we present the work done and results obtained on the thermal properties a selected variety of solids. Photopyroelectric technique has been employed to determine thermal transport properties of two crystals, Dicalcium Leas Propionate and Potassium selenate, which undergo ferroelectric phase trnsions. The thermal properties of an oxide ceramic LaMnO_3 which exhibit giant Magneto resistance have been measured and reported. Again the thermal properties of two ceramic composites have been measured and reported. Even though the main experimental technique used is the PPE technique, other experimental methods such as thermal analysis, FTIR, X-ray diffraction etc. have been used wherever necessary. The following chapters of the thesis contain the details of the experiment, results obtained and discussion of the following results.

REFERENCES

1. J. R. Barker, and T. Rothem, *Chem. Phys.* **68**, 331 (1982)
2. J. R. Barker and Toselli B. M. in *Photothermal Investigations in Solids and Fluids* Sell, J. A. Editor, Academic Press, Inc. New York (1989)
3. J. V. Beitz, M. M. Doxtader, V. A. Maroni, S. Okajima and D. T. Reed, *Rev. Sci. Instrum.* **61**, 1395 (1990)
4. A. G. Bell, *Am. J. Sci.* **20**, 305 (1880)
5. A. G. Bell, *Philos. Mag.* **11**, 510 (1881)
6. H. H. Belz, H. Gutberlet, B. Schallert, B. Schrader, *Appl. Spectrosc.* **41**, 1009 (1987)
7. C. M. Betteridge and Meylor P. J. *CRC Critical Reviews in Analytical Chemistry* **14**, 267 (1984)
8. S. E. Bialkowski, *Chem. Phys. Lett.* **151**, 88 (1988)
9. S. E. Bialkowski and Z.-F. He, *Anal. Chem.* **60**, 2674 (1988)
10. S. E. Bialkowski, X. Gu, P. E Poston, L. S. Powers, *Appl. Spectrosc.* **46**, 1335 (1992)
11. A. C. Boccara, D. Fournier, and Badoz, *J. Appl. Phys. Lett.* **36**, 130 (1979)
12. G. Busse. in *Photoacoustic, Photothermal and Photochemical Processes at Surfaces and Thin Films* Hess, P., Editor, Springer-Verlag, New York (1989)
13. R. J. Collier, C. B. Burckhardt, and L. H. Lin, *Optical Holography* Academic Press, New York (1971)
14. C. C Davis and S. J. Petuchowski, *Appl. Opt.* **20**, 2539 (1981)
15. N. J. Dovichi and J. M. Harris, *Anal. Chem.* **51**, 728 (1979)
16. N. J. Dovichi and J. M. Harris, *Anal. Chem.* **53**, 106 (1981)

17. N. J. Dovichi, *CRC Critical Reviews in Analytical Chemistry* **17**, 357 (1987)
18. N. J. Dovichi, *Rev. Sci. Instrum.* **61**, 3653 (1990)
19. H. J. Eichler, P. Ghnter, and D. W. Pohl, *Laser-Induced Dynamic Gratings* Springer-Verlag, New York (1986)
20. H. L. Fang, and R. L. Swofford, in *Ultrasensitive Laser Spectroscopy* Kliger, D. S., Editor, Academic Press, New York (1983)
21. D. Fournier, A. C. Boccara, N. M. Amer, and R. Gerlach, *Appl. Phys. Lett.* **37**, 519 (1980)
22. D. Fournier and A. C. Boccara, in *Photothermal Investigations in Solids and Fluids* Sell, J. A. Editor, Academic Press, Inc. New York (1988)
23. F. K. Fotiou, and M. D. Morris, *Appl. Spectrosc.* **40**, 704 (1986)
24. D. M. Friedrich, *Ultrasensitive Laser Spectroscopy* D. S Kliger, Editor, Academic Press, New York (1983)
25. M. C. Gagne, P. Galarneau, and S. L. Chin, *Canadian Journal of Physics* **64**, 1117 (1986)
26. J. P. Gordon, R. C. C. Leite, R. S Moore, S. P. S. Porto, and J. R. Whinnery, *Bull. Am. Phys. Soc.* **9**, 501 (1964)
27. J. P. Gordon, R. C. C. Leite, R. S. Moore, S. P. S. Porto, and J. R. Whinnery, *J. Appl. Phys.* **36**, 3 (1965)
28. F. R. Grabiner, D. R. Siebert, and G. W. Flynn, *Chem. Phys. Lett.* **17**, 189 (1972)
29. J. M. Harris, *Optics News* (October) **8** (1986)
30. K. F. Herzfeld, and T. A. Litovitz, *Absorption and Dispersion of Ultrasonic Waves* Academic Press, NY (1959)
31. P. Hess, Editor *Photoacoustic, Photothermal and Photochemical Processes in Gases* Springer-Verlag, New York (1989a)

32. P. Hess, Editor *Photoacoustic, Photothermal and Photochemical Processes at Surfaces and Thin Films* Springer-Verlag, New York (1989b)
33. L. O. Hocker, M. A. Kovacs, C. K. Rhodes, G. W. Flynn, and A. Javan, *Phys. Rev. Lett.* **17**, 233 (1966)
34. C. Hu, and J. R. Whinnery, *Appl. Opt.* **12**, 72 (1973)
35. D. A. Hutchins, and A. C. Tam, *IEEE Trans. Ultrasonics, Ferroelectrics, and Frequency Control* **UFFC-33**, 429 (1986)
36. J. D. Ingle Jr., and S. R. Crouch, *Spectrochemical Analysis* Prentice Hall, Englewood Cliffs, NJ (1988)
37. W. B. Jackson, N. M. Amer, A. C. Boccara, and D. Fournier, *Opt. Lett.* **5**, 337 (1980)
38. W. B. Jackson, N. M. Amer, A. C. Boccara, and D. Fournier, *Appl. Opt.* **20**, 1333, (1981)
39. E. L. Kerr, and J. G. Atwood, *Appl. Opt.* **7**, 915 (1968)
40. T. Kitamori, and T. Sawada, *Spectrochem. Acta. Rev.* **14**, 275 (1991)
41. L. B. Kreuzer, *J. Appl. Phys.* **42**, 2934 (1971)
42. L. B. Kreuzer, N. D. Kenyon and C. K. N. Patel, *Science* **177**, 347 (1972)
43. H. M. Lai and K. Young, *J. Acoust. Soc. Am.* **76**, 2000 (1982)
44. L. D. Landau, and E. M. Lifshitz, *Fluid Mechanics* Addison-Wesley, Reading, MA (1959)
45. M. E. Long, R. L. Swofford, and A. C. Albrecht, *Science* **191**, 183 (1976)
46. G. R. Long, and S. E. Bialkowski, *Anal. Chem.* **57**, 1079 (1985)
47. P. R. Longaker, and M. M. Litvak, *J. Appl. Phys.* **40**, 4033 (1969)
48. A. Mandelis, Editor *Photoacoustic and Thermal Wave Phenomena in Semiconductors* North-Holland, New York (1987)

49. A. Mandelis, in *Photoacoustic, Photothermal and Photochemical Processes at Surfaces and Thin Films*, Hess, P., Editor, Springer-Verlag, New York (1989)
50. F. A. McDonald, *Can. J. Phys.* **64**, 1023 (1986)
51. E. A. McLean, L. Sica, and A. Glass, *J. Appl. Phys. Lett.* **13**, 369 (1968)
52. P. L. Meyer and M. W. Sigrist, *Rev. Sci. Instrum.* **61**, 1779 (1990)
53. K. Mori, T. Imashaka, N. Ishibashi, *Anal. Chem.* **54**, 2034 (1982)
54. M. D. Morris, and F. K. Fotiou, in *Photothermal Investigations in Solids and Fluids* J. A. Sell, Editor, Academic Press, Inc. New York (1989)
55. J. C. Murphy and L. C. Aamodt, *J. Appl. Phys.* **51**, 4580 (1980)
56. J. C. Murphy, and L. C. Aamodt, *Appl. Phys. Lett.* **38**, 196 (1981)
57. J. C. Murphy, J. W. Maclachlan, and L. C. Aamodt, *IEEE Trans. Ultrasonics, Ferroelectrics, and Frequency Control* **UFFC-33** 529 (1986)
58. P. -E. Nordal, and S. O. Kanstad, *Phys. Scr.* **20**, 659 (1979)
59. R. A. Nyquist, M. A. Leugers, M. L. McKelvy, R. R. Papenfuss, C. L. Putzig, and L. Yurga, *Anal. Chem.* **62**, 223R (1990)
60. Y.-H. Pao, editor *Opto-acoustic Spectroscopy and Detection* Academic Press, New York (1977)
61. C. K. N. Patel, R. J. Kerl and E. G. Burkhardt, *Phys. Rev. Lett.* **38**, 1204 (1977)
62. C. K. N. Patel, and A. C. Tam, *Reviews of Modern Physics* **53**, 517 (1981)
63. J. G. Parker, *Appl. Opt.* **12**, 2974 (1973)
64. M. J. Pelletier, H. R. Thornsheim and J. M. Harris, *Anal. Chem.* **54**, 239 (1982)
65. M. J. Pelletier and J. M. Harris, *Anal. Chem.* **54**, 1537 (1983)
66. C. L. Putzig, M. A. Leugers, M. L. McKelvy, G. E. Mitchell, R. A. Nyquist, R. R. Papenfuss and L. Yurga, *Anal. Chem.* **62**, 223R (1990)

67. A. Rosencwaig, in *Opto-acoustic Spectroscopy and Detection* Pao, Y.-H., editor, Academic Press, New York (1977)
68. A. Rosencwaig, *Photoacoustics and Photoacoustic Spectroscopy* John Wiley and Sons, Inc. New York (1980)
69. J. A. Sell, Editor, *Photothermal Investigations in Solids and Fluids* Academic Press, Inc. New York (1989)
70. D. R. Siebert, F. R. Grabiner, G. W. Flynn, *J. Chem. Phys.* **60**, 1564 (1974)
71. M. Slatkine, *Appl. Opt.* **20**, 2880 (1981)
72. D. Solomini, *J. Appl. Phys.* **12**, 3314 (1966)
73. J. C. Stephenson, R. E. Wood, C. B. Moore, *J. Chem. Phys.* **48**, 4790 (1968)
74. J. Stone, *J. Opt. Soc. Am.* **62**, 327 (1972)
75. J. Stone, *Appl. Opt.* **12**, 1828 (1973)
76. A. C. Tam, in *Ultrasensitive Laser Spectroscopy* D. S. Kliger, Editor, Academic Press, New York (1983)
77. A. C. Tam, *Infrared Physics* **25**, 305 (1985)
78. A. C. Tam, *Reviews of Modern Physics* **58**, 381 (1986)
79. A. C. Tam, in *Photothermal Investigations in Solids and Fluids* J. A. Sell, Editor, Academic Press, Inc. New York (1989)
80. A. J. Twarowski and D. S. Kliger, *Chem. Phys.* **20**, 253 (1977a)
81. A. J. Twarowski and D. S. Kliger, *Chem. Phys.* **20**, 259 (1977b)
82. M. L. Viengerov, *Dokl. Akad. Nauk SSSR* **19**, 687 (1938)
83. J. R. Whinnery, *Acc. Chem. Res.* **7**, 225 (1974)
84. J. T. Yardley and C. B. Moore, *J. Chem. Phys.* **45**, 1066 (1966)
85. A. Yariv, *Optical Electronics* 3rd Edition, Holt, Rinehart and Winston, New York (1985)

86. V. P. Zharov, *Laser Opto-acoustic Spectroscopy in Chromatography* in *Laser Analytical Spectrochemistry*, V. P. Letokhov, Editor Adam Hilger, Boston, MA (1986)
87. V. P. Zharov, and V. S. Letokhov, *Laser Optoacoustic Spectroscopy* Springer-Verlag, New York (1986)
88. X. R. Zhu, D. J. McGraw and J. M. Harris, *Anal. Chem.* **64**, 710A (1992)
89. A. Rosencwaig, *Opt. Commun.* **7**, 305 (1973)
90. A. Rosencwaig, *Anal. Chem.* **47**, 592A (1975)
91. A. Rosencwaig in *Advances in Electronics and Electron Physics*, Vol. 46, edited by L. Marton, (Academic Press, New York, 1978) pp. 207-31
92. C. A. Bennett and R. R. Patty, *Appl. Opt.* **21**, 49 (1982)
93. J. Shen and A. Mandelis, *Rev. Sci. Instru.*, **66**, 4999 (1995)
94. J. Shen, A. Mandelis and B.D. Alotsius, *Int. J. Thermophys.* **17**, 1241 (1996)
95. J. Shen, A. Mandelis and T. Ashe, *Int. J. Thermophys.* **19**, 579 (1998)
96. J. A. P. Lima, E. Marin, M.G. Silva, M. S. Sthel, S. L. Cardoso, D. F. Takeuti, C. Gatts, H. Vargas, C. E. Renzende and L. C. M. Miranda, *Rev. Sci. Instru.* **71**, 2928 (2000)
97. J. A. P. Lima, E. Marin, M.G. Silva, M. S. Sthel, S. L. Cardoso, H. Vargas and L. C. M. Miranda, *Rev. Sci. Instru.*, **72**, 1 (2001)
98. J. A. P. Lima, E. Marin, O. Correa, M.G. Silva, S. L. Cardoso, C. Gatts, C.E. Renzende, H. Vargas, and L. C. M. Miranda, *Meas. Sci. Tech.* **11**, 1522 (2000)
99. J. A. P. Lima, M.G. Silva, M. S. O. Massunaga, E. Marin, H. Vargas, and L. C. M. Miranda, *J. Appl. Phys.* **91**, 5581 (2002)
100. E. H. Putley, *Semiconductors and Semimetals*, edited by R. K. Willardson and A. C. Beer, Vol.5 (Academic, New York, 1970) 259.
101. H. Coufal, *Appl. Phys. Lett.* **44**, 59 (1984)

102. A. Mandelis, *Chem. Phys. Lett.* **108**, 388 (1984)
103. H. Coufal, *Appl. Phys. Lett.* **45**, 516 (1984)
104. A. Mandelis, W. Lo and R. W. Lo and R. Wagner, *Appl. Phys. A* **44**, 123 (1987)
105. A. Mandelis, R. E. Wagner, K. Gandhi, R. Baltman and P. Dao, *Phys. Rev. B* **39**, 5254 (1989)
106. H. Tanaka, *Photoacoustic and thermal wave phenomenon in semi conductors*, edited by A. Mandelis (North Holland, New York, 1987) ch.16
107. R. L. Melcher and Arbach, *Appl. Phys. Lett.* **40**, 911 (1982)
108. D. Dădarlat, M. Chirtoc, C. Neamtu and D. Bicanic, *J. Phys. Chem. Solids* **00**, 000 (1990)
109. D. Dădarlat, M. Chirtoc and D. Bicanic, *6th International Topical Meetings on Photoacoustics and Photothermal Phenomena II*, edited by Murphy *et al.* Vol. **62**, 300 (1991)
110. M. Marinelli, F. Mercuri. U. Zammit and R. Pizzoferrato, *Appl. Phys. Lett.* **65**, 2663 (1994)
111. M. Marinelli, U. Zammit, F. Mercuri, R. Pizzoferrato, *J. Appl. Phys.* **72**, 1096 (1991)
112. F. Murthas, M. G. Mecozzi, M. Marinelli, V. Zammit, R. Pizzoferrato, F. Scudieri, S. Martellucci and M. Marinelli, *6th International Topical Meetings on Photoacoustics and Photothermal Phenomena II*, edited by Murphy *et al.* Vol. **62**, 208 (1992)
113. V. Zammit, M. Marinelli, R. Pizzoferrato, F. Scudieri and S. Martellucci, *Photoacoustics and Photothermal Phenomena II*, Vol. **62** (1993).
114. A. Mandelis, J. Vanniasinkam and S. Budhudu, *Phys. Rev. B* **48**, 6808 (1993)
115. A. K. Ghosh and B. K. Chaudhari, *J. Appl. Phys.* **80**, 5292 (1996)

116. J. Philip, *Rev. Sci. Instrum.* **67**, 3621 (1996).
117. J. Shen, K. Fjeldsted, J. Vanniasinkam and A. Mandelis, *Opt. Mater.* **4**, 823 (1995)
118. M. Munidassa, F. Funak and A. Mandelis, *J. Appl. Phys* **83**, 3495 (1998)
119. A. Bozoki, J. Sneider, G. Szabo, A. Miklos, M. Serenyi, G. Nagy and M. Feher, *Appl. Phys. B: Lasers Opt.* **63**, 399 (1996)
120. M. Feher, Y. Jiang, J. P. Maier and A. Miklos, *Appl. Opt.* **33**, 1655 (1994)
121. J. Shen, A. Mandelis and H. Tsai, *Rev. Sci. Instrum.* **69**, 197 (1998)
122. J. Shen, A. Mandelis and B. Aloysius, *Int. J. Thermophys.* **69**, 197 (1998)
123. C. Christofides and A. Mandelis, *J. Thermophys.* **18**, 1241 (1996)
124. C. H. Wang and A. Mandelis, *Rev. Sci. Instrum.* **70**, 2372 (1999)
125. Juhl and Bimberg, *J. Appl. Phys.* **64**, 303 (1988)
126. A. Mandelis and M. M. Zver, *J. Appl. Phys.* **57**, 4421(1985)
127. A. Roscencwaig and A. Gersho, *J. Appl. Phys.* **47**, 64 (1976)
128. Kynar™ Piezo Film Technical Manual, (Pennwatt Corp. Pennsylvania, 1983) 17.
129. W. R Belvin and J. Geist, *Appl. Opt.* **13**, 1171 (1973)
130. L. Bui, H. J. Shaw and L. T. Zitelli, *Electron Lett.* **12**, 393 (1976)
131. M. Chirtoc and G. Mihăilescu, *Phys. Rev B* **40**, 9606 (1989)
132. M. Chirtoc and I. Chirtoc, *Infrared Phys.* **29**, 847 (1989)
133. M. Chirtoc, D. Dadarlat, I. Chirtoc and D. Bicanic, *Spectrosc. Lett.* **21**, 413 (1988)
134. S. B. Peralta, S. C. Ellis, C. Christofides, A. Mandelis, H. Sang and B. Faranbakhsh, *Res. Nondestr. Eval.* **3**, 69 (1991).
135. J. F. Power and A. Mandelis, *Rev. Sci. Instrum.* **58**, 2018 (1987)
136. J. F. Power and A. Mandelis, *Rev. Sci. Instrum.* **58**, 2024 (1987)

137. J. F. Power and A. Mandelis, *Rev. Sci. Instrum.* **58**, 2033 (1987)
138. J. F. Power, *Appl. Spectrosc.* **45**, 1240 (1991)
139. J. F. Power, *Appl. Spectrosc.* **45**, 1252 (1991)
140. H. Coufal and A. Mandelis, *Ferroelectrics* **118**, 379 (1991)
141. M. Marinelli, F. Mercuri. U. Zammit and R. Pizzoferrato, *Appl. Phys. Lett.* **65**, 2663 (1994)
142. C. Christofides, K. Gandhi and A. Mandelis, *Meas. Sci. Technol.* **1**, 1363 (1990).
143. H. Coufal, R. Grygier, D. Horne and J. Fromm, *J. Vac. Sci. Technol. A* **4** 2988 (1986).
144. K. Tanaka, Y. Ichimura and K. Sindoh, *J. Appl. Phys.* **63**, 1815 (1988).
145. J. Philip, R. Rajesh and C. Preethy Menon, *Appl. Phys. Lett.* **78**, 745 (2001).
146. R. Rajesh and J. Philip, *Ind. J. of Pure & Appl. Phys.* **38** , 827 (2000).
147. R. Rajesh and J. Philip, *J. of Mat. Sci.* **38**, 1513 (2003)
148. R. Rajesh and J. Philip, *Semicond. Sci. & Tech.* **18**, 133 (2003)
149. A. C. Tam, *Rev. of Mod. Phys.*, **58**, 381 (1986).
150. C. P. Menon, J. Philip, A. Deepthy and H. L. Bhat, *Mat. Res. Bull.* **36**, 2407 (2001).
151. C. P. Menon and J. Philip, *Ferroelectrics* **282**, 1 (2003).

Chapter 2

Experimental Methods

2.1 INTRODUCTION

When a material goes through a phase transition, its thermal parameters often show anomalous temperature dependence over the transition temperature. In particular a peak structure is observed in the specific heat capacity c_p , and sometimes in the thermal conductivity k , while a dip is often observed in the case of thermal diffusivity α . The nature of the variation of thermal conductivity is dependent on the type of transition that the material undergoes. The determination of the critical exponents of the anomalies of the thermal parameters is useful for the determination of the universality class of the phase transition. Techniques which allow for the simultaneous determination of all the thermal parameters of a material in the vicinity of a phase transition are therefore very attractive for the characterization of a phase transition. One of the major requirements of such a technique is that it should introduce only small temperature perturbations inside the sample, in view of the fact that strong temperature dependence for the thermal parameters can be expected in the vicinity of a phase transition. Different techniques such as photothermal deflection technique, photo acoustic (PA) technique, photopyroelectric (PPE) technique etc. are used for the measurement of thermal parameters of solid samples [1-9]. In this, the photopyroelectric technique is a very useful method for the simultaneous measurement of thermal transport properties such as thermal diffusivity (α) thermal effusivity (e) specific heat capacity (c_p) and thermal conductivity (k) near phase transitions. We have used the PPE technique for our measurements through out this work. The advantage of PPE detection over

gas coupled PAS is that the cell geometry is simpler in design and does not have any mechanical resonance effects in the frequency response.

The PPE technique is the only photothermal technique based on the direct detection of photothermal heating or the temperature changes due to optical irradiation directly. Therefore, it has a number of advantages over other detection schemes involving secondary mechanisms [10-11], since each conversion step in the signal detection degrades the overall signal to noise ratio, sensitivity and band width performance and complicates the theoretical interpretation of results. A PPE experiment is rather simple to design and the specimen needs no special preparation. The materials that can be investigated range from weakly absorbing solids like thin films [2,12-14] or liquids [15], semiconductors [16], surfaces and absorbates [10,13,17-18] to strongly absorbing solids [19] and liquids [20-21] or diffusing materials [1].

Mandelis and Zver in 1985 [8] put forward a one-dimensional analysis of the photopyroelectric model of a solid sample in intimate contact with a pyroelectric thin film, supported on a backing material. They were successful in deriving a general expression for the pyroelectric signal voltage developed in the detector due to light absorption in the sample. The calculations showed that the photopyroelectric voltage is governed by the interplay between the optical absorption in the sample and in the pyroelectric transducer itself. These theoretical calculations helped to establish photopyroelectric spectroscopy as a valid spectroscopic technique with high promise in the realm of non-destructive probing of samples with minimal preparation. These features set this technique ahead of photo acoustic and photothermal deflection spectroscopies in many respects.

In 1989, Chirtoc and Mihailiscu [5], generalized the theory developed by Mandelis and Zver to understand the role played by finite

reflectance at the sample- pyroelectric interface and the mechanism responsible for the peak inversions observed in the reflection mode PPE spectroscopy [20, 22]. These issues have not found satisfactory answers in the framework of the former theory. It is seen that the assumption of an arbitrary value for reflectance completely changes the physical nature of the PPE effect, featuring simultaneous optical absorption and transmission characteristics. Also, it creates very diverse experimental opportunities for optical and thermal investigations of solid, liquid and gaseous substances.

Complete characterization of a material requires the determination of thermal transport properties such as thermal conductivity and specific heat capacity. Conventional techniques used to measure thermal conductivity include the well known steady state and transient methods. Comparatively large size samples, typically of size 5mm^3 or higher are needed to avoid boundary effects while using these techniques. Moreover, large temperature rise often becomes necessary to obtain a reasonably good signal-to-noise ratio, leading to considerable temperature gradient being set up in the sample. However, techniques for high resolution measurements of specific heat capacity are well established [23, 24].

It has been shown that the photothermal techniques allow the simultaneous measurement of specific heat capacity c_{ps} and thermal conductivity k_s [25]. The photo acoustic technique has been used for the simultaneous determination of thermal diffusivity, thermal conductivity and heat capacity of liquid crystalline compounds [26], but some restrictions are imposed on this technique, because considerable complications arise in the design of the cell due to the presence of a coupling fluid. Marinelli *et al.* [25] were quite successful in developing a technique for determining thermal diffusivity, thermal conductivity and heat capacity simultaneously at low temperatures with the pyroelectric detector kept in vacuum. The boundary

conditions involved in the theory of this method are not easy to satisfy at temperatures above room temperature. We have used a photopyroelectric technique for the simultaneous determination of thermal conductivity and heat capacity of samples in which the pyroelectric transducer is in contact with a thermally thick backing medium [27]. The advantage of a thermally thick backing medium is that there will be sufficient heat exchange between the heated pyroelectric detector and the backing so that, signal fluctuations are reduced to a minimum.

2.2 PHOTOTHERMAL METHODS

In the following sessions a brief review of the different photothermal techniques developed to measure thermal properties of solid samples is given. In session 2.2.3, the methodology adopted in photopyroelectric technique is described.

2.2.1 Photo Thermal Deflection Effect

The photothermal deflection (PD) effect, also called photothermal deflection spectroscopy (PDS) relies on the creation of a refractive index gradient in a medium surrounding the sample due to the absorption of radiation, typically from a modulated pump laser beam [28]. The refractive index gradient is directly related to the absorption of this radiation and subsequent relaxation to thermal energy, forming a gradient intensity and therefore in index. Fig.2.1 gives a diagram of a typical PDS experiment.

Here the pump and probe beams cross or nearly cross in the medium. The deflection of the probe is monitored with a position sensitive detector or a photo diode with a razor blade or an other aperture in front of it. Normally the detector is connected to a lock-in amplifier so that the deflection is detected synchronously with the modulation of the pump beam.

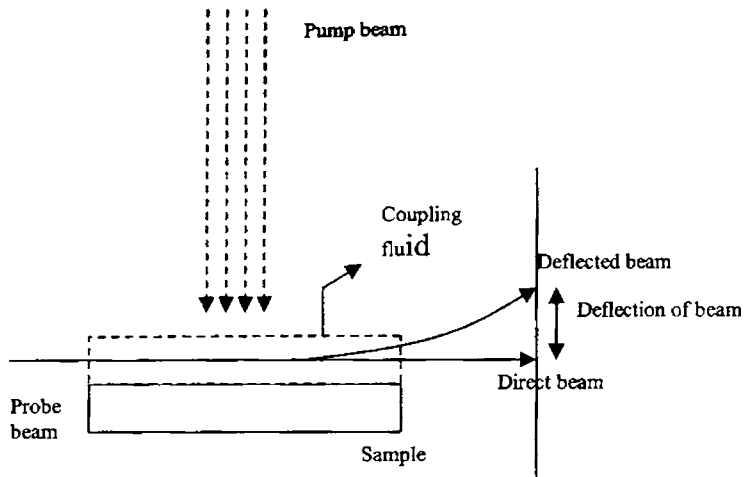


Fig.2.1: Experimental diagram of photothermal deflection

In this way signal averaging can be accomplished that averages out any other beam deflection due to index gradients that may be present but unrelated to the pump-beam absorption. From the variation of the PD signal with pump beam modulation frequency, the thermal diffusivity of the sample can be determined.

2.2.2 Photoacoustic Spectroscopy

The photoacoustic (PA) spectroscopy has evolved over the past three decades as a powerful method to study those materials that are unsuitable for study by conventional spectroscopic techniques [29-32]. This technique is based on the photoacoustic effect, originally detected by Alexander Graham Bell in 1880 [33, 34]. It possesses some unique features, mainly due to the fact that, even though the incident energy is in the form of photons, the interaction of these photons with the sample is studied not through the subsequent detection and analysis of some of the photons, but through a direct measurement of the energy absorbed by the material as a result of its interaction with the incident photon beam

The photoacoustic (PA) effect is the generation of an acoustic signal when the sample under investigation, placed inside an enclosed chamber, is irradiated by an intensity modulated beam of light. In case of gaseous or liquid samples, the sample fills the entire volume of the cell and acoustic signals are detected by a microphone or a piezoelectric transducer. In the case of solids, the sample fills only a portion of the cell and the remaining volume of the cell is filled with a non-absorbing gas like air. The PA signal is detected using a sensitive microphone suitably placed inside the cell. The absorption of the incident radiation excites the internal energy levels of the sample and upon subsequent deexcitation, all or part of the absorbed photon energy is converted into heat through non-radiative deexcitation processes. In the case of gas and liquid samples, which fill the entire volume of the sample chamber, this internal heating causes pressure fluctuations having the same frequency as that of the modulation frequency of the incident radiation and can be detected using an acoustic transducer kept in intimate contact with the sample. In the case of solid samples, which fill only a portion of the sample chamber, the periodic heating of the sample results in a periodic heat flow from the interior of the sample to the surrounding non-absorbing gas medium, which in turn produces pressure fluctuations in the gas and are detected as acoustic signal by a microphone suitably placed inside the chamber.

The Rosencwaig-Gersho (R-G) theory is a one-dimensional analysis of the production of photoacoustic signal in a simple cylindrical cell as shown in Fig. 2.2. The cell has a diameter D and length L . It is assumed that the length L is small compared to the wavelength of the generated acoustic signal λ , S , L and G represent backing material, sample, boundary layer of gas and gas medium respectively

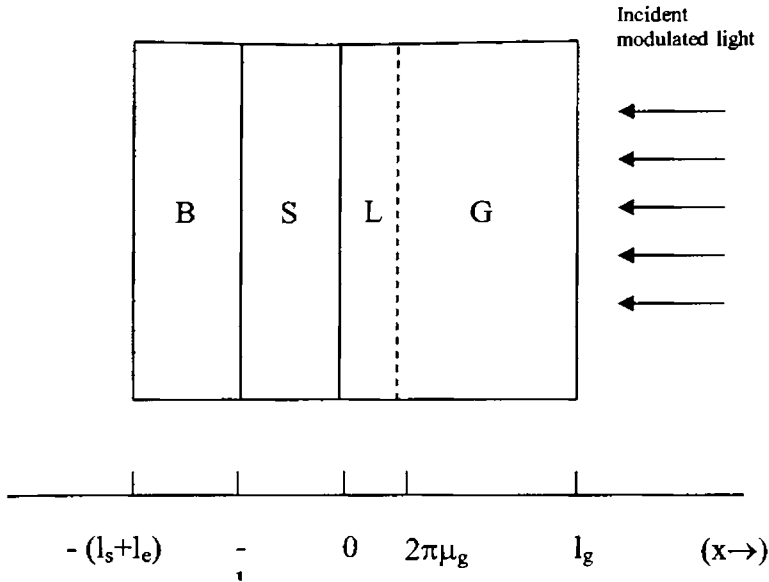


Fig. 2.2: Cross-sectional view of a simple cylindrical photoacoustic cell

A microphone (not shown in figure) detects the average pressure produced in the cell. The solid sample is considered to be in the form of a disc of diameter D and length l_s . The back surface is against a poor thermal conductor of thickness l_b . The length of the gas column in the cell is l_g . It is also assumed that, the gas and the backing material do not absorb light. Measurement of PA signal amplitude with wavelength of the incident radiation leads to determination of optical properties of the sample, and measurement of the PA signal amplitude/phase with modulation frequency enables one to determine thermal properties of the sample. Details of the experiment and results on different samples can be found in literature. Using photoacoustic method of investigation lots of studies are done to investigate

the thermal properties and optical energy gap in chalcogenide glasses [39-48]. Superconducting materials have got their own relevance in all time. Photoacoustic spectroscopy is used to study the thermal properties of superconducting materials like $\text{YBa}_2\text{Cu}_3\text{O}_7$ near transition temperature [49, 50]. The effect in thermal diffusivity by doping Pb in Bi-Sr-Ca-O superconductor is also studied using photoacoustic method [51]. Ferroelectric phase transition in crystals as well as ceramic samples can also studied photoacoustic spectroscopy [52, 53].

2.2.3 The Photopyroelectric Spectroscopy

The basic principle of the single beam PPE technique is that, when a periodically modulated light beam from a source impinges on the surface of a sample, the sample absorbs some of the incident energy. Thus the sample gets heated and due to the increased temperature it undergoes a non-radiative de-excitation process. This periodic temperature variation in the sample can be directly detected with a sensitive pyroelectric transducer, which is kept in intimate contact with the sample. The transducer is made of a thin film pyroelectric material. The PPE signal from the pyro electric transducer is due to a temperature dependent change in the polarization of the pyroelectric material. A one-dimensional geometry as shown in Fig. 2.3 is assumed where g , s , d and b refer to the gas medium in front of the sample, the sample, the pyroelectric detector and the backing medium respectively.

The photopyroelectric effect is based on the use of a pyroelectric transducer to detect the temperature rise due to periodic heating of a sample by induced light. The temperature variations in the detector give rise to an electrical current, which is proportional to the rate of change of the average heat content, given by [3]

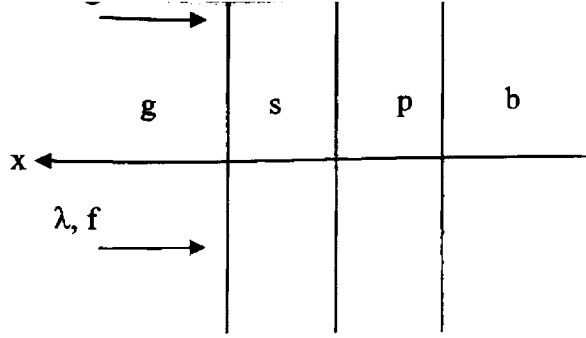


Fig. 2.3: One-dimensional geometry of the PPE set up

$$i_d = PA \left(\frac{\partial \theta(t)}{\partial t} \right) \quad (2.1)$$

where P is the pyroelectric coefficient of the detector, A is the detector area and

$$\theta(t) = \left(\frac{1}{L_d} \right) \int_0^{L_d} \theta(x,t) dx \quad (2.2)$$

is the spatially averaged temperature variation over the detector thickness, L_d .

Now, bearing in mind the fact that the observed signal output is affected by the impedance of the detector and subsequent detection electronics, we consider an equivalent circuit shown in Fig. 2.4. Here the pyroelectric detector is described as an ideal current source with a parallel leakage resistance R_d and a capacitance C_d supported on a backing having an equivalent parallel load resistance R_b and capacitance C_b , while the detection electronics is represented by an input capacitance C_e and a parallel load resistance R_e . The resistance and capacitance values of the detection

electronics get altered depending on the resistance and capacitance values of the backing.

For an optically opaque sample and pyroelectric detector, the complex amplitude of the output signal in frequency domain is given by [8]

$$V(f) = \left(\frac{j2\pi f PRA\theta(f)}{(1 + j f / f_c)} \right) \exp(j2\pi f t) \quad (2.3)$$

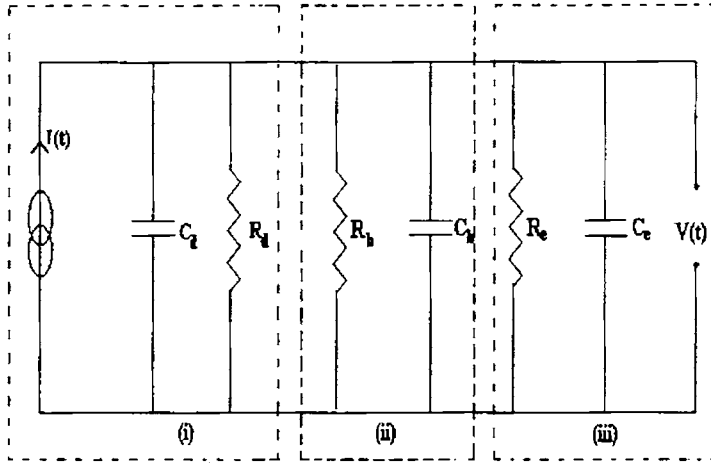


Fig. 2.4: Equivalent circuit for the photopyroelectric set up

where $f_c = \frac{1}{2\pi RC}$, with $\frac{1}{R} = \left(\frac{1}{R_d} + \frac{1}{R_b} + \frac{1}{R_e} \right)$ and $C = (C_d + C_e + C_b)$

and f is the modulation frequency.

The function $\theta(f)$ is given by [37]

$$\theta(f) = \frac{I_0 \beta_s \eta_s (b_{sg} \gamma_s + 1) \left[\exp\left((1+j)\sqrt{\frac{f}{f_{cd}}}\right) - 1 \right] (b_{bd} + 1) - \left[1 - \exp\left(- (1+j)\sqrt{\frac{f}{f_{cd}}}\right) \right] (b_{bd} - 1)}{(1+j) \left(\sqrt{\frac{f}{f_{cd}}} \right) K_s \left(\beta_s^2 - \frac{2jf}{L_s^2 f_{cs}} \right) X} \quad (2.4)$$

where

$$X = (b_{sg} + 1) \left\{ (b_{bd} + 1)(b_{ds} + 1) e^{(1+j)\sqrt{\frac{f}{f_{cd}}}} + (b_{bd} - 1)(b_{ds} - 1) e^{-(1+j)\sqrt{\frac{f}{f_{cd}}}} \right\} e^{(1+j)\sqrt{\frac{f}{f_{cs}}}} + (b_{sg} - 1) \left\{ (b_{bd} + 1)(b_{ds} - 1) e^{(1+j)\sqrt{\frac{f}{f_{cd}}}} + (b_{bd} - 1)(b_{ds} + 1) e^{-(1+j)\sqrt{\frac{f}{f_{cd}}}} \right\} e^{-(1+j)\sqrt{\frac{f}{f_{cs}}}} \quad (2.5)$$

The subscripts refer to the respective media indicated in Fig. 2.3. In general, we define the various parameters in Eq. (2.4) as

$$\mu_i = \sqrt{\frac{\alpha_i}{\pi f}} = \text{the thermal diffusion length of the respective media}$$

with

$$(i = s, d, b \text{ or } g);$$

$$\gamma_s = \left(\frac{\beta_s L_s}{(1+j)} \right) \sqrt{\frac{f_{cs}}{f}}$$

$$f_{ci} = \frac{\alpha_i}{\pi L_i^2} = \text{critical frequency at which the respective medium}$$

goes from a thermally thin to a thermally thick regime,

$$L_i = \text{thickness of the respective medium}$$

$$b_{ij} = \frac{e_i}{e_j} = \text{ratio of thermal effusivities of the media } i \text{ and } j$$

$$\beta_i = \frac{1}{\mu_{\beta i}} = \text{optical absorption coefficient, } \mu_{\beta i} \text{ being the optical}$$

absorption length of the respective medium.

η_s = fraction of absorbed radiation converted to heat (nonradiative quantum efficiency of the sample) and is assumed to be 1.

For a thermally thick sample, with $\mu_s < L_s$, and thermally thick pyroelectric, with $\mu_d < L_d$, the expressions for the PPE amplitude and phase give expressions for the values of the thermal diffusivity and effusivity, which allow a simultaneous determination of thermal conductivity and heat capacity, if the sample density ρ_s is known.

The expressions for the temperature dependent PPE amplitude and phase under the above conditions are obtained, after algebraic simplification, as

$$V(f, T) = \left(\frac{I_0 \eta_s A R_d}{L_d \sqrt{1 + (f/f_c)^2}} \right) \left(\frac{P(T)}{\rho_d(T) c_{pd}(T)} \right) \frac{\exp \left(- \left\{ \frac{\pi f}{\alpha_s} \right\} L_s \right)}{\left(\frac{e_s(T)}{e_d(T)} + 1 \right)}$$

(2.6a)

$$\phi(f, T) = - \tan^{-1} \left(\frac{f}{f_c} \right) - \left(\sqrt{\frac{\pi f}{\alpha_s(T)}} \right) L_s$$

(2.6b)

where T is the temperature and c_{pd} and ρ_d are the heat capacity (at constant pressure) and density of the PPE detector respectively.

From these two expressions, it is clear that the sample thermal diffusivity α_s can be calculated from the phase of the PPE signal, which

when substituted in the expression for PPE amplitude gives the thermal effusivity of the sample. From these the thermal conductivity and heat capacity of the sample can be calculated from the following relations

$$K_s(T) = e_s(T) \sqrt{\alpha_s(T)} \quad (2.7a)$$

$$c_{ps}(T) = \frac{e_s(T)}{\rho_s(T) \sqrt{\alpha_s(T)}} \quad (2.7b)$$

Since all the parameters in equations (2.6a) and (2.6b) are temperature dependent, a temperature calibration of the PPE detector is necessary here. All the thermal parameters can be calculated as a function of the sample temperature, provided the temperature dependence of the pyroelectric detector parameters are known.

2.3 EXPERIMENTAL TECHNIQUES ADOPTED IN THE WORK

We have used a variety of experimental techniques to study thermal and related properties of different samples. The experimental methods that we used are discussed in the following paragraphs.

2.3.1 Photopyroelectric method

This technique is used to study the thermal transport properties of different materials. We have measured the thermal properties of a few ceramic samples using the PPE technique. The variation of the thermal properties of a few crystalline samples that undergo different types of phase transitions with temperature have been studied and reported. The variation of the thermal properties with temperature and magnetic field for a sample that exhibits giant magneto-resistance has also been studied and reported. Details of these experimental methods

are described in the respective chapters. General technical details of the PPE experimental technique are given in section 2.4 of this chapter. The low temperature PPE setup and the magnetic field PPE measurement setup are described in sections 2.5 and 2.6 respectively.

2.3.2 Thermal Analysis- TG/DTA and DSC

Thermal analysis (TA) refers to a group of techniques in which some physical property of the sample is continuously measured as a function of temperature, while the sample is subjected to a controlled / programmed heating / cooling rate. TA is extensively used for fundamental studies as well as for quality control. Thermogravimetry (TG) is a technique in which the mass / weight of a sample is measured as a function of temperature, while the sample is subjected to a controlled heating programme. There may be a weight loss (e.g. decomposition) or a weight gain (e.g. oxidation). DTG is a technique in which the rate of weight change is measured as a function of temperature or time. Some thermal decomposition is complicated; more than one reaction may be occurring over a given temperature range. These overlapping reactions can be more clearly discernible from DTG than from TG curves. We have used a Perkin – Elmer Model Diamond TG/DTA instrument for all measurements reported in this thesis.

Differential Scanning Calorimetry (DSC) is a dynamic thermal analysis technique, with which the thermal response of any sample can be studied over a wide temperature range, under non-isothermal conditions. Whenever a material undergoes a change in its physical state such as melting or transition from one crystalline form to another or whenever it reacts chemically, heat is either absorbed or liberated. Many such processes can be initiated simply by raising the temperature of the material. In DSC, the enthalpies of these processes are determined by measuring the differential

heat flow required to maintain a sample material and an inert reference sample at the same temperature. This temperature is usually programmed to scan over a temperature range by increasing linearly at a predetermined rate. Thermal changes in a sample are due to exothermic or endothermic enthalpic transitions or reactions. Phase changes, fusion, crystalline inversions, boiling, sublimation, vapourisation, oxidation, reduction or other chemical reactions can cause such enthalpic changes. Generally, phase transitions, dehydration, reduction, and some decomposition reactions are exothermic. The relative advantages of the DSC over conventional calorimetric technique are

- (i) rapidity in the determination of thermal properties over a wide temperature range
- (ii) small amounts of sample required for measurements
- (iii) easy data analysis procedure and
- (iv) ability to study many different types of reactions.

The main disadvantages of this technique are relatively low accuracy and precision (5-10% accuracy), inability to conveniently determine the ΔH of overlapping reactions and inaccuracy in the determination of peak areas due to baseline changes during the transition or reaction.

We have used a Mettler Toledo model DSC-822 Differential Scanning Calorimeter to study the heats of transition and specific heat of different samples investigated in this work. The temperature range of this instrument is - 150 ° C to maximum 700 °C and the temperature accuracy is $\pm 0.2^\circ\text{C}$. This instrument permits direct calorimetric measurement, characterization, and analysis of thermal properties of materials. Under the control of the computer, this is programmed from an initial to a final temperature through transitions in the sample material (such as glass transition, melting, crystallization etc.).

2.3.3 Fourier Transform Infrared Spectroscopy

Fourier transform Infrared (FTIR) spectroscopy is a measurement technique for collecting infrared spectra. Instead of recording the amount of energy absorbed when the frequency of the infra-red light is varied (monochromator), the IR radiation is guided through an interferometer. After passing through the sample the detected signal is the interferogram signal. Performing mathematical Fourier Transform on this signal results in a spectrum identical to that from conventional (dispersive) infrared spectroscopy.

FTIR spectrometers are cheaper than conventional IR spectrometers because building interferometers is easier than the fabrication of a monochromator. In addition, measurement with a single spectrum is faster for the FTIR technique because the information of all frequencies is collected simultaneously. This allows multiple samples to be collected and averaged together resulting in an improvement in sensitivity. Because of its various advantages, virtually all modern infrared spectrometers are FTIR variety instruments.

We have used a Thermo Nicolet Avatar 370 FTIR instrument for part of the work presented in this thesis. The spectral range of this instrument is 7000 to 400 cm^{-1} . Its resolution is 0.9 cm^{-1} in the mid-IR range

2.3.4 X-Ray Powder Diffraction

Powder XRD (X-ray Diffraction) is perhaps the most widely used X-ray diffraction technique for structural characterization of materials. As the name suggests, the sample is usually in a powder form, consisting of fine grains of single crystalline material to be studied. The technique is also used widely for studying particles in liquid suspensions or polycrystalline solids (bulk or thin film materials).

The term 'powder' really means that the crystalline domains are randomly oriented in the sample. Therefore when the 2-D diffraction pattern is recorded, it shows concentric rings of scattering peaks corresponding to the various d spacing in the crystal lattice. The positions and the intensities of the peaks are used for identifying the underlying structure (or phase) of the material. For example, the diffraction lines of graphite would be different from diamond even though they both are made of carbon atoms. This phase identification is important because the material properties are highly dependent on structure. Powder diffraction data can be collected using either transmission or reflection geometry. Because the particles in the powder sample are randomly oriented, these two methods will yield the same data.

We have used a Bruker Model AXS D8 Advance Powder X- Ray Diffractometer with angle range $5-360^\circ$. The X –ray source used is Copper with wavelength 1.5406 Å. The detector used in this instrument is Si (Li) PSD.

2.4 THE PHOTOPYROELECTRIC SPECTROMETER

In this section, the experimental set up for the photopyroelectric technique is described. The application of this technique for the determination of thermal diffusivity (α), thermal effusivity (e), thermal conductivity (k) and heat capacity (c_p) are outlined in detail.

A basic PPE spectrometer consists of a radiation source of sufficient intensity, a light intensity modulator, PPE cell in which the sample is placed with the PPE detector and a signal-processing unit. The basic instrumentation has been modified by different workers depending on their application areas. Details of various modulus in a PPE spectrometer, including those of our set up are outlined below.

2.4.1 Radiation Source

The important parameters for the selection of the light source are the available power per usable bandwidth, the wavelength range, tunability and the ease of intensity modulation. Both coherent and incoherent sources are widely used. Arc lamps and lasers are the popular types of light sources currently used in PPE experiments. Continuous tunability from infrared to ultraviolet can be provided by suitable lamp-monochromator combination. High-pressure Xe arc lamps, high-pressure Hg lamps, tungsten lamps etc. are the commonly used incandescent sources. The relatively low bandwidth-throughput product is the major drawback of these sources. Since the strength of the PPE signal is found to be proportional to the intensity of radiation, optical sources should have high spectral radiance. The high peak power available from pulsed lasers is especially attractive for measuring very weak absorption, but the limited tunability is the main drawback of laser sources in PPE experiments.

In most of our experiments we have used a 120 mW He-Cd laser of wavelength $\lambda = 442$ nm, as the optical heating source.

2.4.2 Modulation

For the generation of PPE signal, modulation of the incident light beam is essential. Either amplitude or frequency of the incident beam can be modulated. Amplitude modulation is the most commonly used one because it can be accomplished by relatively inexpensive mechanical chopping methods. The depth of modulation using a mechanical chopper is nearly 100 %. As we know, the major disadvantage of PPE spectroscopy is its susceptibility to synchronous acoustic noise [38]. So care should be taken to minimize the vibration noise, which may interfere with the PPE signal and can't be filtered away even by lock-in detection. So

isolation of the mechanical chopping system from the optical table that supports the rest of the instrumentation needs to be done.

We have used a mechanical chopper (Stanford Research Systems Model No. SR 540) for the intensity modulation of the laser beam, in our experiments. The experiments have been set up on a vibration free table to reduce noise pick up.

2.4.3 PPE Detector

The heart of the PPE spectrometer is the PPE detector with which the temperature variations arising in the sample due to optical irradiation (and absorption) can be detected with high accuracy. The necessary condition for the choice of transducers to detect the thermal waves generated in the sample is that it should be a pyroelectric material. Pyroelectricity is essentially the manifestation of spontaneous polarization dependence on temperature in certain non-centrosymmetric anisotropic solids. If there is a small change of temperature, the pyroelectric material becomes electrically polarized and a voltage arises between specified directions in the material (detector). On placing a sample on the top of the pyroelectric (PE) detector, the average temperature change in the detector is approximately equal to the temperature changes at the interface between the sample and the detector. It is then evident that the time response of the detector is related to the time of the heat diffusion across the sample and in addition, the time required for reaching thermal equilibrium within the detector after thermal deexcitation. So one can obtain short time resolution by decreasing the thicknesses of the sample and the detector [3]; so the type of PE measurements that one wants to perform determine the thickness of the pyroelectric detector. Polyvinylidene difluoride (PVDF) and Lithium tantalate (LiTaO_3) are the most commonly used detectors. If short time responses are not needed, a thicker PE sensor

can be used in order to have stronger signals as well as better signal-noise ratio.

A 28 μm thick PVDF film with pyroelectric coefficient $P = 0.25 \times 10^{-8} \text{ V/cm-K}$ at room temperature has been used as the pyroelectric detector in our measurements. The room temperature values of pyroelectric detector resistance and capacitance are 50 $\text{G}\Omega$ and 750 pF respectively [35].

2.4.4 Signal Processing

The generated PE signal can be monitored directly with the appropriate electronic circuitry. In practical detection electronics the observed signal is, however, affected by the impedance of the sensor and electronics. In order to maximize the signal to noise ratio, the signal from the detector should be processed by an amplifier tuned to the chopping frequency. Generally, a phase sensitive lock-in detection is used for this purpose. Also by lock-in detection, the amplitude and phase of the PE signal can be measured and by using a dual phase lock-in amplifier, the measurements can be more easily when both amplitude and phase vary simultaneously.

We have used a dual phase lock-in amplifier (Stanford Research Systems, Model SR 830) in all our measurements.

2.4.5 The Complete PPE Spectrometer

A photopyroelectric cell which can be used over a wide range of temperatures has been designed and fabricated with which measurements can be made from 80 K to 350 K. A schematic diagram of the sample geometry is shown in Fig. 2.5. The sample cell is having a copper base, which forms the backing for the PPE detector. The sample to be measured is kept on the detector over which a very thin layer of carbon black is coated to improve the absorption.

A photopyroelectric set up of the type shown in Fig.2 6 has been used in the present work. The sample is attached to the pyroelectric detector by means of a thermally thin layer of a heat sink compound whose contribution to the signal is negligible. The pyroelectric detector attached to the sample is placed on a thermally thick backing medium (copper) which satisfies the boundary condition $b_{bd} > 1$. The frequency of modulation of the light beam is kept above 30 Hz to ensure that the PVDF film, the sample and the backing medium are all thermally thick during measurements. The signal output is measured with a lock-in amplifier having $10\text{M}\Omega$ input resistance and 50pF input capacitance. Since the backing material is copper instead of air or vacuum, the equivalent resistance and capacitance may be as high as $100\text{M}\Omega$ and 800pF respectively. So the equivalent resistance is reduced to $10\text{M}\Omega$ by using an additional parallel resistance to shift the value of f_c to the required range as per the assumptions made in the theory.

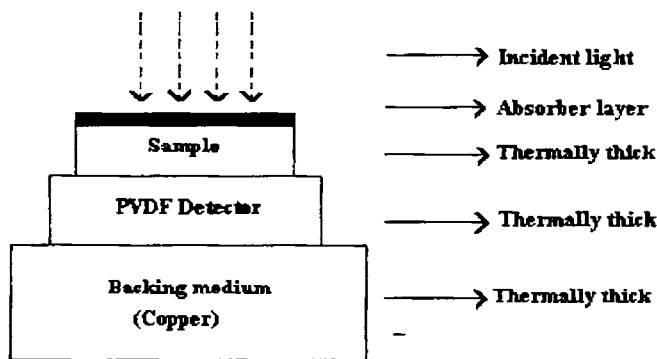


Fig. 2.5: The sample configuration for the PPE setup

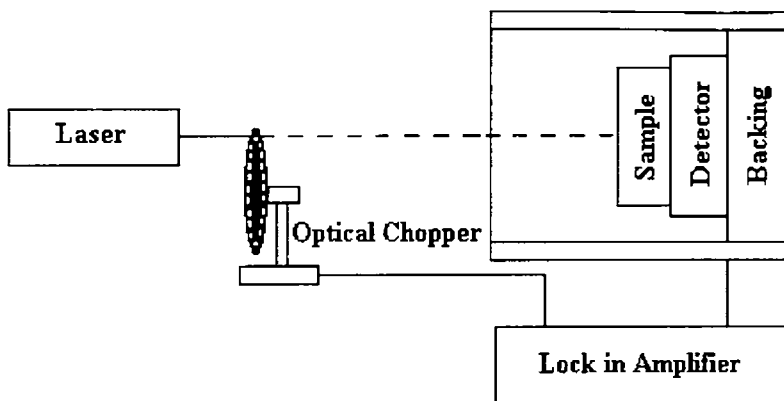


Fig 2.6: Experimental set up for photopyroelectric measurements

2.5 LOW TEMPERATURE PPE MEASUREMENT SETUP

A schematic diagram of the PPE sample cell used for low temperature PPE measurements is shown in Fig. 2.7. The cell consists of a cavity of length about 43cm and diameter about 33cm in which a sample holder is kept. The cavity has got a glass window to pass the laser beam. The sample holder which is made up of a copper block is of about diameter 4cm. The PVDF film which is the sensor is fixed on the sample holder using silver paste. The diameter of the film which is used in the measurement is about 9mm which is important in the calculation. From the back side of the copper block a wire is taken which will serve as the connection from the back side of the film. Then a copper ring kept inside a Teflon ring is kept on the top of the film and tightened it using four screws. From the copper ring a connection is taken which serves as the front connection of the film. Both these wires are given to a BNC connector which is connected to the lock-in amplifier using a coaxial cable. The sample holder is connected to a cold finger which is

connected to the liquid nitrogen chamber. By passing liquid nitrogen into the chamber we can lower the temperature to about 80K. A heater which is attached to the sample holder can be used to increase the temperature. The temperature can be controlled by using a PID temperature controller. All the measurements are done only after evacuating the outer chamber.

The photopyroelectric setup used for measurements with this low temperature cell is the same as the shown in Fig.2.6 with the room temperature sample cell replaced by the low temperature cell.

2.6 PPE MEASUREMENTS WITH MAGNETIC FIELD

We have carried out measurements of the variations of thermal properties of some samples showing GMR properties with applied external magnetic field as well as temperature using the PPE technique. An experimental setup has been designed and fabricated for these measurements. The details of this setup and measurement technique are described below.

2.6.1 Magnetic field Measurement Setup

A PPE setup to measure variations in thermal properties of a sample with applied external magnetic field has been designed and fabricated. This has been configured by modifying the room temperature sample holder. A schematic diagram of this setup is shown in Fig.2.8. The sample cell is kept between the pole pieces of an electromagnet. The distance between the pole pieces is adjusted in such a way that one should get maximum field at the place where the sample is kept. The field can be varied by varying the current through the field coil. With a magnet used in the present setup the field could be varied from 0 to 2T. Using the digital Gauss meter (NISCO model DGM-20) we can measure the field strength for any current and distances between pole pieces. The sample configuration in the new setup is shown in Fig 2.9

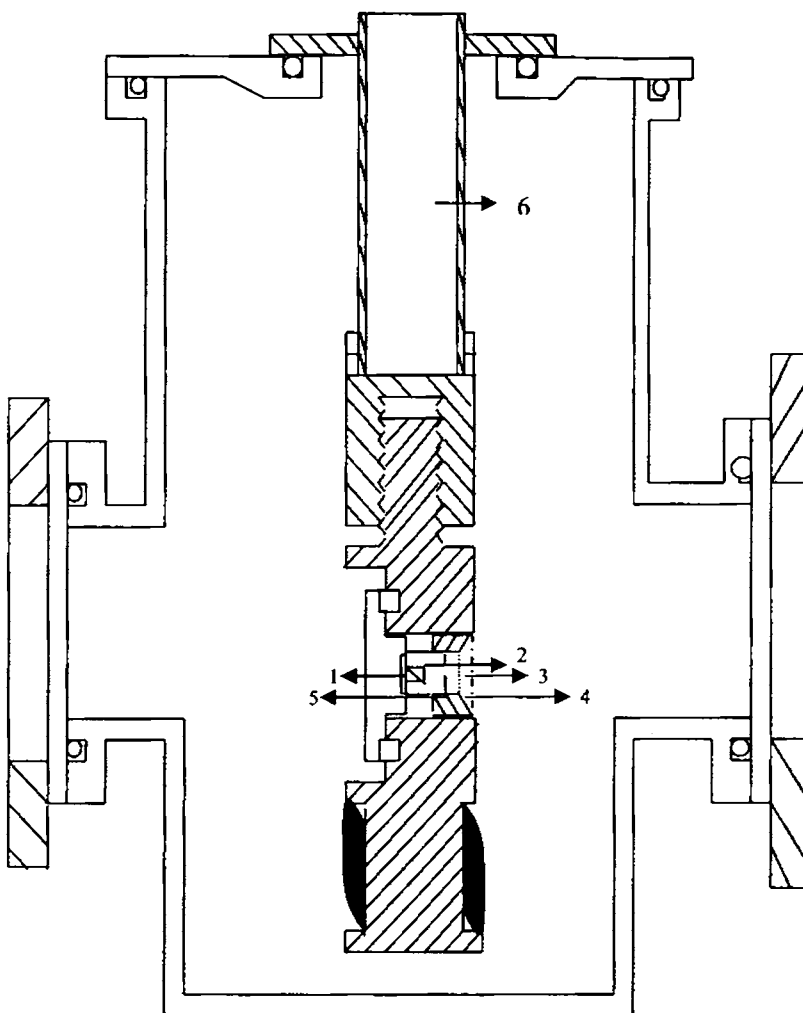


Fig. 2.7: Schematic diagram of the PPE cell

1. PVDF detector 2. Sample 3. Glass window 4. Copper ring 5. Teflon outer cover 6. Liquid nitrogen chamber

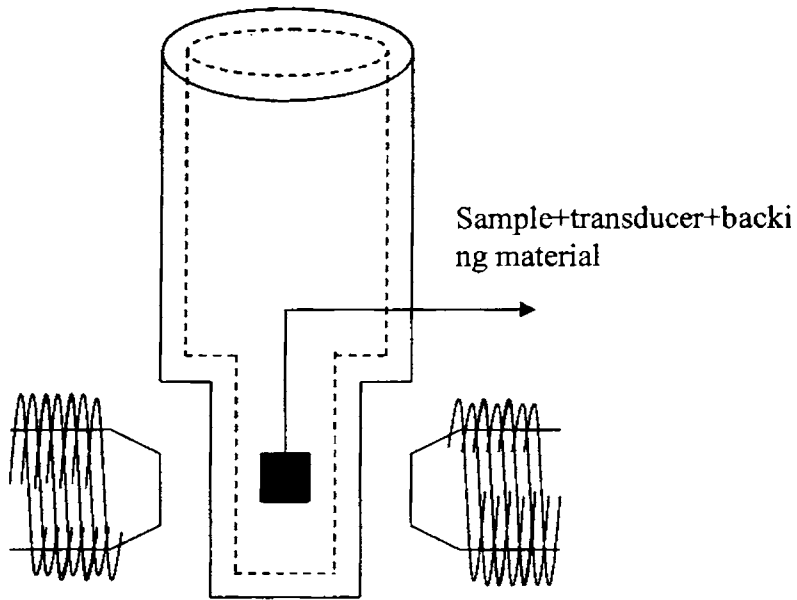


Fig.2.8: The magnetic field measurement set up

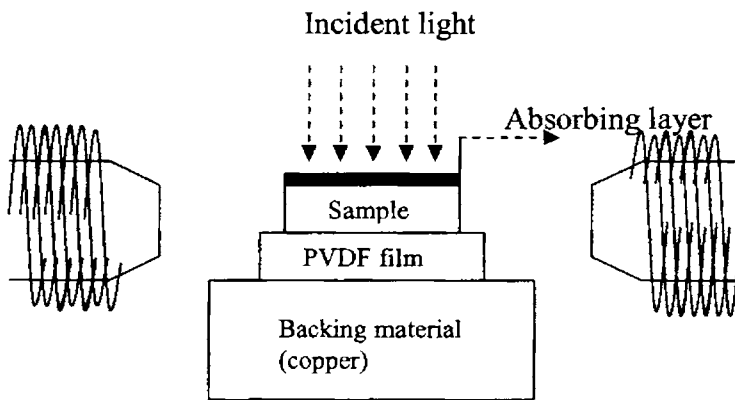


Fig. 2.9: The sample configuration for the magnetic field PPE setup

2.7 MEASUREMENT METHODOLOGY:

The samples are generally cut into size of about 5mm diameter and approximately 0.5mm thickness and optically polished. A very thin layer of carbon black is coated on the sample surface that faces the modulated beam of light to enhance the optical absorption. The sample is kept on the PVDF sensor using heat sink compound which is thermally conducting and electrically insulating. The modulated light beam from the laser source is allowed to fall on the sample. The thermal waves produced in the sample are transmitted to the pyroelectric sensor. Due to the temperature variations an ac voltage is induced into the film and this is measured using the lock-in amplifier. For low temperature measurements liquid nitrogen is poured into the cavity at correct intervals. The temperature is monitored and controlled using a PID temperature controller (Lakeshore cryotronics Model DRC 82C). The temperature can be kept constant using this temperature controller and we can measure the amplitude and phase from the lock in amplifier at any particular temperature. This measurement setup enables one to make PPE measurements by varying temperature and/or magnetic field strength. Measurements done on specific samples are described in the respective chapters of the thesis.

REFERENCES

1. A. Mandelis, *Chem. Phys. Lett.* **108**, 388(1984)
2. H. Coufal, *Appl. Phys. Lett.* **44**, 59 (1984)
3. H. Coufal and A. Mandelis, *Ferroelectrics* **118**, 379 (1991)
4. A. Mandelis, J. Vanniasinkam and S. Budhudu, *Phys. Rev. B* **48**, 6808 (1993)
5. M. Chirtoc and G. Mihailescu, *Phys. Rev. B* **40**, 9606 (1989)
6. J. Shen and A. Mandelis, *Rev. Sci. Instrum.* **66**, 4999 (1995)
7. A. Mandelis and K. F. Leung, *J. Opt. Soc. Am. A* **8**, 186 (1991)
8. A. Mandelis and M. M. Zver, *J. Appl. Phys.* **57**, 4421 (1985)
9. J. Shen, A. Mandelis and H. Tsai, *Rev. Sci. Instrum.* **69**, 197 (1998)
10. H. Coufal and Z. Fresenius, *Anal. Chem.* **324**, 456 (1986)
11. H. Coufal, IEEE Trans. Ultrason. *Ferroelectric. Freq. Control* **UFFC-33** 507 (1986)
12. H. Coufal, *Appl. Phys. Lett.* **45**, 516 (1984)
13. H. Coufal, R. Grygier, D. Horne and J. Fromm, *J. Vac. Sci. Technol. A* **5**, 2875 (1987)
14. H. Coufal, J. Stöhr and K. Baberschke in *Photoacoustic and Photothermal Phenomena*, edited by P. Hess and J. Pelzl, (Springer, Heidelberg, 1988) p.25
15. T. Hinoue, S. Kawada, M. Murata and Y. Yokoyama, *Chem. Lett. Jpn.* 2061 (1988)
16. *Photoacoustic and Thermal Wave Phenomena in Semiconductors*, edited by A. Mandelis, (Elsevier, New York, 1987)
17. R. K. Grygier, W. Knoll and H. Coufal, *Can. J. Phys.* **64**, 1067 (1986)
18. T. J. Chuang, H. Coufal and F. Träger, *J. Vac. Sci. Technol. A* **1**, 236 (1983)

19. D. Dădârlat, M. Chirtoc, R. M. Căndea and I. Bratu, *Infrared Phys.* **24**, 469 (1984)
20. M. Chirtoc, D. Dădârlat, I. Chirtoc and D. Bicanic, *Spectrosc. Lett.* **21**, 413 (1988)
21. M. Chirtoc, D. Dădârlat, I. Chirtoc and D. Bicanic in *Photoacoustic and Photothermal Phenomena*, edited by P. Hess and J. Pelzl, (Springer, Heidelberg, 1988)
22. M. Chirtoc and I. Chirtoc, *Infrared Phys.* **29**, 847 (1989)
23. G. B. Kasting, C. W. Garland and K. J. Lushington, *J. Physique* **41**, 879 (1980)
24. T. Thoen, H. Marynissen and W. van Dael, *Phys. Rev. A* **26**, 2886 (1982)
25. M. Marinelli, F. Murtas, M. G. Mecozzi, U. Zammit, R. Pizzoferrato, F. Scudieri, S. Martellucci and M. Marinelli, *Appl. Phys. A* **51**, 387 (1990)
26. U. Zammit, M. Marinelli, R. Pizzoferrato, F. Scudieri and S. Martellucci, *J. Phys. E: Sci. Instrum.* **21**, 935 (1988)
27. C. Preethy Menon and J. Philip, *Meas. Sci. and Technol.* **11**, 1744 (2000)
28. Jeffery A.Sell, *Photo thermal investigations of solids and fluids*, Academic press,Inc.
29. A. Rosencwaig, *Opt. Commun.* **7**, 305 (1973)
30. A. Rosencwaig, *Anal. Chem.* **47**, 592A (1975)
31. A. Rosencwaig in *Advances in Electronics and Electron Physics*, Vol. 46, edited by L. Marton, (Academic Press, New York, 1978) pp. 207-311
32. A. Rosencwaig, *Photoacoustics and Photoacoustic Spectroscopy*, (Wiley, New York, 1980)
33. A. G. Bell, *Amer. J. Sci.* **20**, 305 (1880)

34. A. G. Bell, *Phil. Mag.* **11**, 510 (1881)
35. 1983 Kynar™ Piezo Film Technical Manuel (Penwalt Corp.) p.17
36. R. J. Collier, C. B. Burckhardt, and L. H. Lin, *Optical Holography* Academic Press, New York (1971)
37. G. Busse, in *Photoacoustic, Photothermal and Photochemical Processes at Surfaces and Thin Films* Hess, P., Editor, Springer-Verlag, New York (1989)
38. A. Rosencwaig and A. Gersho, *J. Appl. Phys.* **47**, 64 (1976)
39. K.N. Madhusoodanan and Jacob Philip, *Phys. Rev. B* **39**, 7922 (1989)
40. K.N. Madhusoodanan and Jacob Philip, *J. Non-Cryst. Solids* **109**, 255 (1989)
41. K.N. Madhusoodanan, K. Nandakumar, Jacob Philip, S.S.K. Titus, S. Asokan and E.S.R. Gopal, *Phys. Stat. Solidi. a* **114**, 525 (1989)
42. K.N. Madhusoodanan, R. Sreekumar and J Philip, *J. Acoust. Soc. India* **17**, 347 (1989)
43. Jacob Philip and K.N. Madhusoodanan, *Phys. Rev. B* **38**, 4127 (1988)
44. K.N. Madhusoodanan and Jacob Philip, *Phys. Status Solidi a* **108**, 775 (1988)
45. K.N. Madhusoodanan and Jacob Philip, *Pramana-J. Phys.* **33**, 705 (1989)
46. Sheenu Thomas and J. Philip, *J. of Phy. C: Cond. Matt.* **12**, 4767 (2000)
47. Sheenu Thomas and J. Philip, *Solid State Comm.* **107**, 423 (1998)
48. Sheenu Thomas and J. Philip, *Phys. Stat. Solidi (b)* **20**, 359 (1997)
49. Johny Isaac, Jacob Philip and B.K. Chaudhari, *Pramana - J. Phys.* **32**, L 167 (1989)
50. Johny Isaac, Jacob Philip and B.K. Choudhuri, *Pramana-J. Phys.* **31**, L153 (1989)

51. J. Isaac, J Philip, M. T. Sebastian and A. D. Damodaran, *Physica C: Superconductivity* **199**, 247 (1992)
52. Johney Isaac and J Philip, *Phys. Status. Solidi b* **165**, K47 (1991)
53. Johney Isaac and J Philip, *J. Appl.Phys.* **69**, 7765 (1991)

Chapter 3

Thermal transport properties of Di Calcium Lead Propionate

1. 1 INTRODUCTION

Dicalcium Lead Propionate (DLP, Chemical formula $\text{Ca}_2\text{Pb}(\text{C}_2\text{H}_5\text{COO})_6$), which belongs to the family of double propionates, is ferroelectric below 333K along the *c* axis [1]. It undergoes a para to ferro electric phase transition at 333K (T_{c1}), which is a second order phase transition. Upon decreasing the temperature further, it undergoes another phase transition at 191K (T_{c2}), which is first order. The transition at T_{c1} is associated with the movement of the ethyl group (C_2H_5) [2], but the one at T_{c2} is still not understood well. Even below this transition temperature the material continues to remain ferroelectric. Based on the measurement of the hydrostatic pressure dependence of the crystal structure of DLP above and below the respective phase transitions, Gesi and Ozawa [3] have proposed that the phases above and below T_{c2} are isomorphous to each other. However, on the basis of polarizing microscopic observations and dielectric constant measurements, Gesi has concluded that the two phases above and below T_{c2} are not isostructural [4]. The crystal structure of DLP is tetragonal at room temperature [5]. The space group associated with this is D^4_4 ($P4_32_12$). The lead atoms are located at $4a$ positions and calcium atoms at $8b$ positions. It is also interesting to note that the position of organic group has not yet been identified. Studies on the pyroelectric properties of DLP associated with its phase transitions by Osaka, Makita and Gesi have led to

the conclusion that DLP crystal between $T_{c1}=333\text{K}$ and $T_{c2}=191\text{K}$ is tetragonal and polar, the point group in phase being C_4 or C_{4v} [6].

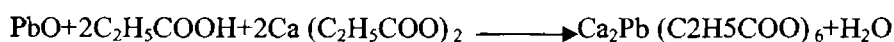
The Raman scattering, Infrared absorption and Dielectric properties of this crystal have been studied by earlier workers [7, 8]. Earlier, EPR studies on DLP, doped with Mn^{2+} , by Bhat *et.al* suggest that Mn^{2+} enters the plane of Ca^{2+} substitutionally, and are loosely held in the lattice sites of Ca^{2+} , as the ionic radius of Mn^{2+} (0.08nm) is small compared to Ca^{2+} (0.09nm) [9]. From the results on the temperature dependence of electrical conductivity and dielectric constant, Badarinath et al have concluded that the para to ferroelectric transition in Mn^{2+} doped DLP is a defect controlled property, and is dependent on the concentration of the dopant [10]. The phase diagram of the mixed crystal system DSP-DLP, where DSP stands for Dicalcium Strontium propionate, was determined by Nagae *et. al* from dielectric and dilatometric measurements [7]. They confirmed that the space groups of DLP are D_4^d (D_4^d) above T_{c1} and C_2^d (C_2^d) below this temperature. Work done by Standnicka *et.al*. showed how much more accurately the transition temperature could be established for DSP-DLP mixed crystal through high precision measurements of optical retardation [11]. Nage *et.al*. have reported Raman scattering spectra of DSP and DLP between 73 and 423K [7]. Since no soft modes were observed, they concluded that both the phase transitions of the two materials are of the order – disorder type implying that these transitions are most probably isomorphous [7]. Takashige *et al*. have reported the piezoelectric and elastic properties of ferroelectric DLP over a wide temperature region, including the ferroelectric-paraelectric phase transition point (T_{c1}) [8].

Even though the specific heat of DLP was reported way back in 1965 [1], other thermal properties such as thermal conductivity have not been reported so far. Moreover, systematic thermal analysis following

thermogravimetry or scanning calorimetry through T_{c1} and T_{c2} have not yet been reported. In this work we report thermo gravimetric and scanning calorimetric analysis of DLP through these transition temperatures. The FTIR spectrum at room temperature is also reported. The thermal transport properties of the sample, thermal diffusivity (α), effusivity (e), thermal conductivity (k) and specific heat capacity (c_p) of the sample have been measured as a function of temperature following an improved photopyroelectric (PPE) technique described in Chapter 2. The anisotropy in thermal diffusivity/conductivity along the principal axes as well as their variation through these transition temperatures have also been measured following the PPE technique. The experimental methods followed, results obtained and a discussion of the results are given in the following sections.

3.2 SAMPLE PREPARATION

DLP crystals were grown by slow evaporation method [12, 13]. The solution is prepared by gradually dissolving lead monoxide in an aqueous solution of propionic acid to which the calcium salt of propionic acid was added in the stoichiometric proportion. The chemical equation for this reaction is



The solution is filtered and recrystallised two to three times for clarity of the crystals. Then the solution is kept in a bath keeping the temperature about 35°C and good quality colorless transparent crystals of size about 1cm^3 is obtained in three to four weeks time. Morphology of the crystals is shown in Fig.3.1. Using the X-ray diffraction spectrometer the x-ray diffraction pattern has been recorded and is shown in Fig.3.2. So obtained crystals were cut with a slow speed diamond wheel saw such that they have faces perpendicular to the $[100]$, $[010]$, $[010]$ planes. The samples are carefully polished and made into a thickness of about 0.5mm for

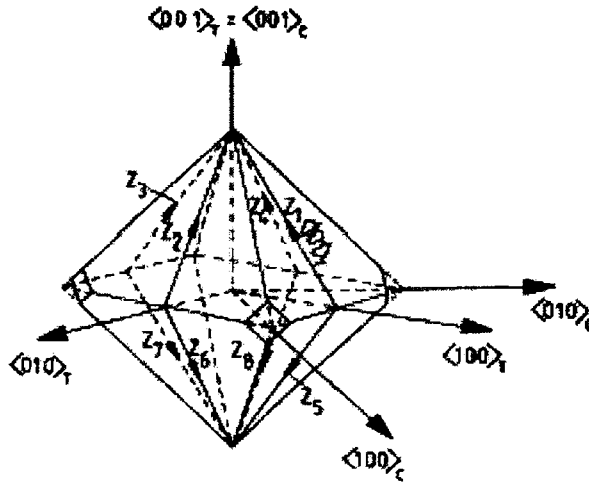


Fig.3.1: Morphology of the DLP crystals

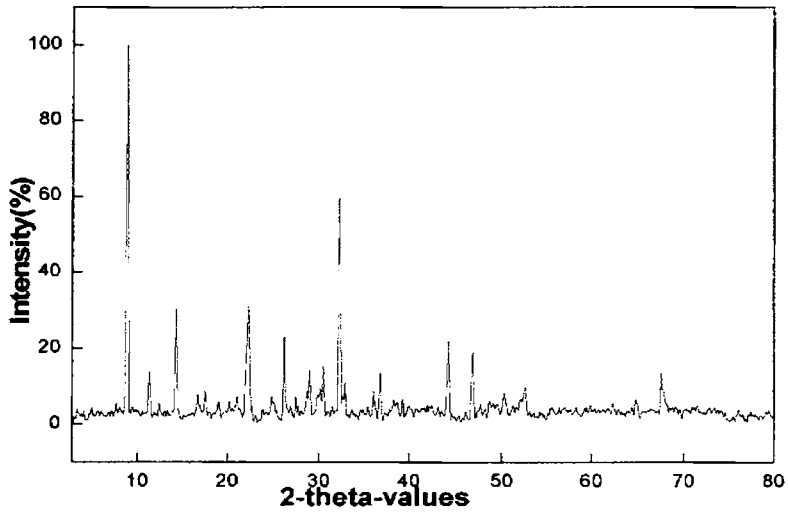


Fig.3.2: X-ray diffraction pattern of the crystal

photopyroelectric measurements. The density of the sample was measured to be $1.747 \pm 0.001 \text{ g/cm}^3$

3.3 EXPERIMENTAL METHOD

3.3.1 Photopyroelectric thermal wave measurements

The photopyroelectric method as has been described in chapter 2 has been used to determine the thermal properties of single crystals of DLP [14, 15]. For this measurement the sample dimensions should be such that the sample, the pyroelectric detector and the backing material should be thermally thick during the whole measurement. The sample is illuminated with an intensity-modulated beam of light, which gives rise to periodic temperature variation in the sample by optical absorption. The thermal waves so generated propagate through the sample and are detected with a pyroelectric detector. Modulation frequency is kept above 30Hz in all our experiments to ensure that the detector, the sample and the backing medium are all thermally thick during measurements. The thermal thickness of DLP sample has been verified by plotting the PPE amplitude and phase with frequency at room temperature. Since the optical absorption in DLP is low, a light coating of carbon black is provided on the face of the sample to enhance optical absorption and thermal wave generation. Block diagram of the experimental setup and other details are already given in chapter 2 of the thesis.

Measurement of the PPE signal phase and amplitude enables one to determine thermal diffusivity (α) and thermal effusivity (e) respectively. Principles of this method and experimental procedures are described in detail elsewhere [14]. From the measured values of α and e , the thermal conductivity k and specific heat capacity c_p of the samples are determined, knowing density ρ , using the following relations [14].

$$k = e [\alpha]^{1/2} \quad (1)$$

$$c_p = e/[\rho[\alpha]^{1/2}] \quad (2)$$

The calibration of the experimental set up has been done with known samples prior to carrying out the measurements.

The variations of the detected signal amplitude and phase using the lock in amplifier as a function of frequency for DLP sample at room temperature are shown in Fig.3.3 and Fig.3.4 for the three symmetry directions. In these measurements the sample has been cut and polished to such a thickness that the sample and the PVDF film detector are thermally thick at all the modulation frequencies used.

These measurements have been done at temperatures between 170 K and 360 K at temperature intervals of 2 K normally and at intervals of 1 K at temperatures in the vicinity of the two transition points. At each measurement temperature, the sample has been kept at constant temperature during measurements. The temperature variations of the PPE amplitude and phase along the a-, b-, c- axis of DLP are shown in Fig.3.5, Fig.3.6 and Fig.3.7 respectively. From the frequency dependence of the pyroelectric amplitudes and phases, the thermal diffusivity and effusivity of the sample along the above axes have been determined at each temperature. The temperature variations of these parameters along the a-, b- and c-axis of DLP are shown in Fig.3.8, Fig.3.9 and Fi.3.10 respectively. From the diffusivity and effusivity values, the corresponding values of thermal conductivity and specific heat capacity have been computed and plotted in Figures 3.11, 3.12 and 3.13 for all three axes.

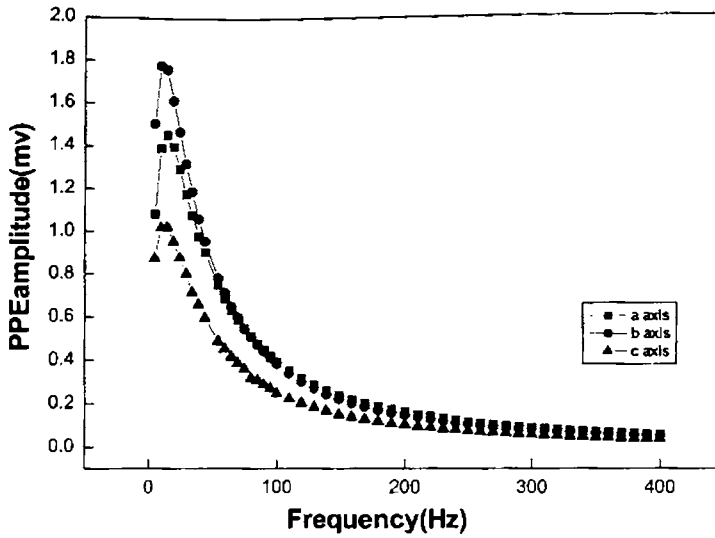


Fig.3.3: Variations of PPE amplitude with frequency at room temperature along the three axes

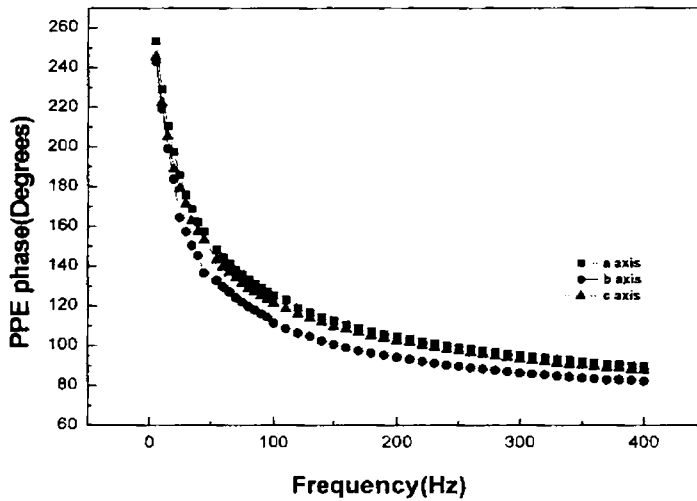


Fig.3.4: Variations of PPE Phase with frequency at room temperature along the three axes

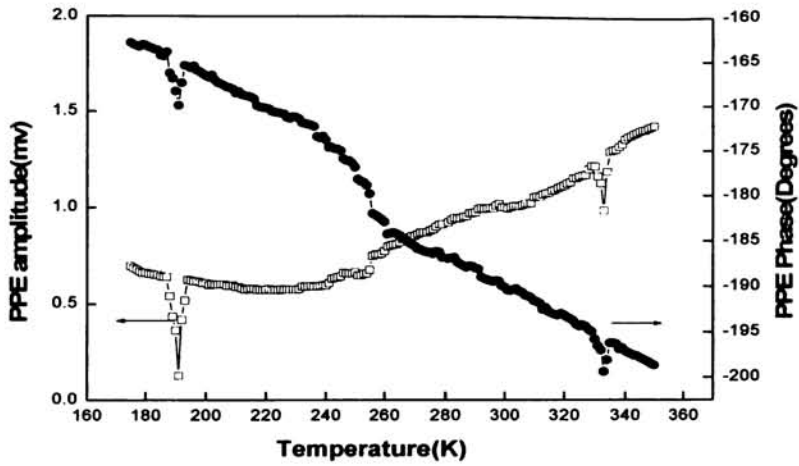


Fig.3.5: Variations of PPE amplitude and phase with temperature along a- axis

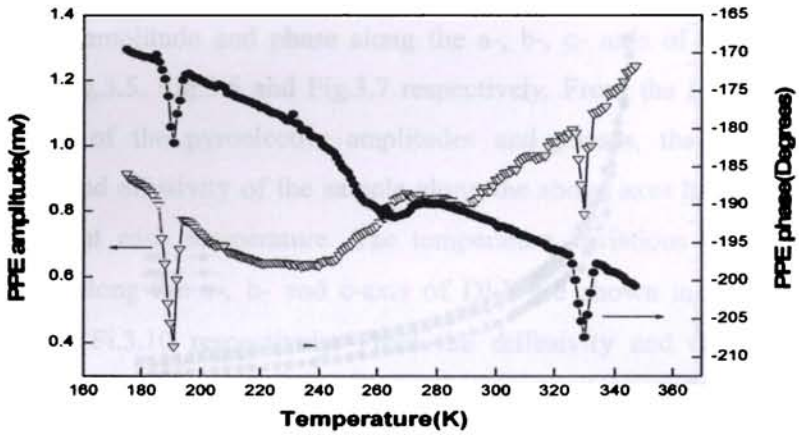


Fig.3.6: Variations of PPE amplitude and phase with temperature along b- axis

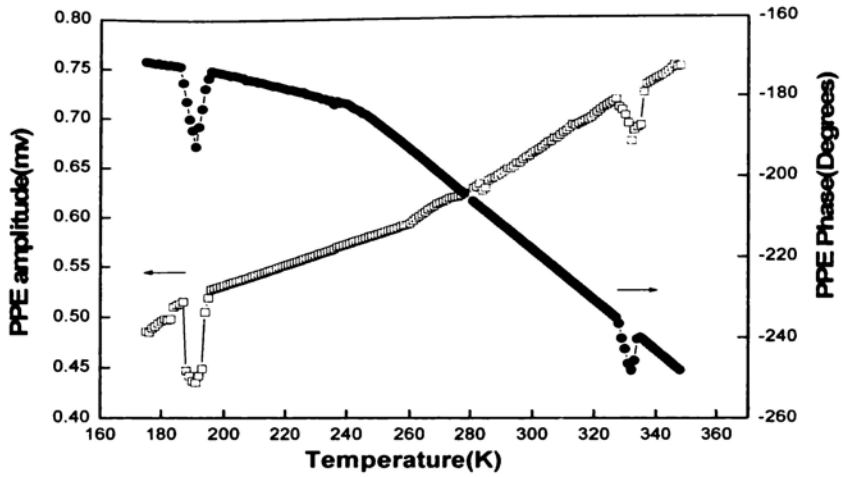


Fig.3.7: Variations of PPE amplitude and phase with temperature along c- axis

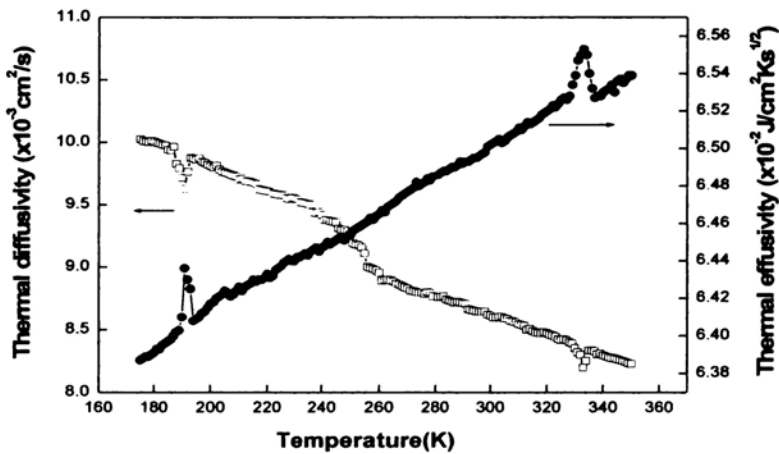


Fig.3.8: Variation of thermal diffusivity and thermal effusivity with temperature along a- axis

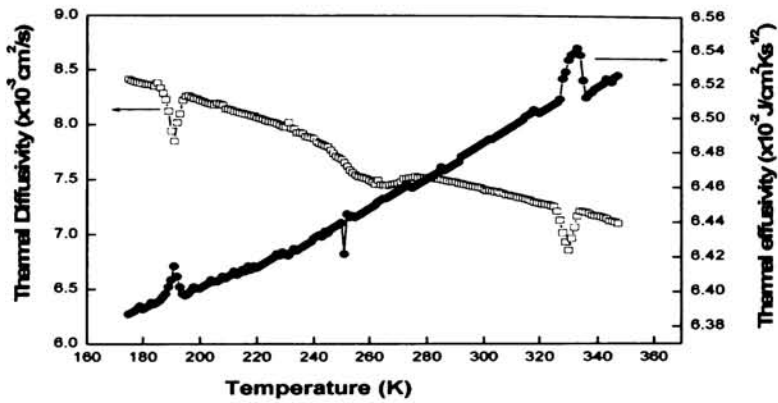


Fig.3.9: Variation of thermal diffusivity and thermal effusivity with temperature along b- axis

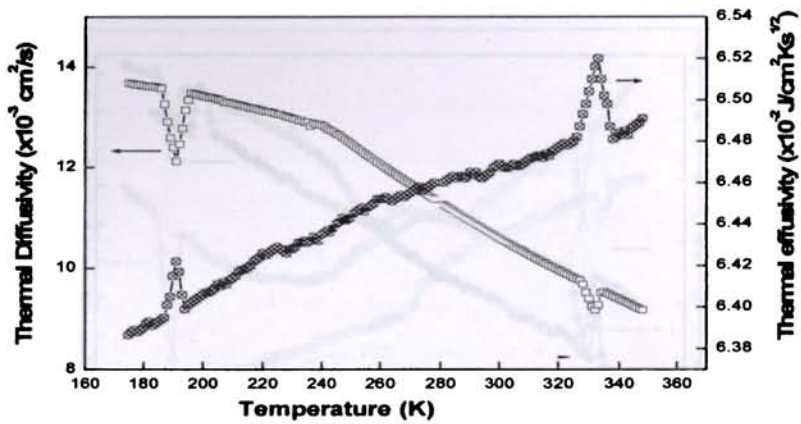


Fig.3.10: Variation of thermal diffusivity and thermal effusivity with temperature along c- axis

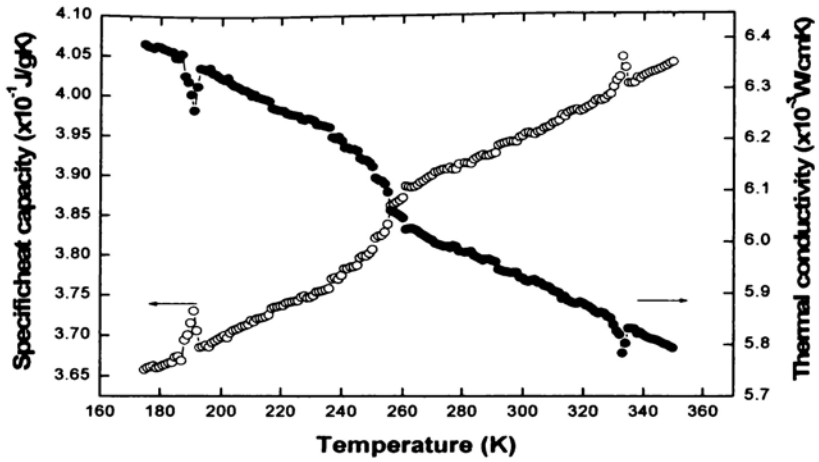


Fig.3.11: Variations of specific heat capacity and thermal conductivity with temperature along a- axis

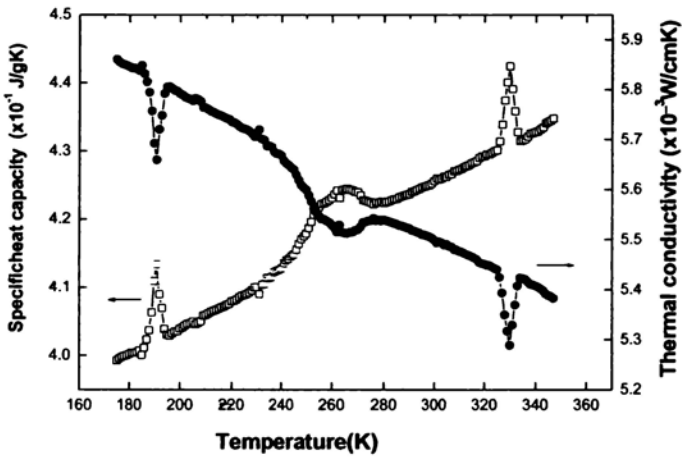


Fig.3.12: Variation of specific heat capacity and thermal conductivity with temperature along b- axis

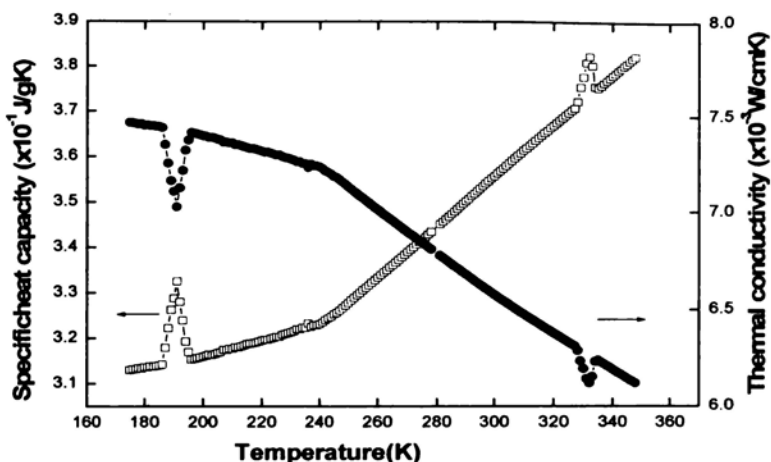


Fig.3.13: Variation of specific heat capacity and thermal conductivity with temperature along c- axis

3.3.2 Thermal analysis of DLP Crystals

The TG/DTA and DSC curves of DLP crystals have been recorded following the standard procedures. TG/DTA analysis has been carried out in nitrogen atmosphere. TG/DTA curves have been plotted in the temperature range 30° C to 1000° C at a heating rate of 10° C per minute. The TG/DTA curves for DLP crystals are shown in Fig. 3.14.

The DSC curve of DLP during heating cycle is shown in Fig.3.15. The transitions at 191K (-82° C) and 333K (60° C) can be clearly seen in the DSC plot. Fig. 3.16 shows the DSC plots recorded during heating and cooling cycles. The thermal hysteresis of the sample during the heating and cooling cycles around the transition at 191K (-82° C) is evident from this figure.

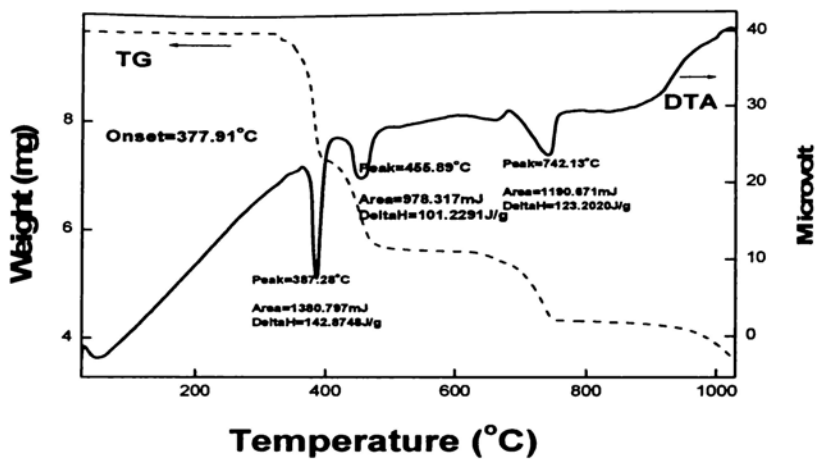


Fig.3.14: TG and DTA curves of the DLP sample

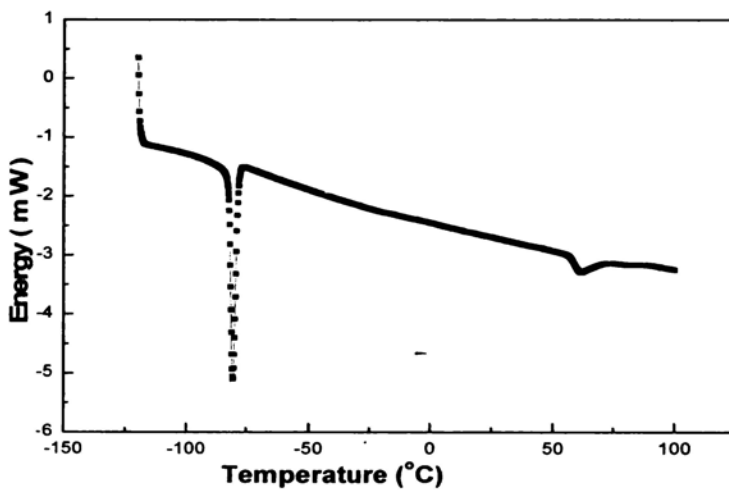


Fig.3.15: DSC plot of DiCalcium Lead Propionate during heating.

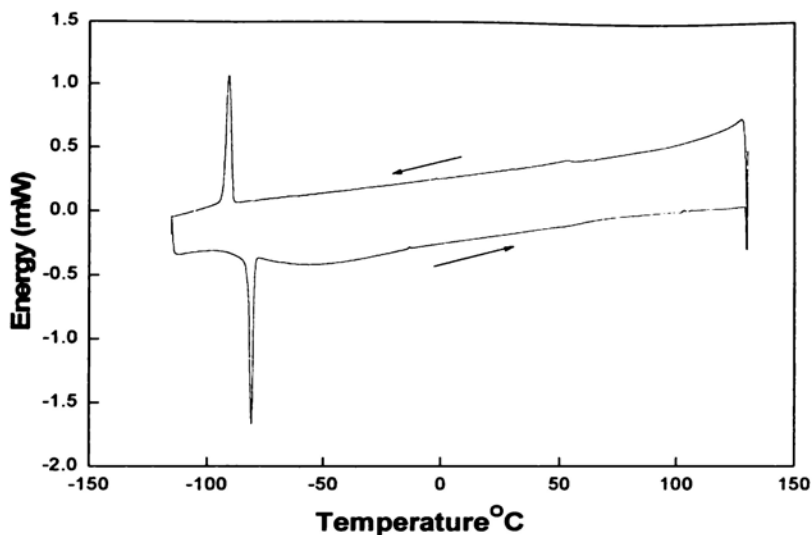


Fig.3.16: DSC curves of DLP during heating and cooling cycles

3.3.3 FT-IR Spectrum

The infrared absorption spectrum in the mid-IR range have been recorded. The FTIR spectrum of DLP in the wavenumber range $4000\text{--}400\text{cm}^{-1}$ is given in Fig.3.17. The wave numbers corresponding to the absorption peaks are indicated in the figure.

3.4 RESULTS AND DISCUSSION

3.4.1 Thermal conductivity During Phase Transitions

We have presented a comprehensive set of results on the thermal transport and other relevant properties of DLP crystal. The variation of thermal diffusivity (α), effusivity (e), thermal conductivity (k) and specific heat capacity (c_p) of DLP, shown in figures 3.8, 3.9, 3.10, 3.11, 3.12 and 3.13 clearly indicate that the above thermal properties undergo anomalous

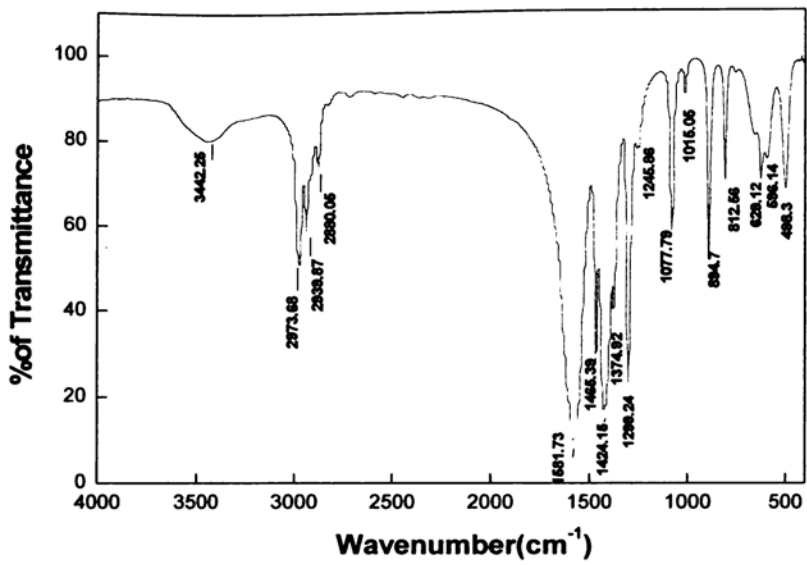


Fig.3.17: FTIR spectrum of Di Calcium Lead Propionate.

variations during the phase transitions at 191K conductivity show anomalous decreases during transitions, whereas the heat capacity shows a corresponding anomalous increase. Being an electrical insulator crystal, the major contribution to the heat capacity of DLP is expected from the lattice phonons and the electronic contribution to heat capacity is very small. As the phonon modes undergo variations due to mode instability at the transition points, they absorb excess energy giving rise to enhancement in heat capacity. This is getting reflected in the DSC curve as well. Again, during the transitions, the phonon mean-free path increases, resulting in a decrease in thermal resistance or a corresponding increase in thermal diffusivity and thermal conductivity. The thermal properties of DLP crystal along the three symmetry axes are tabulated in Table 3.1. As is evident from this table, the anisotropy in thermal conductivity is not very high for this crystal. The

maximum thermal conduction occurs along the c-axis which is the direction of spontaneous polarization for this crystal.

Table 3.1 Thermal conductivity of DLP along the three principal axes, in units of $\times 10^{-2} \text{Wcm}^{-1}\text{K}^{-1}$

Temperature K	c-axis	a-axis	b-axis
Room Temperature (302)	0.65 ± 0.01	0.59 ± 0.01	0.55 ± 0.01
191	0.70 ± 0.01	0.62 ± 0.01	0.56 ± 0.01
333	0.61 ± 0.01	0.57 ± 0.01	0.54 ± 0.01

3.4.2 Thermal conductivity Ellipsoids

When a temperature gradient is present in a material heat will always flow from the hotter to colder region to achieve thermal equilibrium. As we know thermal conductivity is the property that relates heat flow to the temperature gradient. In an isotropic material

$$J = k (dT/dr)$$

Where J = heat flow, k = thermal conductivity, dT / dr = temperature gradient
For an anisotropic material heat flow J is given by

$$J = k (\text{grad } T)$$

i.e. The variation of anisotropic properties such as conductivity can conveniently be by a representation surface. In many case this is an ellipsoid. Consider k_1, k_2, k_3 as the directional cosines and x, y, z as the principal values. Then

$$k = k_1 l^2 + k_2 m^2 + k_3 n^2$$

where $l = x/r$, $m = y/r$, and $n = z/r$, here r is an arbitrary vector

On further simplification we can reach into a form as

$$(x^2/a^2) + (y^2/b^2) + (z^2/c^2) = 1$$

This represents an ellipsoid.

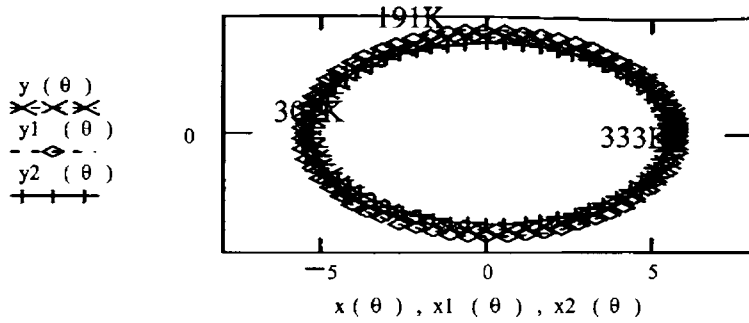
The thermal conductivity ellipsoids normal to the three symmetry axes have been plotted. These ellipsoids are plotted using the values of thermal conductivity about the three principal axes.

As can be seen from the thermal conductivity ellipsoids drawn at different temperatures the general nature of the ellipsoids does not change with temperature. This means that the nature of anisotropy in thermal conductivity do not change with temperature or during phase transition.

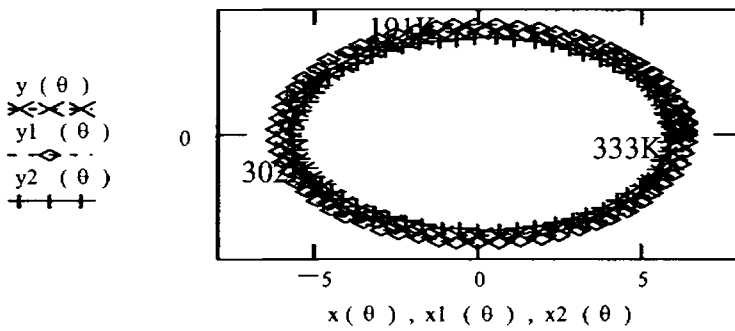
3.4.3 Other Results

From the TGA/ DTA curves it is evident that the decomposition of the sample is maximum at 387°C, and the rate of decomposition is also maximum at this temperature. From the FTIR spectrum of the DLP crystal we can get information about the chemical bonds and their motions in the crystal. The peaks from 2280-2971 cm^{-1} correspond to the C-H stretch mode. Peak at 1581 cm^{-1} represent the asymmetric stretching mode of C-O bond and the one at 1484 cm^{-1} represents symmetric stretching of the C-O bond. Scissoring mode of CH_2 is reflected by the peak at 1465 cm^{-1} and the peak at 1077 cm^{-1} corresponds twisting and wagging modes. The C-O stretching coupled with C-C stretching is manifested by the peak at 1299 cm^{-1} . Peaks from 590 -890 cm^{-1} correspond to rocking mode and the peak at 498 cm^{-1} is possibly due to metal oxygen bond. Thus all the chemical bonds and their motions are revealed by the FTIR spectrum.

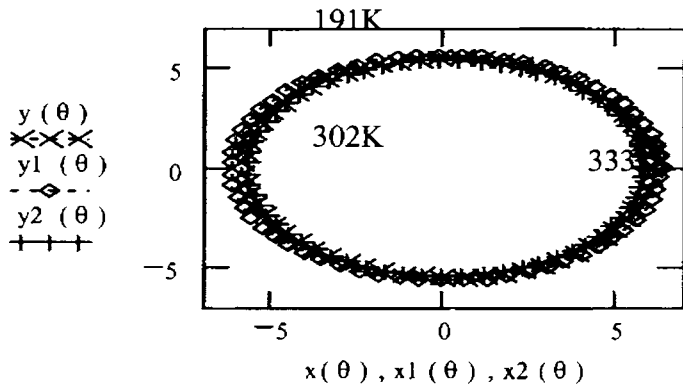
The heat capacity of DLP reported earlier [10] at 191 K compares well with the value obtained from our thermal wave measurements. Our results indicate that photopyroelectric thermal wave measurements can bring out the variation of thermal transport properties such as thermal diffusivity, thermal conductivity and heat capacity of crystalline samples during their



Thermal conductivity ellipsoids perpendicular to a-axis



Thermal conductivity ellipsoids perpendicular to b-axis



Thermal conductivity ellipsoids perpendicular to c-axis

Fig.3.18: Thermal conductivity ellipsoids of DLP crystal about the three principal axes

phase transitions. These measurements help to understand the lattice properties of such crystals and their variations with temperature.

REFERENCES

1. N. Nakamura, H. Suga, H. Chihara and S.Seki, *Bull. Chem. Soc. Jpn.*, **8**, 1779 (1965).
2. N. Nakamura, H. Suga, H. Chihara and S.Seki, *Bull. Chem. Soc. Jpn.*, **41**, 291 (1978)
3. K.Gesi and K.Ozawa, *J. Phys. Soc. Jpn.*, **39**, 1026 (1975)
4. K.Gesi, *J.Phys.Soc.Jpn.*,**53**,1602 (1984)
5. E. Ferroni and P. Orioli, *Z. Krist.*, **111** ,362, (1959)
6. T.Osaka, Y.Makita and K.Gesi, *J.Phys.Soc.Jpn.*, **38**, 292 (1975)
7. Y.Nagae, M.Wada, Y.Ishibashi and Y.Takagi, *J. Phys. Soc. Jpn.*, **41**, 1659 (1976)
8. M.Takashige, S .Hirotsu, S.Sawada and K.Humano, *J. Phys. Soc. Jpn*, **45**, 558 (1978)
9. S.V.Bhat, V.Dhar and R.Srinivasan, *Ferro-electrics (GB)*,**39**, 1167 (1981)
10. K.V.S.Badarinath and S.Radhakrishna, *J. Mat. Sci. Lett.*, **3**, 75 (1984)
11. K.Standnicka, A.M.Glazer and U.Bismayer, *Phase transitions*, **27**, 73 (1990)
12. K.Sushil Misra and Stainslaw Jerzak , *Phy.Rew.B*, **39**, 2041 (1989)
13. J.C.Jacco, G.Kostecky and G.M.Loiacono, *J.cry.grth.*, **51**, 477 (1981)
14. C.P. Menon and J. Philip, *Meas. Sci. &Tech*, **11**, 1744 (2000)
15. M. Marinelli, F. P. Murtas, M. G. Mecozzi, U. Zammit, R.Pizzoferrato, F. Scudierri, S. Maerwillucci, and M. Marinelli, *Appl. Phys. A: Solid Surf.*, **51**, 387 (1990)
16. J.F.Nye: *Physical properties of crystals*. Claredon, Oxford: 1957
17. C.Preethy Menon, J.Philip, A.Deepthy and H.L.Bhat, *Mat.res.bull*, **36**, 2407 (2001)
18. C.Preethy Menon and J.Philip, *Ferroelectrics*, **287**, 63 (2003)

Chapter 4

Thermal transport properties across the Incommensurate phase in Potassium Selenate

4.1 INTRODUCTION

The appearance of incommensurate phases exhibited by several ferroelectric crystals is an interesting phenomenon associated with structural phase transitions. Incommensurate phases were first observed in transition-metal dichalcogenides (Wilson *et.al.* 1974), where the phase transitions are driven by charge-density wave instabilities. Since then the list has been augmented by many dielectric materials, in which the driving mechanisms are not so obvious.

Most of the structural phase transitions are defined by crystal instability against distortion, characterized by a wave vector lying at a special point in Brillouin zone of the high temperature phase. Many interesting physical systems undergo transformations to periodic ordered phases which are incommensurate with the underlying lattices, i.e. the wave vector describing the modulation cannot be formed by simple ratio fractions of reciprocal lattice vectors, and the resulting phase is thus not crystalline. The incommensurate structure may be a condensed charge-density wave (CDW), a static spin-density wave (SPW) or a helical structure, a structural distortion or even a separate atomic lattice [1-3].

The existence of incommensurate phase in a system is represented in Figure 4.1.

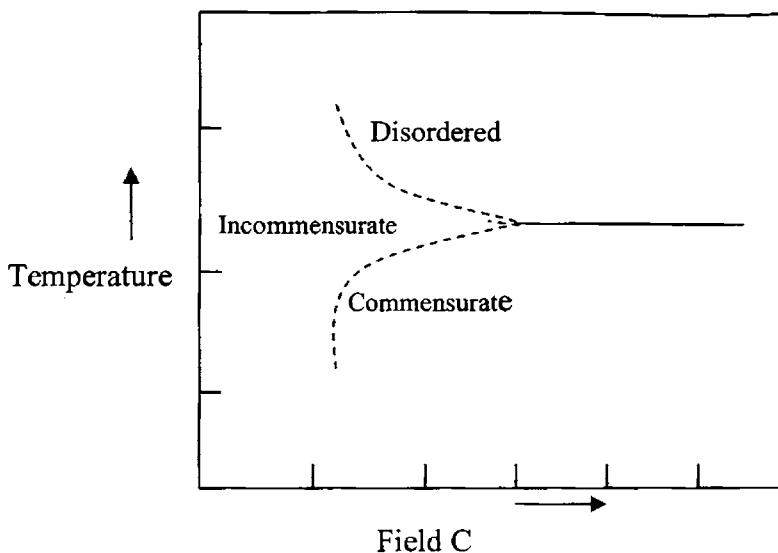


Fig. 4.1: Schematic phase diagram for a system undergoing a transition to an incommensurate phase

In the figure the field C may be thought of as controlling the location of the minimum in location curve of the soft mode [4]. For positive values of C , the minimum in the dispersion occurs at a special point of the Brillouin zone and on cooling the crystal enters a conventional ('commensurate') ordered phase. For negative values of the minimum in the dispersion are shifted from the special point and cooling induces a transition into an incommensurate phase. The point dividing these two portions of the phase boundary has been termed a Lifschitz point [5]. As shown in Fig.4.1, further reduction in temperature can then promote a second transition into a commensurate phase.

A material which has been intensively studied with respect to its incommensurate ordering is Potassium Selenate (K_2SeO_4). Since the discovery of ferroelectricity and successive phase transitions in Potassium Selenate single crystals, many experimental and theoretical studies have

been carried out by different workers to understand the mechanisms of these transitions [6]. With the occurrence of the ferroelectric phase, this material also undergoes an Incommensurate phase (IC-phase) transition, which is of great interest to condensed matter physicists. Ferroelectric crystals, which are known to exhibit IC phase transition includes Ammonium fluoro-berrylate [7], Potassium selenate [8], Sodium nitrite [4], Thiourea [9] etc. Potassium selenate, with the chemical formula K_2SeO_4 , undergoes three successive phase transitions at temperatures $T_1 = 745$ K, $T_2 = 129.5$ K and $T_3 = 93$ K. The different phases and the corresponding structures exhibited by K_2SeO_4 are depicted in Fig. 4.2.

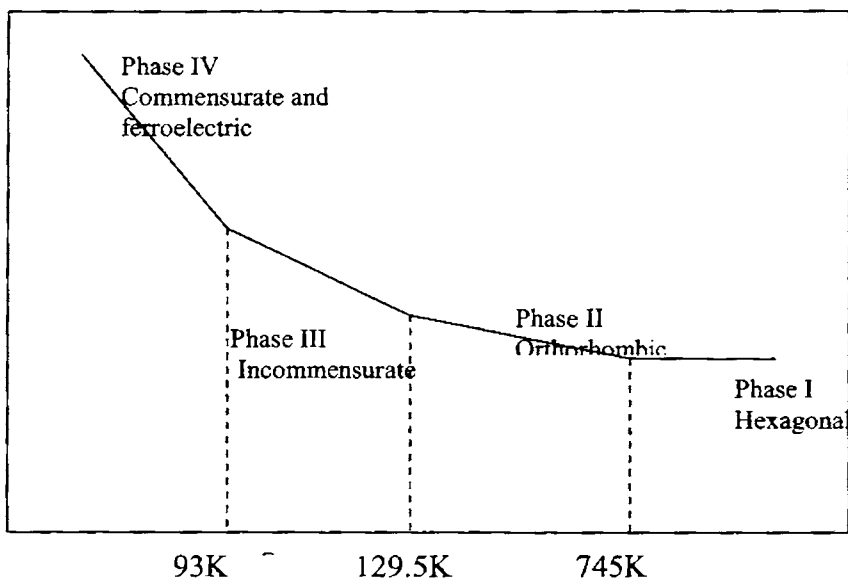


Fig.4.2: Diagram to demonstrate various phases of K_2SeO_4

The crystal exhibits hexagonal structure in Phase I, with space group $D_{6h}^4 (P6_3/mmc)$ [10], which changes to an orthorhombic structure (Phase II) with space group $D_{2h}^{16} (Pnam)$ at T_1 [11]. Then, Phase II changes into an incommensurate one (Phase III) at T_2 , which is a second order phase transition. It undergoes an IC- phase transition at T_3 , below which the crystal is commensurate and ferroelectric with a small spontaneous polarization along the c-direction.

The existence of an IC-phase and transition to the commensurate phase has attracted the attention of many researchers to this crystal as a typical example exhibiting successive phase transitions with a clear IC-phase. Many experimental studies such as dielectric measurements [6, 12], X-ray and neutron diffraction [8, 13-14], ESR [15], Raman and Brillouin scattering [16-18], Ultrasound velocity, attenuation and dispersion [19, 20] etc. have been reported near T_2 and T_3 . The variations of specific heat capacity and thermal expansion of K_2SeO_4 in the low temperature phase have been reported by earlier workers [12, 24]. Thermal expansion along the c-axis exhibits a discontinuity at the incommensurate to commensurate transition. Specific heat measurements show anomalies at T_2 and T_3 , indicating that the transition at T_2 is second order and that at T_3 is first order [12]. In spite of all these measurements reported at temperatures T_3 and T_2 , only very few experimental results have been reported near T_1 [21-25] because of the inherent difficulties involved in carrying out precision experiments at high temperatures. The variation of the specific heat capacity across the structural transition at T_1 has not been reported so far for this material. More experimental data are in fact still required for a better understanding of the high temperature phase of this material.

From neutron scattering measurements it is known that the soft phonon mode occurs at the IC wave vector $\mathbf{q}_0 = (1-\delta) \times \mathbf{a}^*/3 = 0.31\mathbf{a}^*$. In the incommensurate phase this modulating wave vector increases slightly with

decreasing temperature and changes at discontinuously $T_3 = 93\text{K}$ to the commensurate value $q_0 = a^*/3$. Quartic anharmonic interaction between the polar optic mode and the order parameter results in ferroelectricity in the commensurate phase IV (space group $C_{2v}^9 = Pna 2_1$), observable by a spontaneous polarization P_3 and a strong maximum in the dielectric function ϵ_{33} . By undertaking Raman scattering in phase III, dispersion of the amplitude mode (amplitudon) can be measured. In commensurate phase IV a superstructure is formed; now the two phonon modes of symmetry types A_1 and B_1 that emerge from the amplitudon and the phason become observable in light scattering. Anomalies in the molar heat capacity were observed at both transitions $\text{II} \leftrightarrow \text{III}$ and $\text{III} \leftrightarrow \text{IV}$, but considerably weaker at the latter. By Brillouin scattering in K_2SeO_4 the relative variation of the longitudinal sound velocities with temperature were measured around the transition $\text{II} \leftrightarrow \text{III}$.

A dynamic measurement of the thermal conductivity across a transition temperature is rather difficult due to the fact that the sample cannot be kept in a steady state during measurements. Thermal wave measurements based on photo-thermal effect, such as thermal wave interferometry, photo-thermal deflection technique, photo-acoustic methods and photopyroelectric measurements help to get over this difficulty. In these techniques one measures the thermal diffusivity, rather than thermal conductivity. Thermal diffusivity measurements do not suffer from heat losses from the sample during measurements and hence is more accurate than a direct measurement of thermal conductivity by the steady state method. With a proper choice of boundary conditions, photo-thermal/ photo-acoustic techniques makes a simultaneous measurement of thermal diffusivity and effusivity possible, from which the thermal conductivity and specific heat capacity can be extracted. The photo-pyroelectric technique has been used earlier to measure the variations of thermal conductivity and heat

capacity of a few crystalline solids as they undergo phase transitions with temperature [26, 27].

In this chapter we report the results of our measurement of the thermal diffusivity, thermal conductivity and heat capacity of K_2SeO_4 as it goes through the IC-phase between 129.5 K and 93 K. The anisotropy in thermal conductivity along the three principal directions of this crystal and its variation with temperature are brought out and discussed. Differential scanning calorimetric (DSC) measurements across the high temperature phases have been carried out to determine anomalies in enthalpy during the transition from Phase I to Phase II, and the ratio method adopted to determine the variation of specific heat capacity with temperature across the high temperature transition point T_1 . We have combined the results from photopyroelectric and calorimetric measurements to plot the variation of specific heat with temperature through all the four phases of K_2SeO_4 , and the results are discussed.

4.2 SAMPLE PREPARATION

K_2SeO_4 crystals are grown from solution following the well known method of slow evaporation technique. Selenous acid (H_2SeO_3) is refluxed to get selenic acid (H_2SeO_4) using hydrogen peroxide. Then potassium carbonate and selenic acid are taken in stoichiometric proportions to get the solution of potassium selenate following the chemical reaction



The solution is kept in a bath for three to four weeks to get good transparent crystals of K_2SeO_4 of about $1 \times 1 \times 1$ cm³ size. This crystal is isomorphous with $(NH_4)_2SO_4$ in morphology [20]. The morphology of the crystal is shown in

Figure 4.3. The X-ray powder diffraction pattern of the crystal, recorded for structure confirmation, is shown in the Figure 4.4, which agrees well with the diffraction patterns reported earlier.

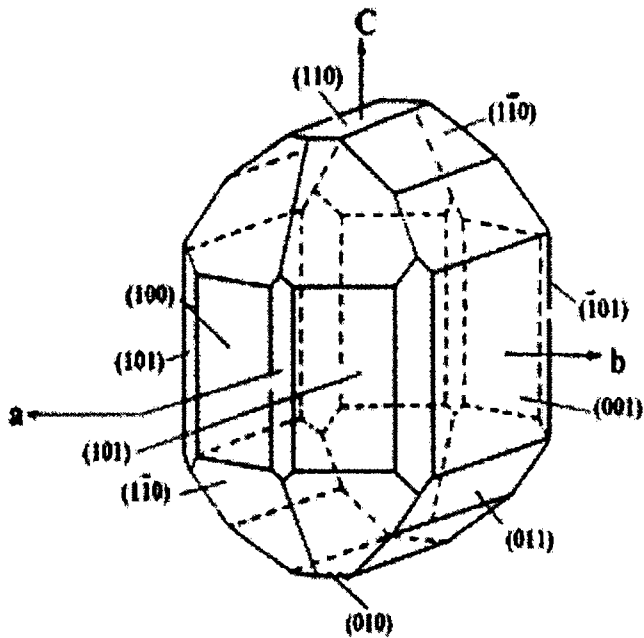


Fig. 4.3: Morphology of K_2SeO_4 crystal

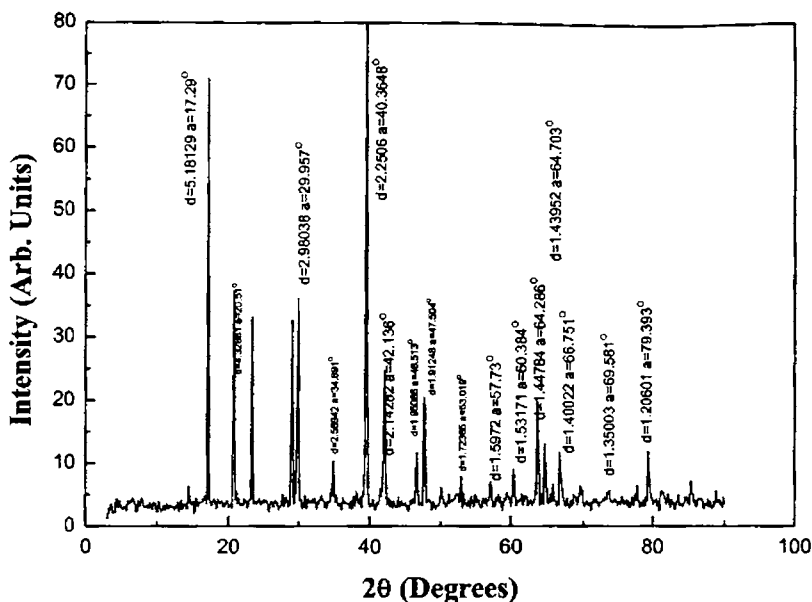


Fig. 4.4: XRD pattern of K_2SeO_4 crystal at room temperature

The crystals are cut with a slow speed diamond wheel saw in such a way that they have faces normal to the [100], [010] and [001] orientations of the crystal, which are designated as a , b and c axes respectively. The samples are carefully polished and made into thickness of about 0.5 mm for photopyroelectric measurements. The density of the sample is measured to be 0.859 g/cm^3 . Pieces of the crystal, weighing about 5 mg, are used for scanning calorimetric measurements.

4.3 EXPERIMENTAL METHODS

4.3.1 Photo-Pyroelectric Thermal Wave Measurements

The improved photopyroelectric (PPE) technique, described extensively in chapter 2, has been used to determine the thermal properties of single crystals of K_2SeO_4 [26, 27]. For this measurement the sample thickness

should be such that the sample, the pyroelectric detector and the backing material used should be thermally thick during the measurement. The sample is illuminated with an intensity- modulated beam of light, which gives rise to periodic temperature variations in the sample by optical absorption. The thermal waves so generated propagate through the sample, and are detected with a pyroelectric detector.

The measurements have been done at temperatures between 85 K and 300 K at temperature intervals of 2 K normally and at intervals of 1 K at temperatures in the vicinity of the two transition points. First, measurements have been done with the sample cut with faces normal to the *c*-axis. At each measurement temperature, the sample has been kept at constant temperature during measurements. From the frequency dependence of the pyroelectric amplitudes and phases, the thermal diffusivity and effusivity of the sample have been determined at each temperature. These measurements have been repeated for samples cut with faces normal to *a*- and *b*- axes as well.

4.3.2 Differential Scanning Calorimetric Measurements

The DSC curve of the sample has been plotted at higher temperatures with a Mettler Toledo DSC 822^e at a heating rate of 10°C/min. In view of the fact that the low temperature transitions in K₂SeO₄ are weak, the variations in specific heat are comparatively small. It is difficult to measure such small variations with enough sensitivity following the DSC technique. In the high temperature region, the variation of specific heat with temperature has been determined by the ratio method with Alumina used as the reference sample. This method results in specific heat capacity values with accuracy better than ± 2.5 %.

4.4 RESULTS AND DISCUSSION

The variations of PPE signal amplitude and phase measured as a function of modulation frequency for K_2SeO_4 sample, measured along the three principal directions at room temperature are shown in figures 4.5 and 4.6 respectively. The temperature variations of amplitude and phase along the a-, b-, c-axis of K_2SeO_4 are shown in Fig.4.7, Fig.4.8, and Fig.4.9 respectively. From the frequency dependence of the pyroelectric amplitudes and phases, the thermal diffusivity and effusivity of the sample have been determined at each temperature. The temperature variations of these parameters along the a-, b- and c-axis of K_2SeO_4 are shown in Fig.4.10, Fig.4.11 and Fig.4.12. From the diffusivity and effusivity values, the corresponding values of thermal conductivity and specific heat capacity have been computed and plotted in Figures 4.13, 4.14 and 4.15 for all three axes.

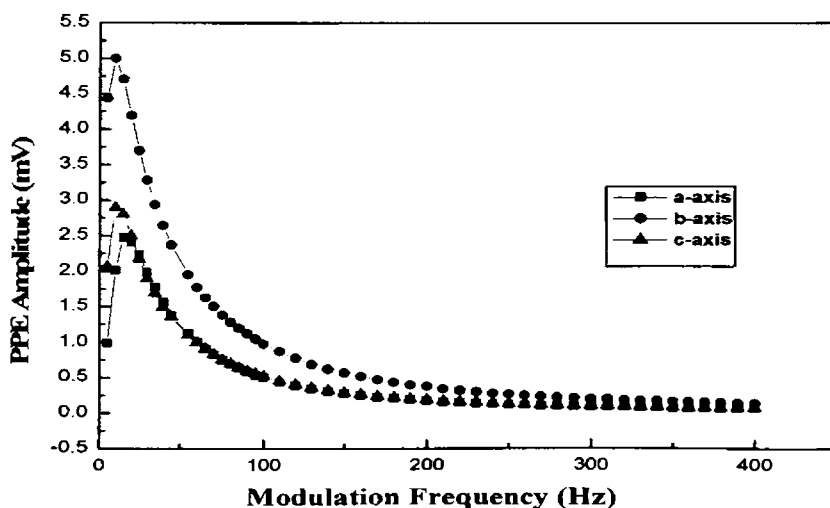


Fig. 4.5: Frequency dependence of photo-pyroelectric amplitudes along the three principal axes of K_2SeO_4

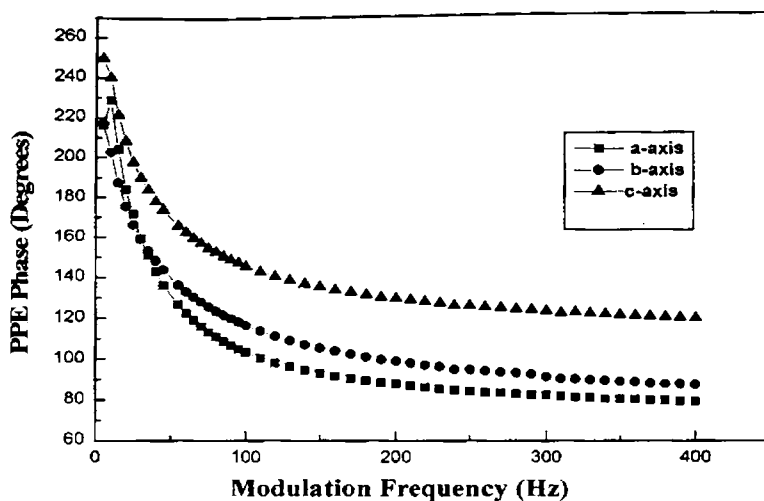


Fig. 4.6: Frequency dependence of the photo-pyroelectric phases along the three principal axes of K_2SeO_4

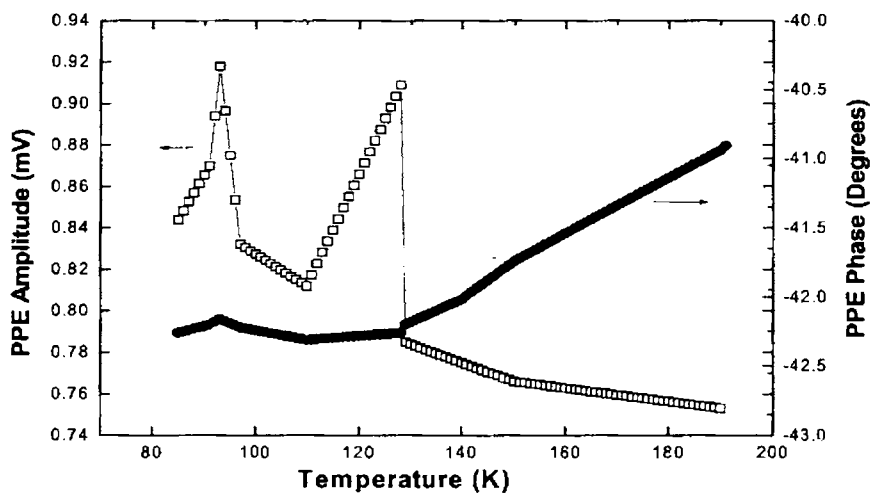


Fig.4.7: Variation of PPE amplitude and phase with temperature along a- axis

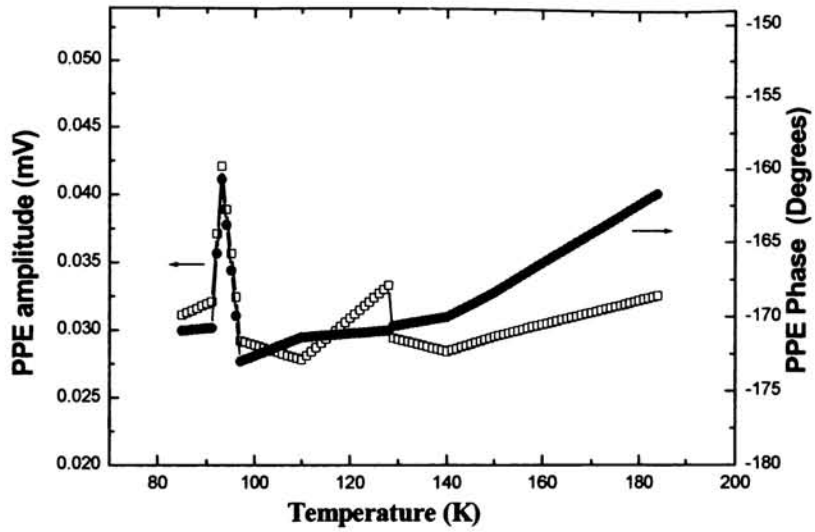


Fig.4.8: Variation of PPE amplitude and phase with temperature along b- axis

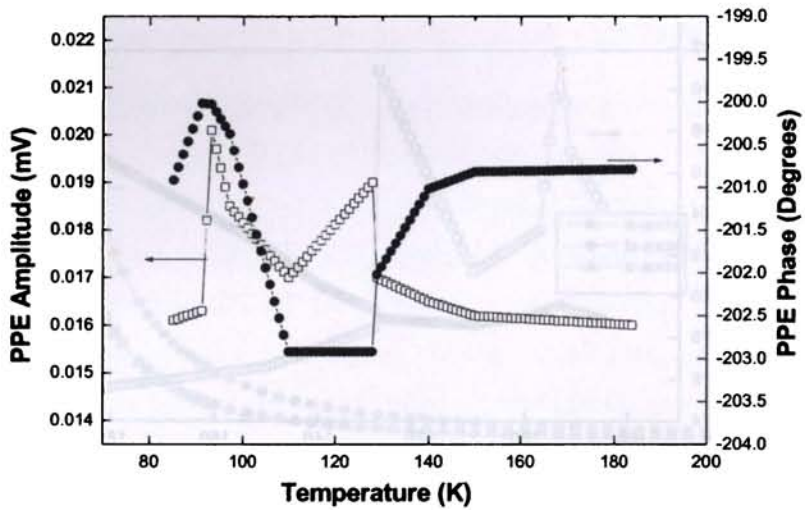


Fig.4.9: Variation of PPE amplitude and phase with temperature along c- axis

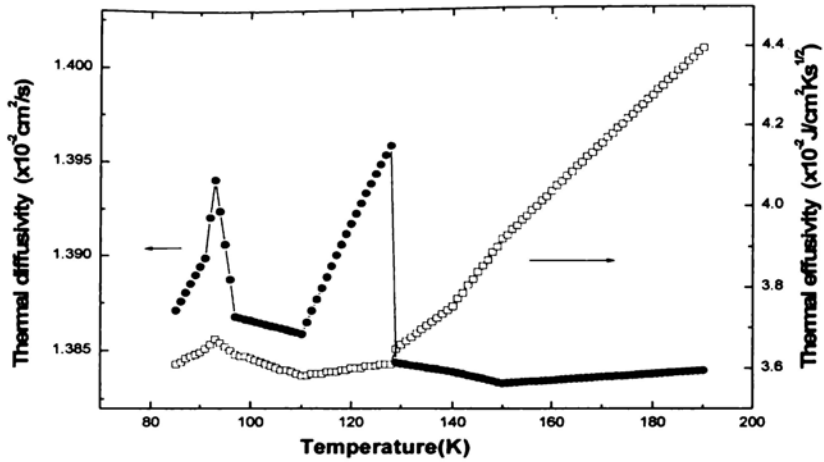


Fig.4.10: Variation of thermal diffusivity and thermal effusivity with temperature along a- axis

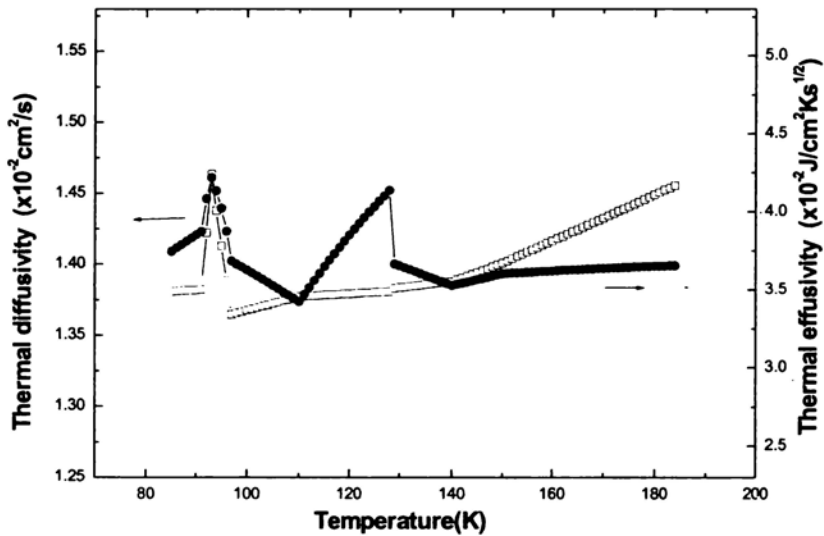


Fig.4.11: Variation of thermal diffusivity and thermal effusivity with temperature along b- axis

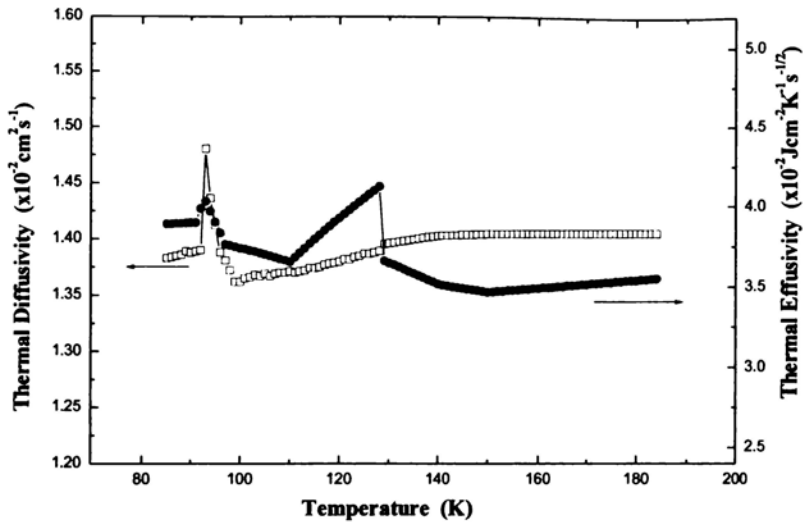


Fig.4.12: Variation of thermal diffusivity and thermal effusivity with temperature along c- axis

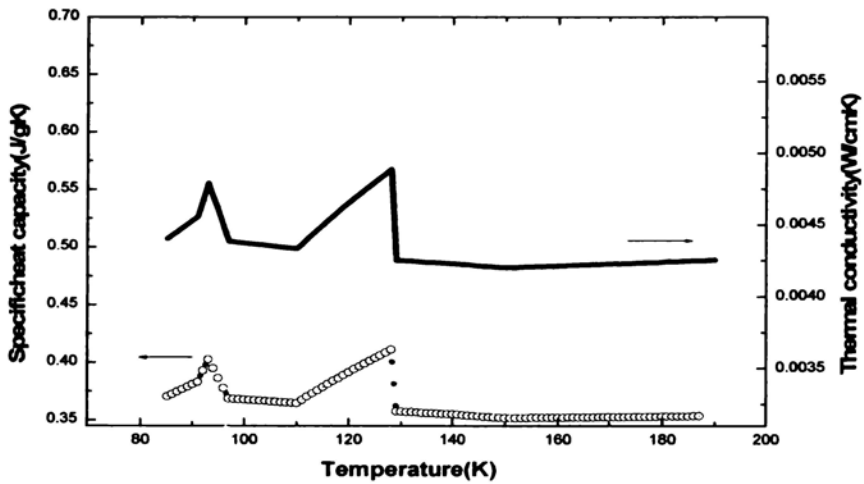


Fig.4.13: Variation of specific heat capacity and thermal conductivity with temperature along a- axis

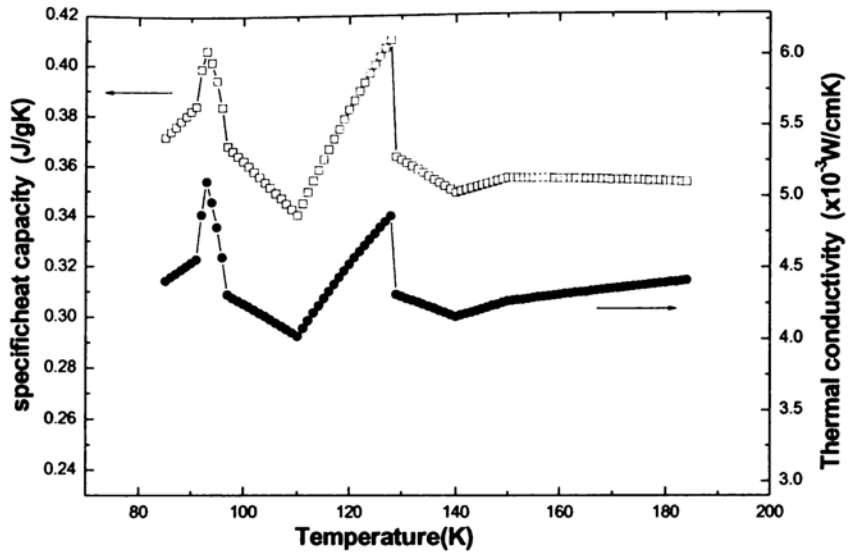


Fig.4.14: Variation of specific heat capacity and thermal conductivity with temperature along b- axis

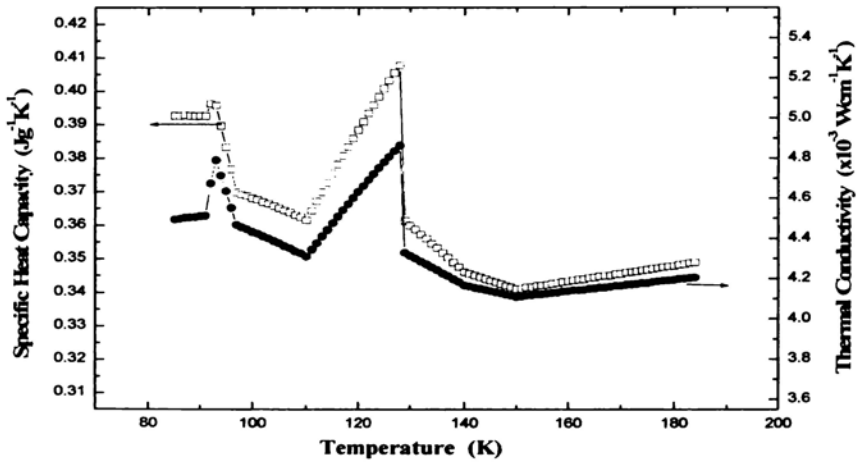


Fig.4.15: Variation of specific heat capacity and thermal conductivity with temperature along c- axis

The numerical values of thermal conductivity of K_2SeO_4 along the three symmetry axes at room temperature, as well as at 93 K and 129.5 K, are tabulated in Table 4.1.

Table 4.1 Thermal conductivity (in units of $10^{-3}W\ cm^{-1}\ K^{-1}$) along the three principal axes of K_2SeO_4 at different temperatures

Temperature K	a - axis	b - axis	c - axis
Room Temperature (302)	4.21 ± 0.01	4.22 ± 0.01	4.41 ± 0.01
127	4.86 ± 0.01	4.88 ± 0.01	5.10 ± 0.01
93	4.79 ± 0.01	4.78 ± 0.01	4.80 ± 0.01

From this table one can estimate the anisotropy in thermal conductivity for potassium selenate at room temperature as well as at the two transition temperatures below room temperature. One can see that the thermal conductivity along the *c*-axis, which is the direction of spontaneous polarization for this crystal, is slightly more than those along *a* or *b* - axes at all temperatures. The anisotropy in thermal conductivity, in general, is small and decreases as the temperature is lowered. The thermal conductivity ellipsoids for all the three axes have been drawn with the corresponding thermal conductivity values at the two low temperature transitions as well as at room temperature to demonstrate the extent of thermal conductivity anisotropy in this crystal. The thermal conductivity ellipsoids at room temperature, 129.5K, and 93K are shown in figures 4.16 (a, b and c).

The variations of thermal diffusivity (α), effusivity (e), thermal conductivity (k) and specific heat capacity (c_p) with temperature along the c -axis of K_2SeO_4 , shown in figures 4.13 and 4.15, clearly indicate that the above thermal properties undergo anomalous variations during phase transitions at 93 K and 129.5 K. Figure 4.15 clearly shows that thermal conductivity and heat capacity exhibit maxima at the phase transition temperatures 93 K and 129.5 K. Moreover, it can be seen that there is an overall enhancement in thermal conductivity in the IC-phase of K_2SeO_4 between 93 K and 129.5 K. The maxima in thermal conductivity at the phase transition temperatures can be explained in terms of the increase in phonon mean free path or decrease in phonon-phonon and phonon-defect collision rates. Again, the anomalous variation in specific heat capacity is due to softening of phonon modes and the corresponding enhanced contribution of phonon modes to specific heat capacity.

The IC-phase in K_2SeO_4 has been observed experimentally as satellite peaks in the X-ray and neutron diffraction patterns. In the IC-phase of K_2SeO_4 at temperatures close to T_2 , the incommensurate modulation wave is purely harmonic, but as the temperature approaches T_3 , nonlinear phase modes, which are equally spaced commensurate constant phase domains separated by narrow phase varying regions called phase solitons emerge. The presence of these modulation waves or phase solitons can influence heat conduction in ferroelectric crystals in two different ways. The usual expression for thermal conductivity k in an insulating crystal is given by

$$k = (1/3) c v l \quad (4.1)$$

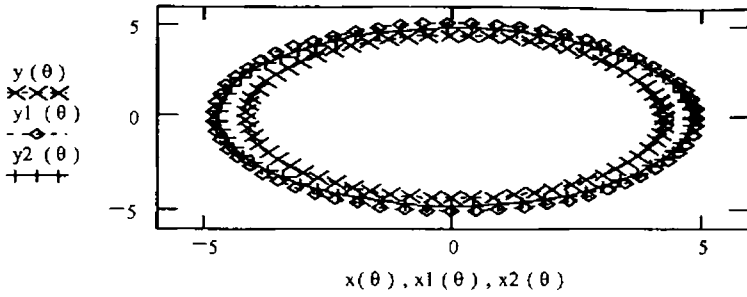


Fig.4.16: (a) Thermal conductivity ellipsoids perpendicular to a-axis

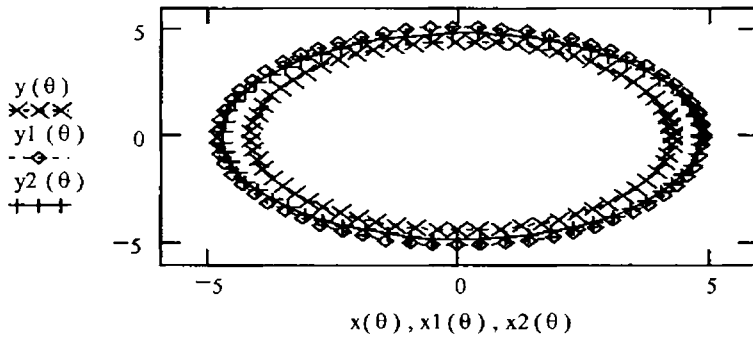


Fig.4.16: (b) Thermal conductivity ellipsoids perpendicular to b-axis

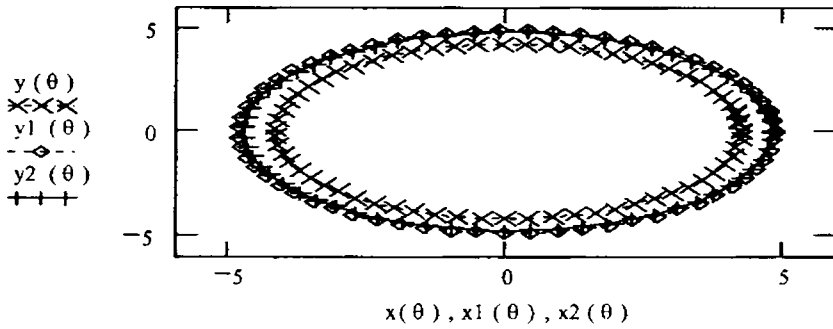


Fig.4.16: (c) Thermal conductivity ellipsoids perpendicular to c-axis

where c , v and l denote the phonon specific heat, the phonon group velocity and the phonon mean free path respectively. The phase solitons can affect the mean free path by phonon scattering and hence can cause anomalous variation of thermal conductivity in the IC-phase. Another possibility is that the modulation waves themselves can act as heat carriers, resulting in an enhancement in thermal conductivity. Whether thermal conductivity increases or decreases during an IC phase transition depends on which factor dominates in the process. One can isolate thermal conductivity enhancement in the IC-phase by computing the value of $k-k_{bg}$ where k is the total thermal conductivity and k_{bg} is the background thermal conductivity in the absence of occurrence of the IC-phase. In general, for an insulating crystal, k_{bg} follows an inverse T behavior.

As can be seen from the thermal conductivity ellipsoids drawn at different temperatures the general nature of the ellipsoids does not change with temperature. This means that the nature of anisotropy in thermal conductivity do not change with temperature or during phase transition.

The DSC curve during the heating cycle shown in Fig.4.17 shows a clear peak occurring at 745 K indicating that the phase transition at this temperature is endothermic. The variation of specific heat capacity with temperature to a temperature well above 745 K has been determined by the DSC ratio method. These results have been combined with the results shown in Fig. 4.15 to plot the variation of heat capacity with temperature encompassing all the four phases of K_2SeO_4 . This is shown in Fig.4.18. The variation of the specific heat capacity around the high temperature transition around 745 K is shown in the inset of Fig. 4.18.

To the best of our knowledge, this is the first time the variation of the specific heat of K_2SeO_4 through all the three transition

temperatures T_1 , T_2 and T_3 (and through all the four phases) is plotted. The anomalous variation in heat capacity during transitions can be understood as due to softening of the phonon modes and the corresponding enhanced contribution of phonon modes to the specific heat capacity.

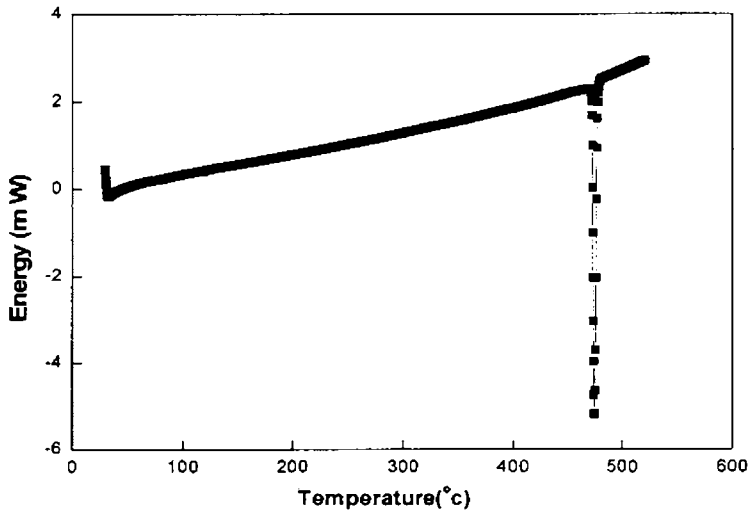


Fig.4.17: DSC curve during the heating cycle

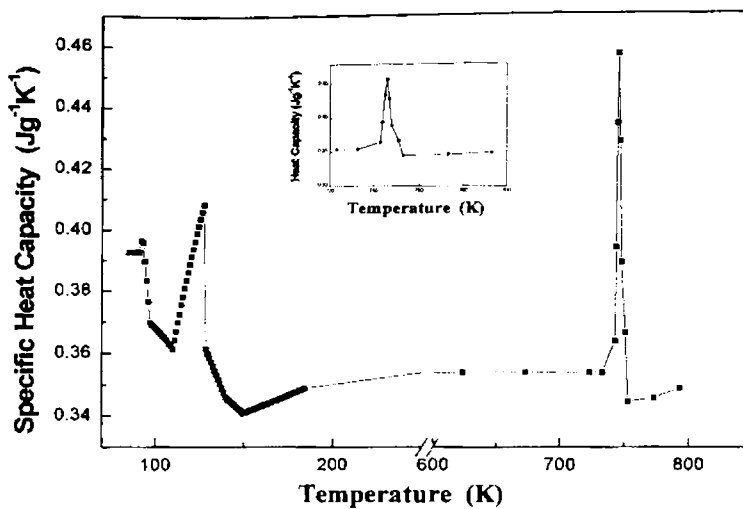


Fig.4.18: Variation of specific heat capacity with temperature through all the four phases of K_2SeO_4 . The inset shows the variation close to the high temperature transition point

REFERENCES

1. J. D. Axe, *Oak Ridge laboratory report CONF-760601-P1*, 353 (1976)
2. R. A. Cowley and A.D. Bruce, *J.Phys.C : Solid State Phys.*, **11**, 3577 (1978)
3. P. Bak and J. Timonen, *J.Phys.C : Solid State Phys.*, **11**, 4901 (1978)
4. A.D. Bruce, R. A. Cowley and A. Murray, *J.Phys.C : Solid State Phys.*, **11**, 3591 (1978)
5. R. M. Hornreich, M. Luban and S. Shtrikman, *Phys. Rev. Lett.*, **35**, 1678 (1975)
6. K. Aiki, K. Hukuda and O. Matumura, *J.Phys.Soc.Jpn.*, **26**, 1064 (1969)
7. M. Iizumi and K. Gesi, *Solid State Commun.* **22**, 37 (1977)
8. M. Iizumi, J. D. Axe, G. Shirane and K. Shimaoka, *Phys.Rev.B.*, **15**, 4392 (1977)
9. Y. Yamada, I.Shibuya and S.Hoshino, *J.Phys.Soc.Jpn.* **18**, 1594 (1963)
10. G. J. Goldsmith and J. G. White, *J.Chem.Phys.*, **31**, 1175
11. S. Shiozaki, A. Sawada, Y. Ishibashi and Y. Takagi, *J.Phys.Soc.Jpn.*, **43**, 1314 (1977)
12. A. Kálmán, J. S. Stephens and D. W. J. Cruickshank, *Acta Cryst.B*, **26**, 1451 (1970)
13. K. Aiki, K. Hukuda, H. Koga and T. Kobayashi, *J.Phys.Soc.Jpn.*, **28**, 389 (1970)
14. N. Ohama, *Mat. Res. Bull.*, **9**, 283 (1974)
15. H.Terauchi, *J.Phys.Soc.Jpn.*, **39**, 435 (1975)
16. K. Aiki, *J.Phys.Soc.Jpn.*, **29**, 379 (1970)
17. M.Wada, A.Sawada, Y. Ishibashi and Y. Takagi, *J.Phys.Soc.Jpn.*, **42**, 1229 (1977)

18. M. Wada, H. Uwe, A. Sawada, Y. Ishibashi, Y. Takagi and T. Sakudo, *J.Phys.Soc.Jpn.* **43**, 544, (1977)
19. T. Yagi, M. Cho and Y. Hidaka, *J.Phys.Soc.Jpn.*, **46**, 1957 (1979)
20. H.Hoshizaki, A. Sawada, Y. Ishibashi, T. Matsuda and I. Hatta, *Jpn.J. Appl. Phys.*, **19**, L324 (1980)
21. S. Shiozaki, A. Sawada, Y. Ishibashi and Y. Takagi, *J.Phys.Soc.Jpn.*, **43**, 1314 (1977)
22. H. G. Unruh, W. Eller, G. Kirf, *Phys.Status Solidi a.*, **55**, 173 (1979)
23. K. Inoue, K. Suzuki, A. Sawada, Y. Ishibashi and Y. Takagi *J.Phys.Soc.Jpn.* **46**, 608 (1979)
24. M. Cho and T.Yagi, *J.Phys.Soc.Jpn.* , **49**, 429 (1980)
25. S. S. Gupta, S. Karan and S.P.S.Gupta, *Jpn. J. Appl. Phys.*, **39**, 2736 (2000)
26. C. P. Menon And J. Philip, *Meas. Sci. &Tech.*, **11**, 1744 (2000)
27. M. Marinelli, F. P.Murtas, M.G.Mecozzi, U.Zammit, R.Pizzoferrato, F. Scudierri, S. Maerwillucci, and M. Marinelli, *Appl. Phys. A: Solid Surf.* **51**, 387 (1990)

Chapter 5

Thermal transport properties of $\text{La}_{(1-x)}\text{Te}_x\text{MnO}_3$ ($x= 0, 0.1, 0.15, 0.2$) exhibiting giant magneto resistance

5.1 INTRODUCTION

5.1.1. Giant magneto resistance

The phenomenon of magnetoresistance (MR) is the change in electrical resistance (R) of a material in response to an externally applied magnetic field (H). Mathematically, it is written as $MR = [R(H) - R(0)]/R(0)$, where $R(H)$ and $R(0)$ are the resistances of the material in the presence of applied magnetic field and zero fields, respectively. The electrical resistance in a material arises due to the processes of scattering (collision) of electrons with lattice phonons, other electrons, impurities, lattice defects etc. and the corresponding scatterings are electron–phonon scattering, electron–electron scattering, electron–impurity scattering, etc. In a real crystal, the atoms are not fixed at the equilibrium lattice positions, but they always vibrate around their equilibrium position due to thermal energy. When electrons pass by these vibrating atoms, they get scattered (electron–phonon interaction) and contribute to electrical resistance. In a real world, it is impossible to get a crystal completely devoid of defects or impurities. So, during the flow, the electrons get scattered by these impurities or defects as well as other electrons. When a normal material is subjected to an external magnetic field (\mathbf{B}), the trajectories of the electrons inside the material get deviated and they follow a helical path due to the Lorentz force [$q(\mathbf{v} \times \mathbf{B})$], where q is charge and \mathbf{v} is velocity, resulting in an increase in the probability of scattering.

This process usually gives a small positive ordinary magnetoresistance (OMR) of the order of 1% or so in the field of order of 1 Tesla and varies as B^2 in low field regime. It also does not saturate with increasing field.

In the year 1857, W. Thomson (Lord Kelvin) discovered a new phenomenon when he was measuring the resistance of iron and nickel in the presence of a magnetic field [1]. He found a 0.2% increase in the resistance of Fe when the magnetic field was applied longitudinally and a 0.4% decrease in resistance when the field was applied in transverse direction. This phenomenon is known as anisotropic magnetoresistance (AMR). It originates from anisotropic spin-orbit interaction and causes the resistance to depend on the relative orientation of electric current and magnetization. However, it was subsequently found that at room temperature, the AMR in bulk alloys of Ni-Fe and Ni-Co could be of the order of 3–5%. AMR thin films were used for the magneto resistive effects in connection with read out heads for magnetic disks and as magnetic field sensors. The 151-year-old AMR remained as the main source of magnetoresistance in ferromagnets till 1988, and there was hardly any improvement in the performance of magneto resistive materials with time. The general consensus in the 1980s was that it was not possible to significantly improve the performance of magnetic sensors based on magneto resistive effect.

In 1988, there was an upsurge in the field of magnetoresistance as Fert's group in France discovered that the application of magnetic field to a Fe/Cr multilayer results in a huge reduction of electrical resistance, which was found to be much higher than OMR and AMR and named it as giant magnetoresistance (GMR) [2]. A similar effect in Fe/Cr/Fe trilayer structure was simultaneously discovered by Grünberg's group in Germany [3]. Both the above mentioned structures were grown by Molecular Beam Epitaxy (MBE) technique. Therefore, the discovery of GMR was solely possible due to the development in thin film deposition techniques such as MBE,

sputtering, etc., and surprisingly it was found that the layered system grown by these techniques were completely different in their properties from their constitutive bulk material. Albert Fert and Peter Grünberg were awarded the Nobel Prize in 2007 for their independent discovery of GMR.

Like the other magneto resistances (OMR, AMR), GMR is also a change in electrical resistance in response to an externally applied magnetic field, and is a quantum mechanical effect which is based on spin-dependent scattering phenomenon in magnetic multilayers. The change in resistance of the multilayer occurs when the applied magnetic field aligns the magnetic moments (magnetization) of successive ferromagnetic layers as shown in Figure 5.1. In the absence of applied magnetic field, the magnetic moments of magnetic layers are not aligned with respect to each other i.e., their magnetizations are antiparallel to each other and it results in higher resistance. By applying a magnetic field, the magnetic moments of successive ferromagnetic layers get aligned i.e., their magnetizations are parallel to each other and it results in a drop in resistance of the multilayer. Mathematically, GMR can be defined as $GMR = (R_{AP} - R_P) / R_P$, where R_P and R_{AP} are the resistances in parallel and antiparallel states. Unlike ordinary magnetoresistance, the GMR saturates with applied magnetic field as shown in Figure 5.1.

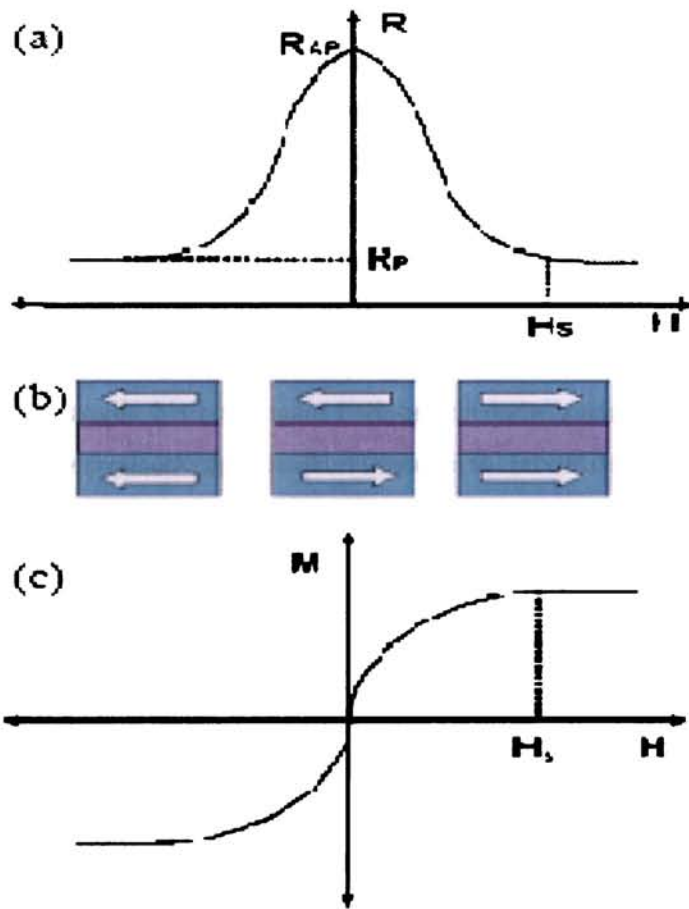


Fig. 5.1. Schematic representation of the GMR effect. (a) Change in the resistance of the magnetic multilayer as a function of applied magnetic field. (b) The magnetization arrangement (indicated by the arrows) of the multilayer (trilayer) at various magnetic fields; the magnetizations are aligned antiparallel (AP) at zero field and are aligned parallel (P) when the external magnetic field $H >$ saturation field (H_S). (c) M-H curve for the multilayer

In order to observe GMR in a magnetic multilayer, one must be able to orient the magnetic moments of the ferromagnetic layers in the parallel direction by applying a magnetic field and in zero field they should have antiparallel magnetization arrangement. This antiparallel magnetization arrangement in a multilayer is achieved due to interlayer exchange coupling which is antiferromagnetic (AF) in nature. The interlayer exchange coupling is mediated by the mobile electrons in the non-magnetic spacer layer like Cr and is analogous to Ruderman–Kittel–Kosuda–Yosida (RKKY) interaction between localized magnetic moments present in a matrix of non-magnetic metal. The interlayer exchange coupling oscillates between ferromagnetic and antiferromagnetic as a function of the non-magnetic spacer layer thickness. By suitably and judiciously tuning the non-magnetic spacer layer thickness, one can have antiparallel magnetization alignment in zero field. It is not that the antiferromagnetic interlayer exchange coupling is the only way to achieve GMR; there are other ways to achieve it. Antiparallel magnetization alignment can also be achieved by introducing ferromagnetic layers of different coercivities (pseudo-spin valve structure), i.e., by a combination of soft and hard ferromagnetic layers. In this case, the magnetic moments of the soft and hard ferromagnetic layers switch at different values of applied magnetic field providing a window of field values in which the layers remain in an antiparallel state with respect to each other, and thus leading to high resistance. Once the applied magnetic field crosses the coercive field (H_c) of hard ferromagnetic layer, both the layers align in parallel state leading to low resistance. Another way to change the alignment of the ferromagnetic layers is to tune the coercivity of one ferromagnetic layer to a higher value. This is possible when one ferromagnetic layer is pinned by the exchange coupling with an adjacent antiferromagnetic layer (spin valve structure). The other unpinned ferromagnetic layer is free to rotate with the applied magnetic field, thus providing a parallel or an

antiparallel state. Though the GMR value in a magnetic multilayer is higher, spin valves are more attractive because of the small magnetic field required to change the resistance of this structure. Magnetic granular systems are also ideal candidates from the GMR point of view. In these materials ferromagnetic precipitates are embedded in a non-magnetic host metal film. The randomly oriented ferromagnetic precipitates tend to align with which the application of magnetic field leads to a drop in the resistance. The different types of systems described above which exhibit GMR behavior are shown in Figure 1.2.

The origin of GMR can be understood by only considering the spin-dependent effects. According to Mott, the electrical conductivity in a metal can be described in terms of two largely independent conducting channels corresponding to up and down spins respectively. Total conductivity is represented by the two-current model as, $\sigma_{\text{Total}} = \sigma_{\uparrow} + \sigma_{\downarrow}$ (keeping in mind that there occurs no spin flip scattering). According to him, the electric conduction takes place by the *sp* band electrons primarily as they have lower effective mass and higher mobility. As the *d* band is exchange split in ferromagnets, the density of states for up and down band is different at the Fermi level. Therefore, the probability of scattering for up and down *sp* electrons into the states near the Fermi level are different. So, the conductivities are different for the two conduction channels.

Using Mott's simple argument, it is possible to understand the origin of GMR in magnetic multilayer. Let us consider a collinear magnetic configuration of two magnetic layers separated by a non-magnetic spacer layer as shown in Figure 1.3. We will assume that the scattering is strong for spins antiparallel to magnetization direction and weak for parallel magnetization direction. In case of parallel configuration, the spin-up electrons are weakly scattered in all layers and leads to spin-down electrons

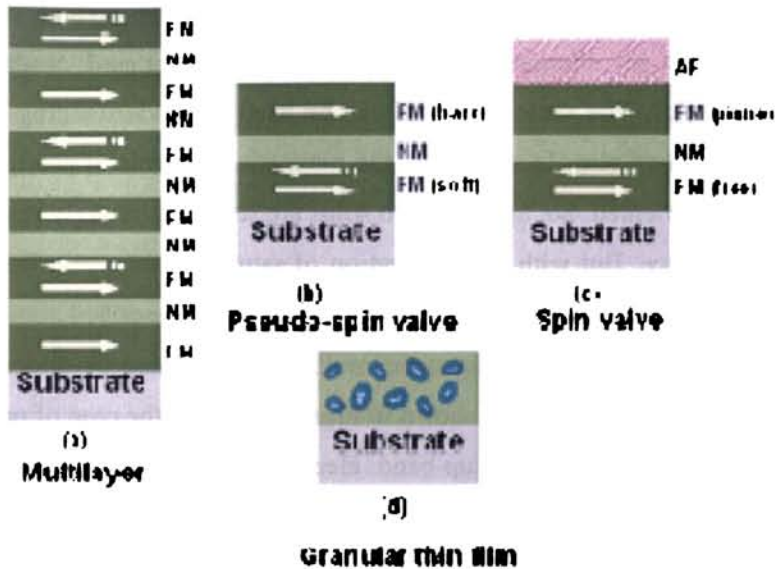


Fig. 1.2. Different GMR structures (a) multilayer (b) pseudo spin valve (c) spin valve (d) granular thin film. (a) In the multilayer the ferromagnetic layers (FM) are separated by non magnetic (NM) spacer layers. At zero field, ferromagnets are aligned antiparallel as indicated by full and partial solid arrows. At saturation field the magnetic moments are aligned parallel (the solid arrows). (b) In the pseudo spin valve, the magnetic structure com a hard and soft magnetic layer; the switching of ferromagnetic layers occur at different magnetic fields providing a change in the relative orientation of magnetization. (c) In the spin valve, the top FM is pinned by the attached antiferromagnetic (AF) layer. The bottom FM layer is free to rotate by applied magnetic field. (d) In the granular material, magnetic precipitates are embedded in the non-magnetic metallic material. The application of magnetic field aligns the magnetic moments of randomly oriented granules.

are strongly scattered in magnetic layers so that they weakly participate to the conduction of current. But in low resistance but, in contrast, the Non magnetic layer thickness the case of antiparallel configuration, both up and down electrons get alternately strongly and weakly scattered, leading to higher resistance. The same argument can be used for understanding GMR in granular system also. In zero field, the magnetic moments of precipitates are randomly oriented. So, up and down spins are scattered strongly resulting in high resistance. But with the application of saturating magnetic field, all the precipitates align and it results in low resistance. As described above, the spin dependent scattering in magnetic multilayers can also be understood from the band structure picture shown in Figure 1.3: (i) In the case of parallel magnetization alignment, the up-band electrons from one ferromagnetic layer can be transported to the other ferromagnetic layer due to the availability of density of states at the Fermi level, and this leads to low resistance. (ii) For the antiparallel case the transport of up electrons from one ferromagnetic layer to other is not allowed and it results in high resistance. Thus depending on the direction of magnetization of a material with respect to spin polarization of the current, a material can behave either as an insulator or a conductor. A classic analogy can be made with the phenomenon of polarized light passing through the analyzer. However, in optical case crossing the polarizer axis at 90° with respect to analyzer axis prevents the transmission of light, whereas for spin-polarized electrons the magnetization of successive layers should be rotated by 180° to stop the electrical conduction.

5.1.2 Manganese oxides

Mixed valence manganites with the perovskite structure has been studied for almost 60 years. The system offers a degree of chemical flexibility that permits the relation between the oxide's structure, electronic and magnetic

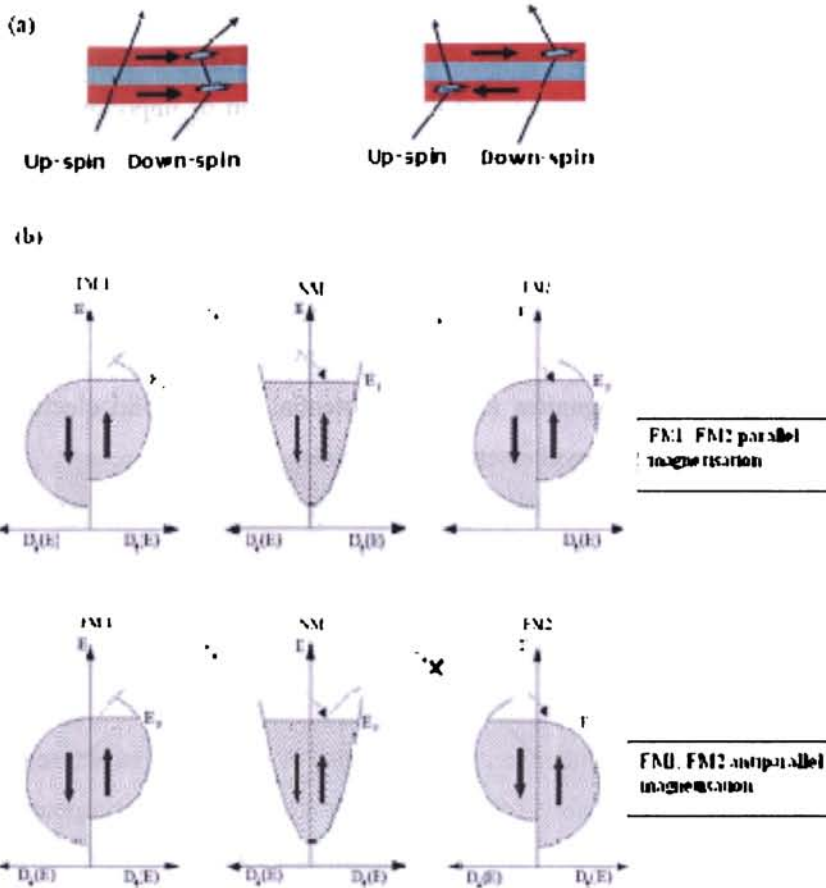


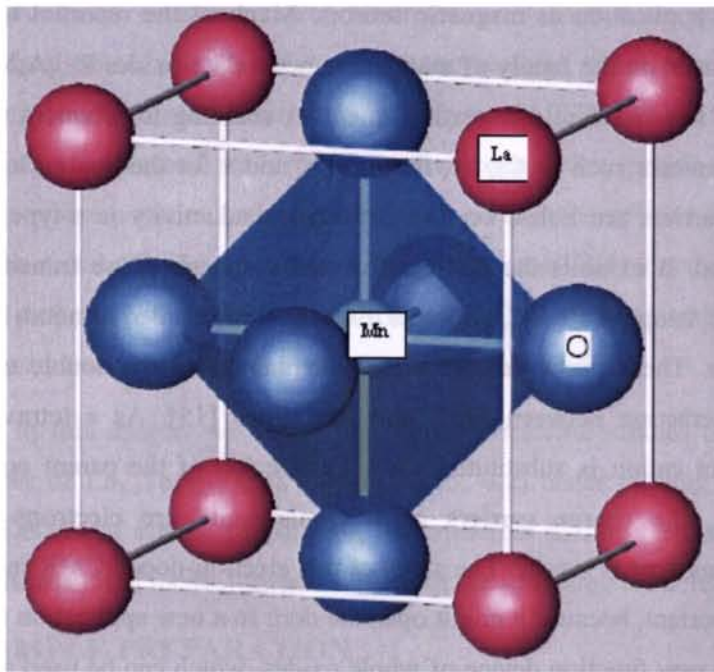
Fig. 1.3. (a) Schematic illustration of electron transport in a multilayer for parallel and antiparallel magnetizations of the successive ferromagnetic layers. The magnetization directions are indicated by the arrows. The solid lines are individual electron trajectories within the two spin channels. (b) Schematic representation of microscopic spin-polarized transport from a ferromagnetic metal (FM1) through a normal metal (NM) and into a second ferromagnetic metal (FM2) for parallel and Antiparallel magnetizations. For antiparallel magnetizations, the transport of up spin electrons from FM1 to FM2 is not allowed as shown by a cross (higher resistance) but for parallel case it is allowed (low resistance).

properties to be examined in a systematic way. Research on the manganites have revealed new phenomena such as colossal [4] and dense granular magnetoresistance [5] and has led to the formulation of important physical concepts such as double exchange [6, 7] and the Jahn-Teller polaron [8,9]. Early research was motivated by a need to develop insulating ferromagnets with a large magnetization for high frequency applications. More recent work has been driven by a desire to understand and exploit the large negative magnetoresistance effects that appear above and below the Curie temperature. The manganites also have potential use as solid electrolytes, catalysts, sensors and novel electronic materials.

Mixed valence oxides are represented by $R_{1-x}A_xMnO_3$ (where R = La, Nd, Pr and A = Ca, Sr, Ba, Pb) have been the materials of intense experimental interest. Besides manganese, many perovskite structure oxides formed with Al, Ga or another 3d element such as Chromium, Iron, Cobalt or Nickel have been subjected to experimentation. The rare earth orthoferrites $RFeO_3$ is one example of a series of perovskite structure oxide. An exhaustive compilation of data on perovskite-structure compounds by Goodenough and Longho [10] was published in a 1970 *Landholdt-Börnstein* volume. The mixed valence oxides can be considered as solid solutions between end members such as $RMnO_3$ and $AMnO_3$, with formal valence state $R^{3-}Mn^{3+}O_3^{2-}$ and $A^{2-}Mn^{4+}O_3^{2-}$ leading to mixed valence compounds such as $(R_{1-x}^{3+}A_x^{2+})(Mn_{1-x}^{3+}Mn_x^{4+})O_3$. The nominal electronic configurations of Mn^{3+} and Mn^{4+} are $3d^4$ and $3d^3$ respectively. Chemically, the system is characterized by the wide range of cations, which can occupy the A-site in the perovskite structure, which may be set at the body centre or the cube corner. The structure of mixed valence oxides can be considered as a cubic close packed array formed of O_3^{2-} anions and large A cations with small B cations in the octahedral interstitial sites as shown in Fig. 5.4. The ideal

cubic structure is distorted by cation size mismatch and the Jahn-Teller effect, where by a distortion of the oxygen octahedron surrounding the B site cation splits the energy levels of a $3d$ ion such as Mn^{3+} , thus lowering the energy. The distorted structures are frequently orthorhombic.

The broad feature of mixture valence perovskites was described by polycrystalline ceramic samples by Jonker and van Santen [11], van Santen and Jonker [12] and Jonker [13] in the late 1940s. They discussed the preparation, crystal structure and magnetic



$$a=b=c=0.388\text{nm}$$

Fig. 5.4: Ideal cubic perovskite structure ABO_3 for the mixed valence perovskites

properties of the $(La_{1-x}Ca_x)MnO_3$ series [11] and gave an account for the electrical conductivity [12]. Similar results were found for the $(La_{1-x}Sr_x)$

MnO₃ and (La_{1-x}Ba_x) MnO₃ series, but the range of solid solutions was limited to $x < 0.7$ or $x < 0.5$ respectively. Magnetoresistance and other transport properties were first described in 1954 by Volger [14] who showed that the magnetoresistance of La_{0.8}Sr_{0.2}MnO₃ is negative with a peak near the Curie temperature.

5.1.3 Electron doped manganese oxides

The colossal magnetoresistance (CMR) effect in manganite perovskites has drawn worldwide attention recently due to their physical properties and potential application as magnetic sensors. Much of the reported work has been focused on the family of manganese perovskite oxides R_{1-x}A_xMnO₃, in which R is a trivalent rare earth element, A standing for divalent (alkaline earth) elements such as Ca, Sr, Ba and Pb, and x for the doping level. The charge carriers are holes, i.e. the electrical conductivity is p-type for this compound. It exhibits the CMR effect and magnetic phase transition at a particular temperature TC , which is always, accompanied a metal–insulator transition. These properties are usually explained by the double exchange (DE) interaction between Mn³⁺ and Mn⁴⁺ ions [15]. As a tetravalent or equivalent cation is substituted for a La site ion of the parent compound LaMnO₃, the charge carriers of this manganite are electrons and its conducting type is n-type. The study of this electron-doped CMR material is very important, because it might open the door to a new application field and lead to a new function device of whole oxides, which can be used at a wide range of temperatures and operated with low noise and high sensitivity. Studies of electron-doped manganites, including R_{1-x}Ce_xMnO₃ in the form of bulk and thin films [16-23] and La_{1-x}Zr_xMnO₃ bulk have been reported [24]. According to a previous work, R_{1-x}Ce_xMnO₃ showed a metal–insulator transition and ferromagnetism associated with large negative magnetoresistance (MR) similar to La_{1-x}Ca_xMnO₃. Ca ions exist in a

tetravalent state and the mixed manganese ions were Mn^{2+} and Mn^{3+} in the system. Moreover, Mitra *et al* [22, 23] have already fabricated a p–n diode successfully by combining $La_{1-x}Ce_xMnO_3$ and $La_{1-x}Ca_xMnO_3$ thin films. Recently, Tan *et.al.* and oleaga *et.al.* have reported an investigation of a new n-type compound $La_{1-x}Te_xMnO_3$ [25, 26].

Thermal properties of $R_{1-x}A_xMnO_3$ is an interesting phenomena to be studied. Oleaga *et.al.* has done the studies in the critical behaviour of $RMnO_3$ (R=La, Pr, Nd) by thermal diffusivity and specific heat measurements close to their magnetic transitions using an ac photopyroelectric calorimeter [26]. Hartmann *et.al.* have done work on the magnetoresistance, specific heat and magnetocaloric effect of equiatomic rare-earth transition-metal magnesium compounds [27]. In this they have performed a systematic study of the resistance and the specific heat as a function of temperature and magnetic field on a series of rare-earth (RE) transition-metal (T) Mg compounds. C.P.Menon *et.al.* have done studies on thermal properties of $LaPbMnO$, $LaSrMnO$, $LaCaMnO$ systems near metal-insulator transition using photo-pyroelectric technique[28].

In this chapter we report the photopyroelectric studies of thermal properties of $La_{1-x}Te_xMnO_3$ ($x= 0, 0.1, 0.15, 0.2$) under varying magnetic fields. Details of sample preparation, experimental details, results obtained and a discussion of the results are outlined in the following sections.

5.2. SAMPLE PREPARATION

Polycrystalline samples of $La_{(1-x)}Te_xMnO_3$ ($x= 0, 0.1, 0.15, 0.2$) were prepared by conventional ceramic techniques. The stoichiometric mixture of high purity. La_2O_3 , TeO_2 , and Mn_3O_4 powders was milled, pressed and pre-heated at 700 °C for 24 h, and then the sample was ground and fired at 900 °C for 12 h. Both the steps mentioned above were processed in flowing argon gas. In the end the sample was sintered at about 930 °C for 24 h in

flowing oxygen gas and then cooled down to room temperature in the off powered furnace. The X-ray diffraction patterns of the samples are taken and they agree with the reported ones [25]. The X-ray diffraction patterns of the samples are shown in Figure 5.5.

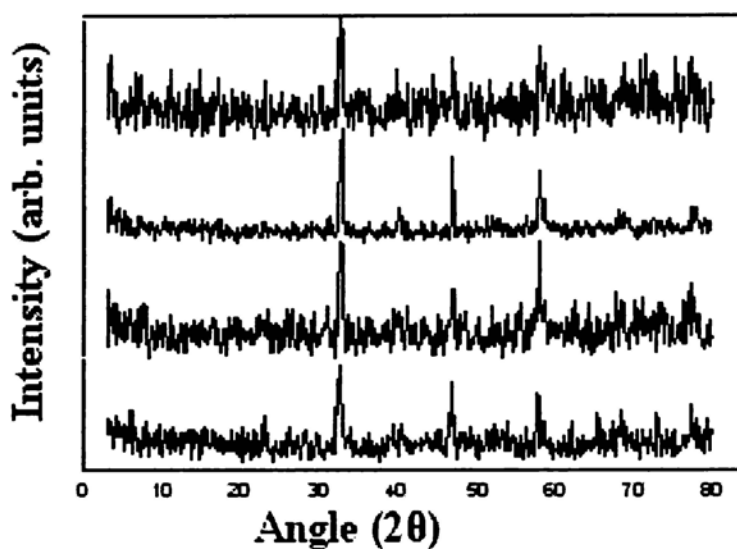


Fig. 5.5 X-ray diffraction pattern $\text{La}_{(1-x)}\text{Te}_x\text{MnO}_3$ ($x= 0, 0.1, 0.15, 0.2$)

5.3 EXPERIMENTAL METHODS AND RESULTS

5.3.1 PPE Measurements with sample in Magnetic field

The photopyroelectric method with varying magnetic field as described in chapter 2 has been used to determine the thermal properties $\text{La}_x\text{Te}_{x-1}\text{MnO}_3$. For this measurement the sample dimensions should be such that the sample,

the pyroelectric detector and the backing material should be thermally thick during the whole measurement. The sample is illuminated with an intensity-modulated beam of light, which gives rise to periodic temperature variations in the sample by optical absorption. The thermal waves so generated propagate through the sample and are detected with a pyroelectric detector. Modulation frequency is kept above 30Hz in all our experiments to ensure that the detector, the sample and the backing medium are all thermally thick during measurements. Block diagram of the experimental setup and other details are already given in Chapter 2 of the thesis. The sample cell as such is kept between the pole pieces of the electromagnet whose field can be varied by varying current. The temperature of the setup also can be varied by pouring liquid nitrogen into the sample chamber and then temperature can be controlled using a PID temperature controller (Lakeshore Cryotronics Model. DRC 82 C). Keeping temperature constant above and below the transition temperature, magnetic field is varied and the corresponding amplitude and phase of the signal is taken from the lock-in amplifier. From this we can calculate the thermal diffusivity and effusivity of the sample for that particular temperature and field. And the specific heat capacity and thermal conductivity of the sample are evaluated using the equations

$$k = e [\alpha]^{1/2} \quad (1)$$

$$c_p = e/[\rho[\alpha]^{1/2}] \quad (2)$$

The calibration of the experimental set up has been done with known samples prior to carrying out the measurements.

The measurements have been done at temperatures between 120 K and 300K for the sample with $x=0$, and 200 K and 300K for samples with $x= 0.1, 0.15, 0.2$ at temperature intervals of 2 K normally and at intervals of 1 K at temperatures in the vicinity of the two transition points. At each measurement temperature, the sample has been kept at

constant temperature during measurements. From the frequency dependence of the pyroelectric amplitudes and phases, the thermal diffusivity and effusivity of the sample along the above axes have been determined at each temperature. The temperature variations of these parameters for all the four samples are shown in Fig.5.6, Fig.5.7, Fig.5.8, Fig.5.9, Fig.5.10, Fig.5.11, and Fig.5.12 respectively. From the diffusivity and effusivity values, the corresponding values of thermal conductivity and specific heat capacity have been computed and plotted in Figures 5.13, 5.14, 5.15, 5.16, 5.17, 5.18 and 5.19 respectively. These parameters are also calculated by keeping the temperature 5K above and 5K below the transition temperature for every sample. These plots are also shown in figures 1.20, 5.21, 5.22, 5.24, 5.25, 5.26, 5.27, 5.28, 5.29, 5.30 and 5.31. For the sample with $x=0.2$ these measurements haven't been done since it does not exhibit any transition or anomaly.

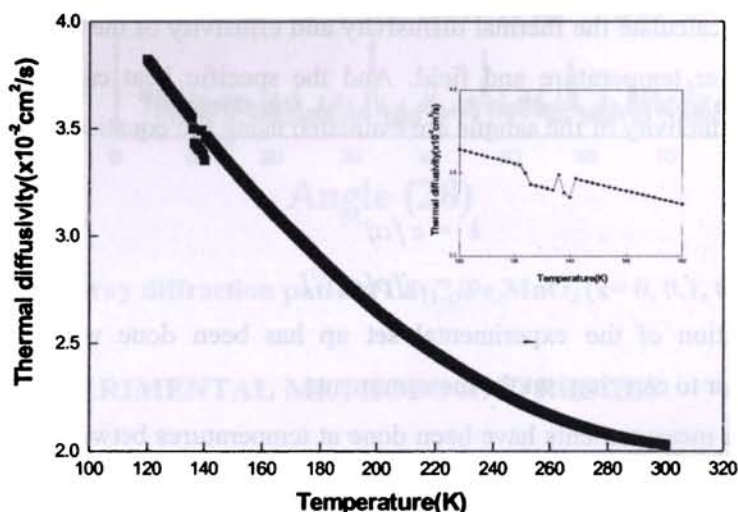


Fig.5. 6: Plot showing the variation of thermal diffusivity of LaMnO_3 with temperature. The inset shows variation in the vicinity of the transition

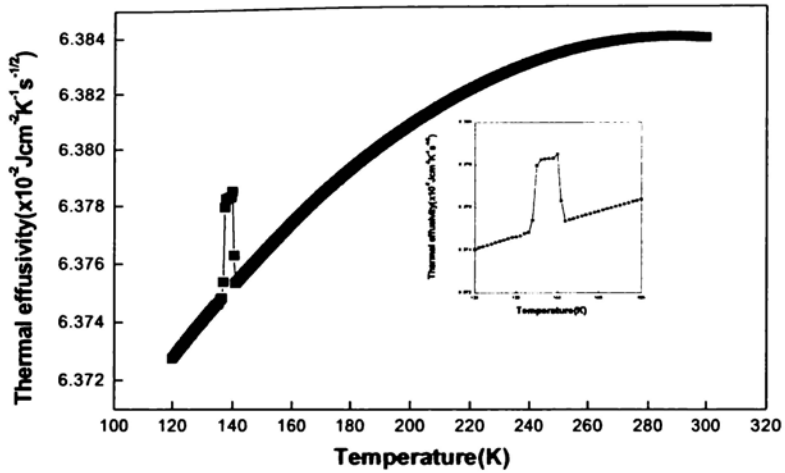


Fig.5. 7: Plot showing the variation of thermal effusivity of LaMnO_3 with temperature. The inset shows variation in the vicinity of the transition

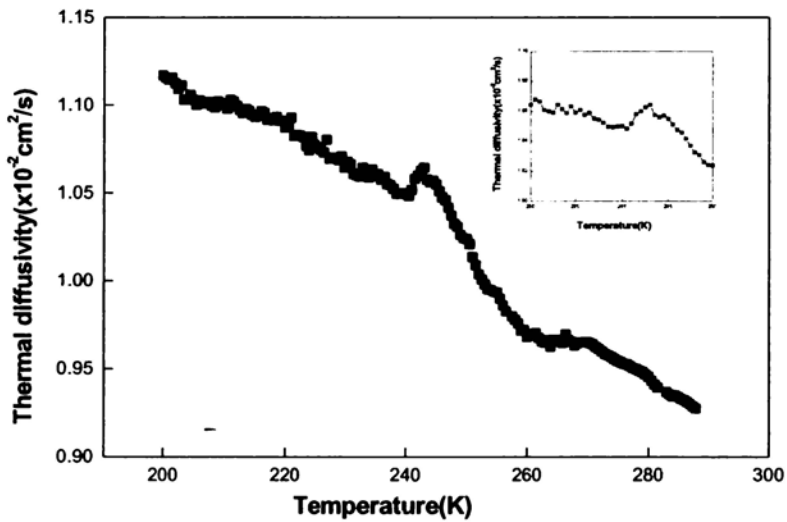


Fig.5.8: Plot showing the variation of thermal diffusivity of $\text{La}_9\text{Mn}_{0.1}\text{O}_3$ with temperature. The inset shows variation in the vicinity of the transition

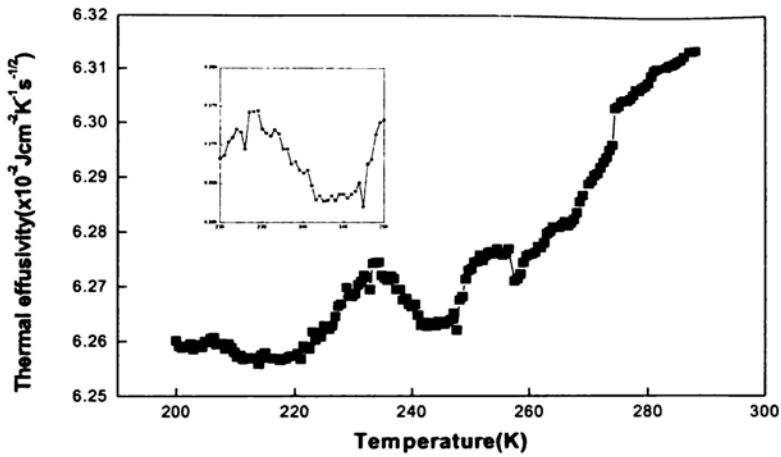


Fig.5.9: Plot showing the variation of thermal effusivity of $\text{La}_{0.9}\text{Mn}_{0.1}\text{O}_3$ with temperature. The inset shows variation in the vicinity of the transition

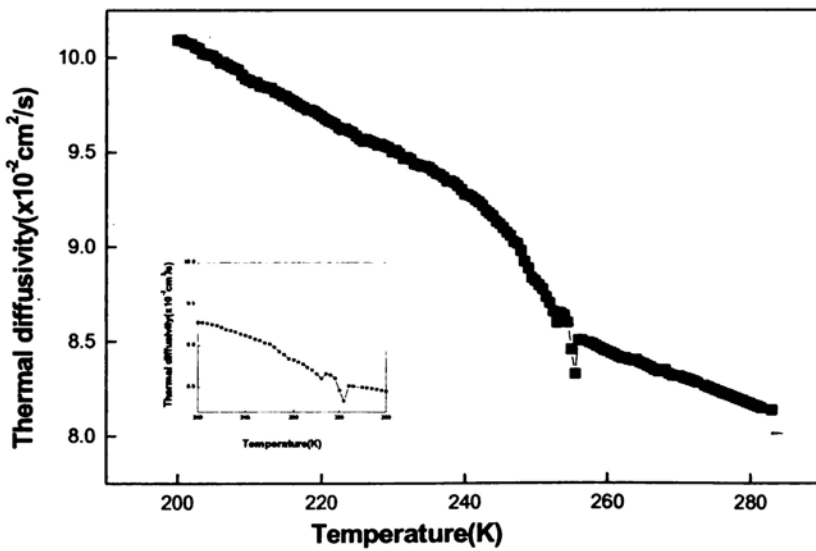


Fig.5.10: Plot showing the variation of thermal diffusivity of $\text{La}_{0.85}\text{Mn}_{0.15}\text{O}_3$ with temperature. The inset shows variation in the vicinity of the transition.

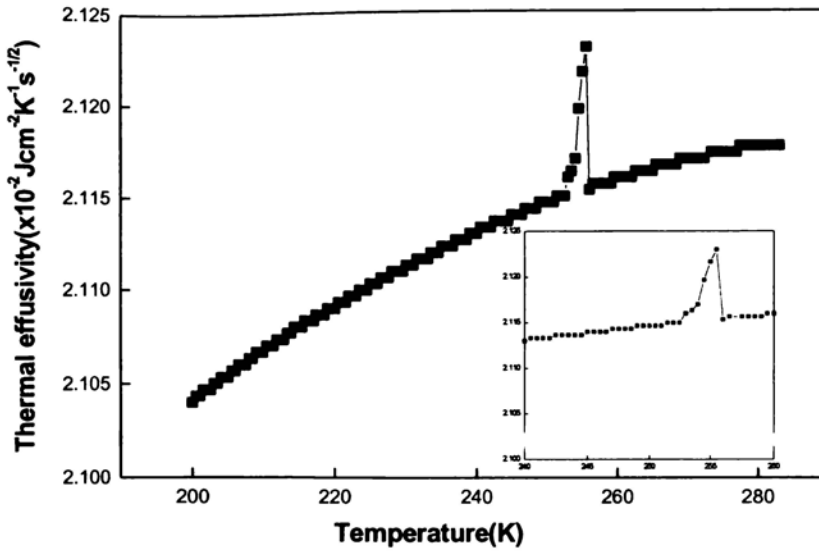


Fig.5.11: Plot showing the variation of thermal effusivity of $\text{La}_{0.85}\text{Mn}_{0.15}\text{O}_3$ with temperature. The inset shows variation in the vicinity of the transition

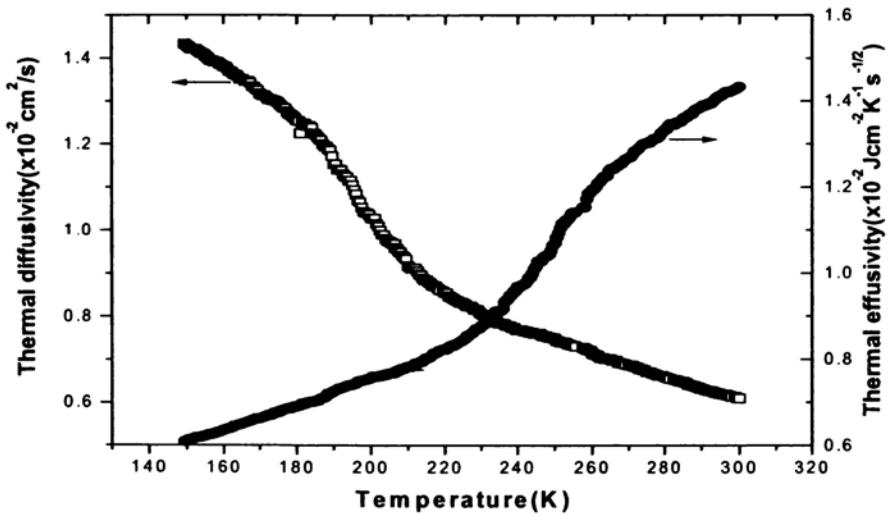


Fig.5.12: Plot showing the variation of thermal diffusivity and thermal effusivity of $\text{La}_{0.8}\text{Te}_{0.2}\text{MnO}_3$. The inset shows variation in the vicinity of the transition.

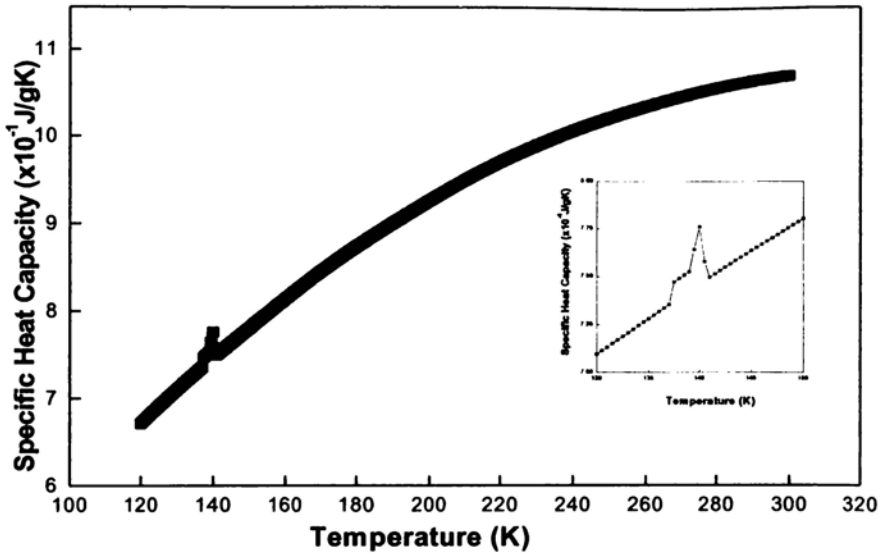


Fig.5. 13: Plot showing the variation of specific heat capacity of LaMnO₃ with temperature. The inset shows variation in the vicinity of the transition

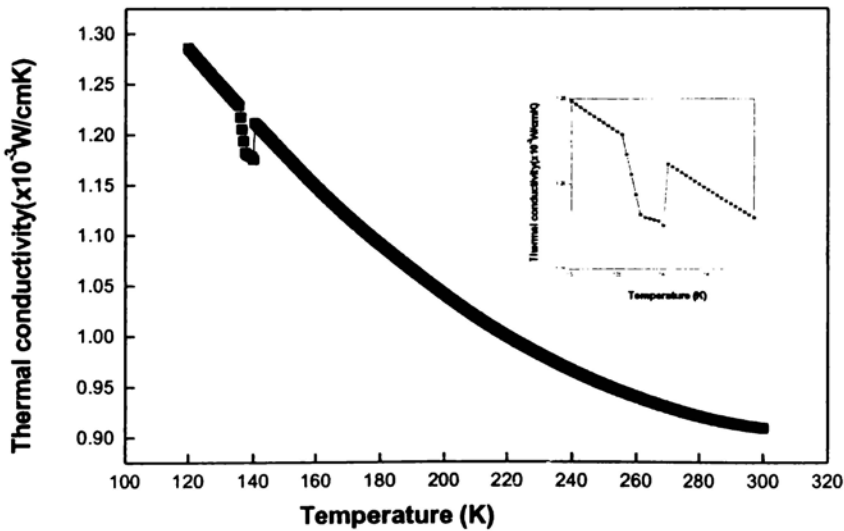


Fig.5. 14: Plot showing the variation of thermal conductivity of LaMnO₃ with temperature. The inset shows variation in the vicinity of the transition

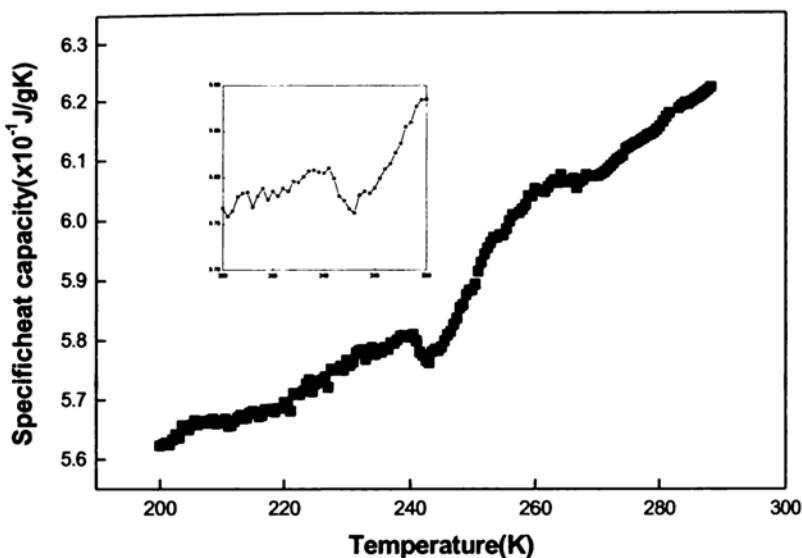


Fig.5.15: Plot showing the variation of specific heat capacity of $\text{La}_{0.9}\text{Mn}_{0.1}\text{O}_3$ with temperature. The inset shows variation in the vicinity of the transition

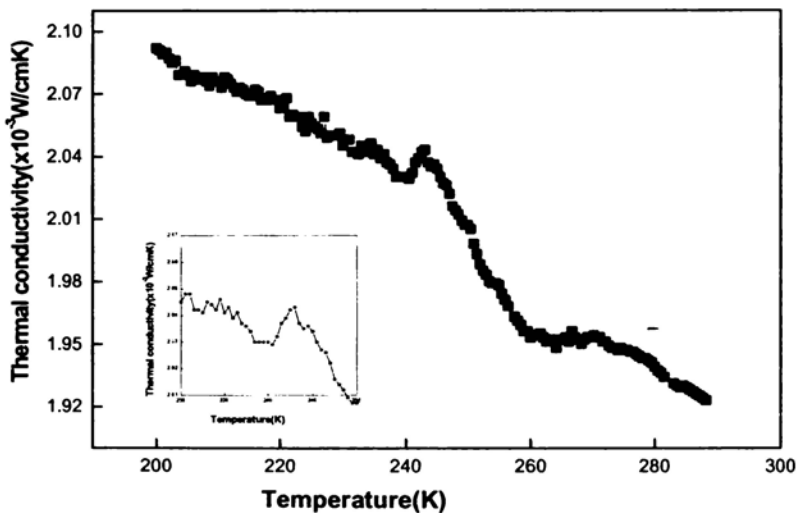


Fig.5.16: Plot showing the variation of Thermal conductivity of $\text{La}_{0.9}\text{Mn}_{0.1}\text{O}_3$ with temperature. The inset shows variation in the vicinity of the transition

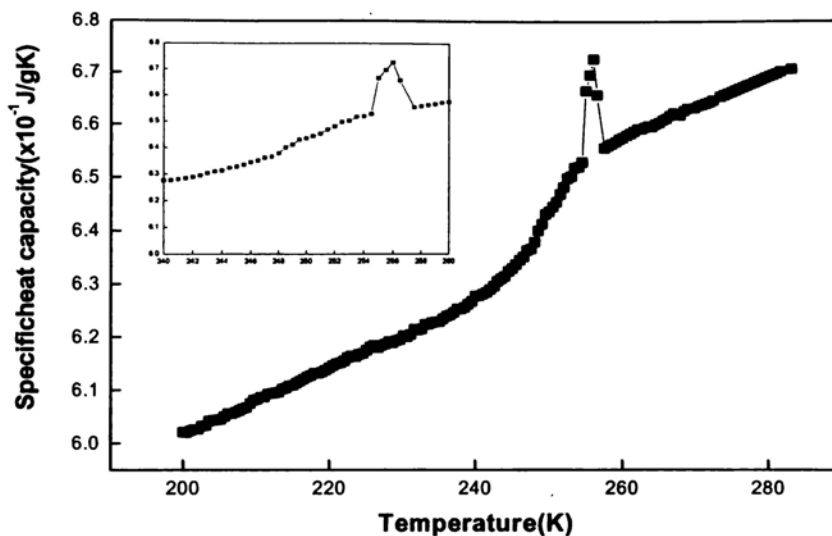


Fig.5.17: Plot showing the variation of specific heat capacity of $\text{La}_{0.85}\text{Mn}_{0.15}\text{O}_3$ with temperature. The inset shows variation in the vicinity of the transition

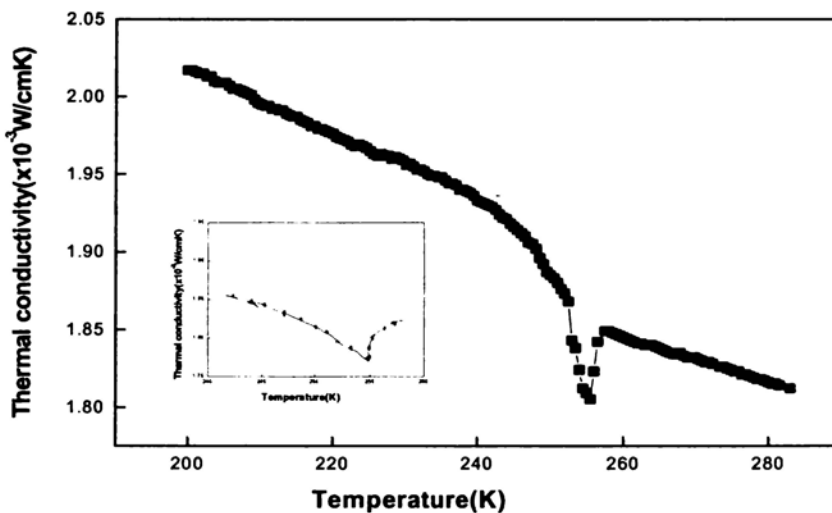


Fig.5.18: Plot showing the variation of thermal conductivity of $\text{La}_{0.85}\text{Mn}_{0.15}\text{O}_3$ with temperature. The inset shows variation in the vicinity of the transition

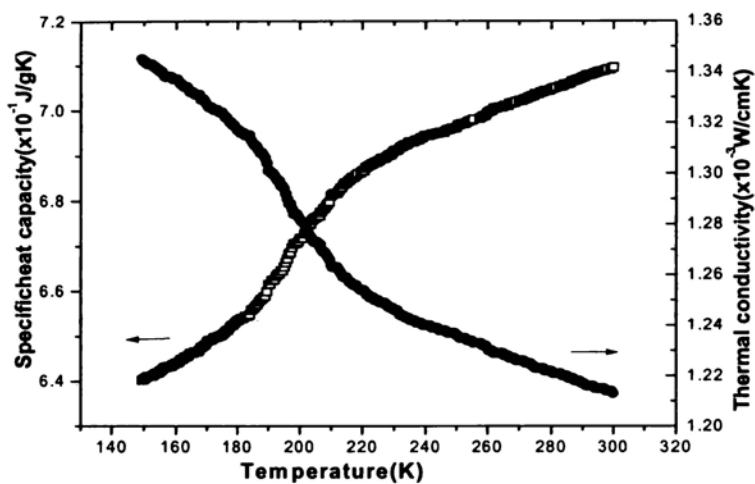


Fig.5.19: Plot showing the variation of specific heat capacity and thermal conductivity of $\text{La}_{0.8}\text{Te}_{0.2}\text{MnO}_3$ with temperature

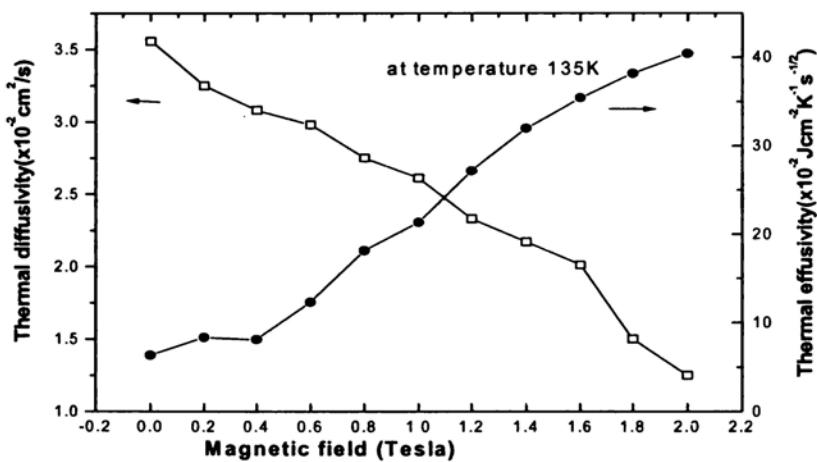


Fig.5.20: Plots showing the variation of thermal diffusivity and thermal effusivity of LaMnO_3 with magnetic field at 135K

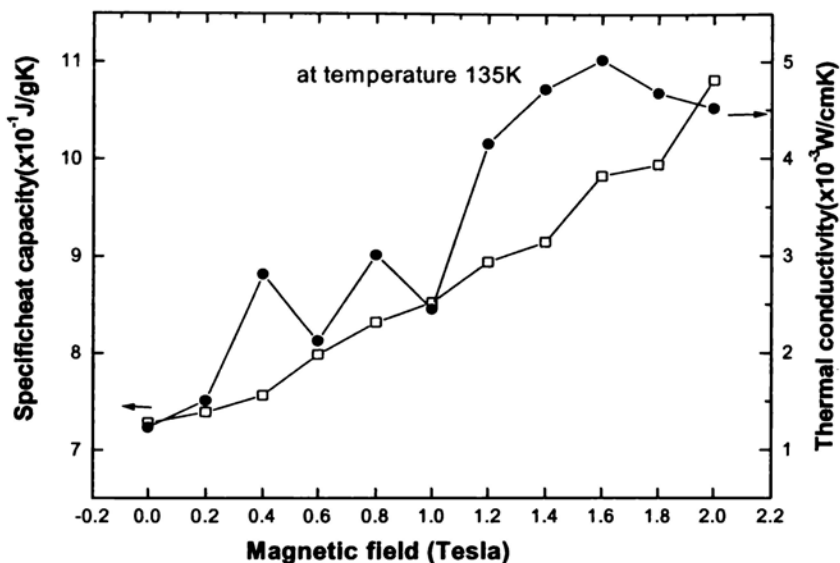


Fig.5.21: Plots showing the variation of specific heat capacity and thermal conductivity of LaMnO_3 with magnetic field at 135K

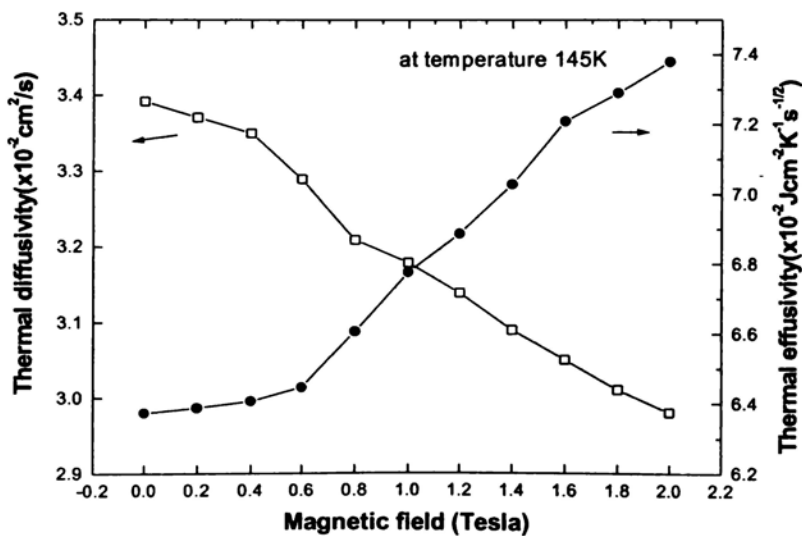


Fig.5.22: Plots showing the variation of thermal diffusivity and thermal effusivity of LaMnO_3 with magnetic field at 145K

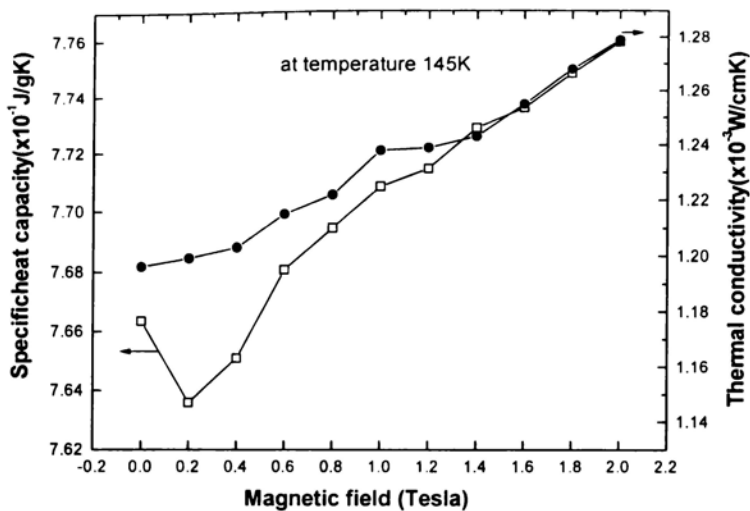


Fig.5.23: Plots showing the variation of specific heat capacity and thermal conductivity of LaMnO_3 with magnetic field at 145K

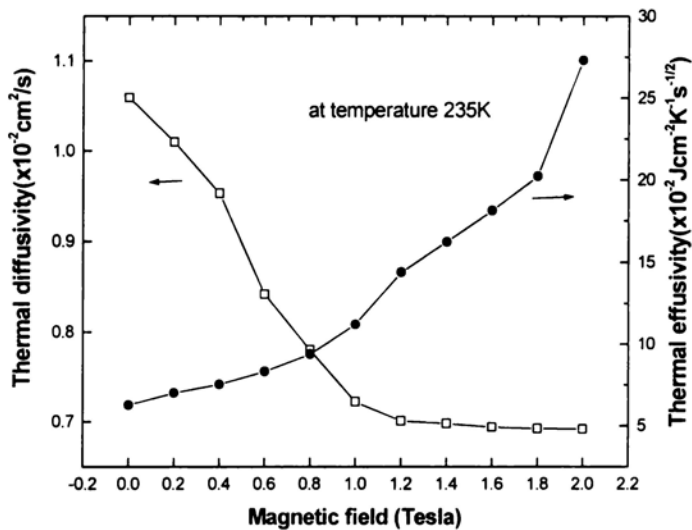


Fig.5.24: Plots showing the variation of thermal diffusivity and thermal effusivity of $\text{La}_{0.9}\text{Te}_{0.1}\text{MnO}_3$ with magnetic field at 235K

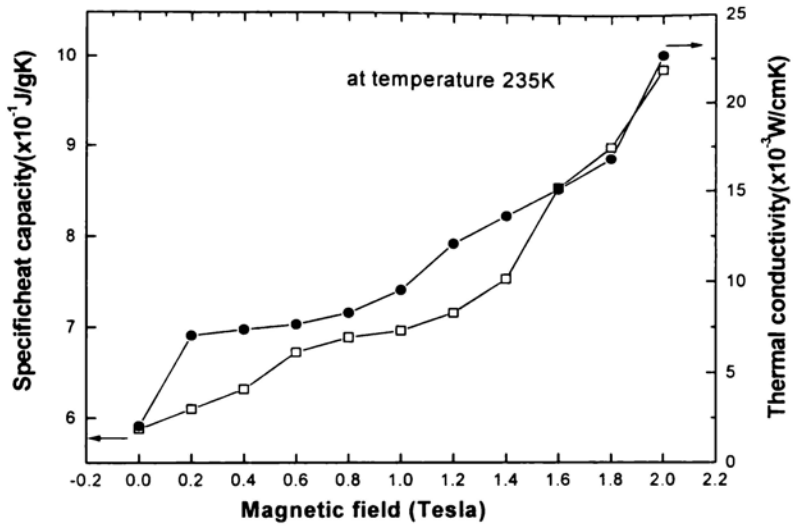


Fig.5.25: Plots showing the variation of specific heat capacity and thermal conductivity of $\text{La}_{0.9}\text{Te}_{0.1}\text{MnO}_3$ with magnetic field at 235K

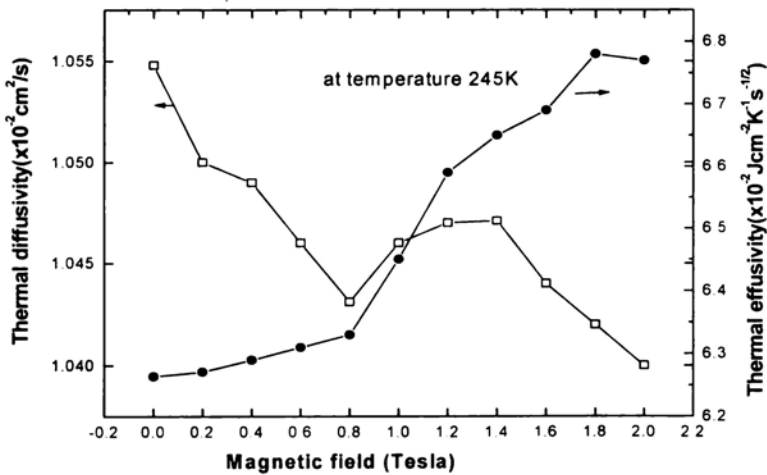


Fig.5.26 Plots showing the variation of thermal diffusivity and thermal effusivity of $\text{La}_{0.9}\text{Te}_{0.1}\text{MnO}_3$ with magnetic field at 245K

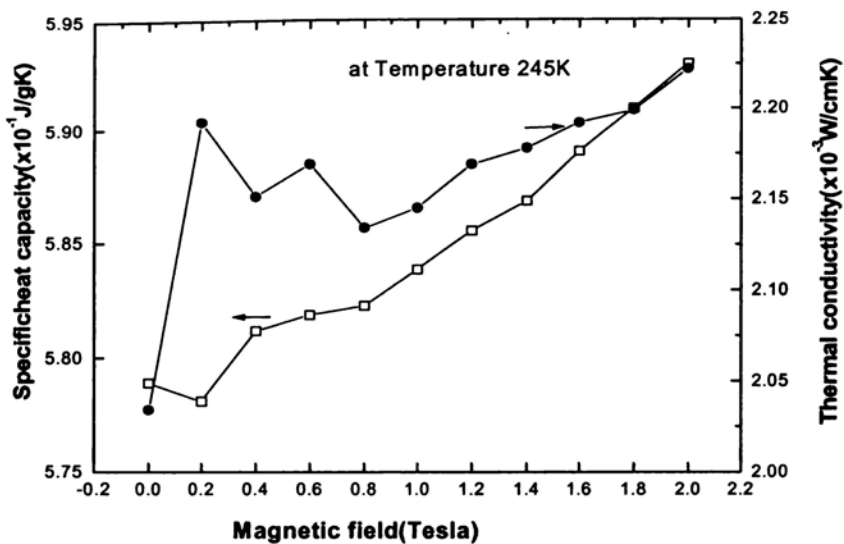


Fig.5.27: Plots showing the variation of specific heat capacity and thermal conductivity of $\text{La}_{0.9}\text{Te}_{0.1}\text{MnO}_3$ with magnetic field at 245K

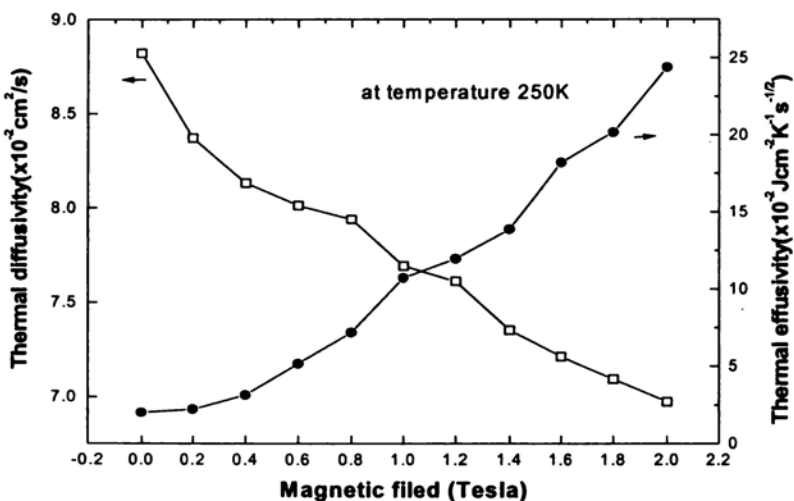


Fig.5.28: Plots showing the variation of thermal diffusivity and thermal effusivity of $\text{La}_{0.85}\text{Te}_{0.15}\text{MnO}_3$ with magnetic field at 250K

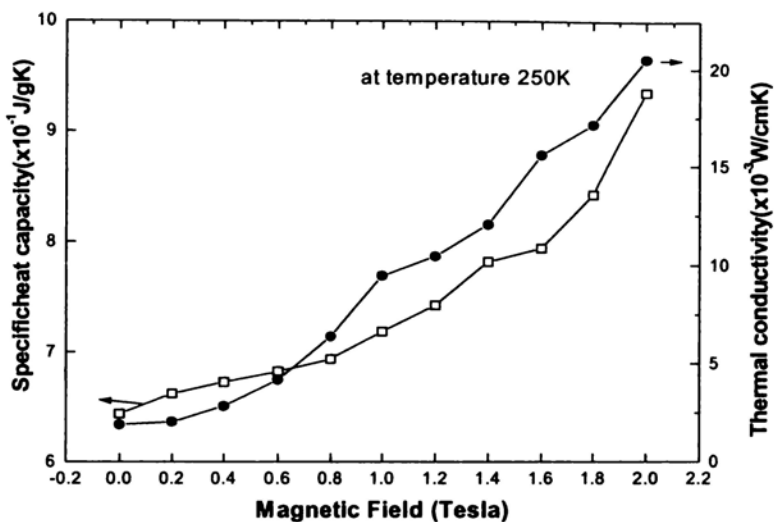


Fig.5.29: Plots showing the variation of specific heat capacity and thermal conductivity of $\text{La}_{0.85}\text{Te}_{0.15}\text{MnO}_3$ with magnetic field at 250K

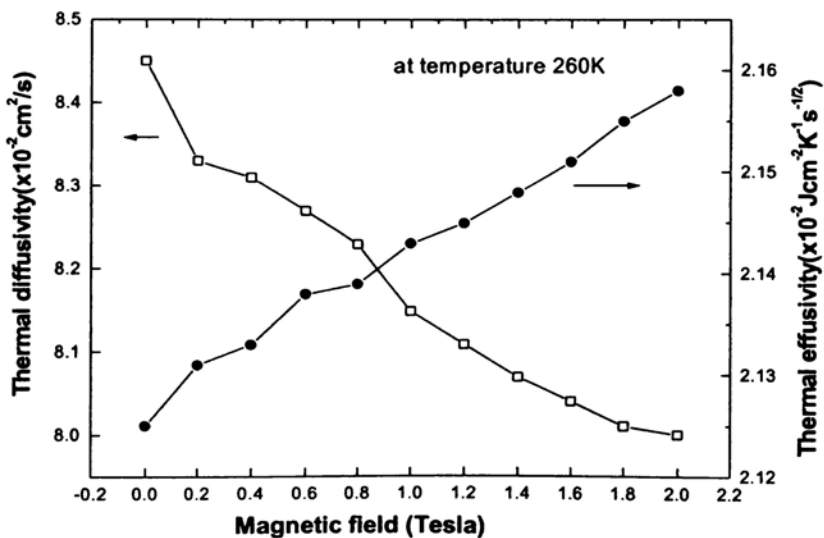


Fig.5.30: Plots showing the variation of thermal diffusivity and thermal effusivity of $\text{La}_{0.85}\text{Te}_{0.15}\text{MnO}_3$ with magnetic field at 260K

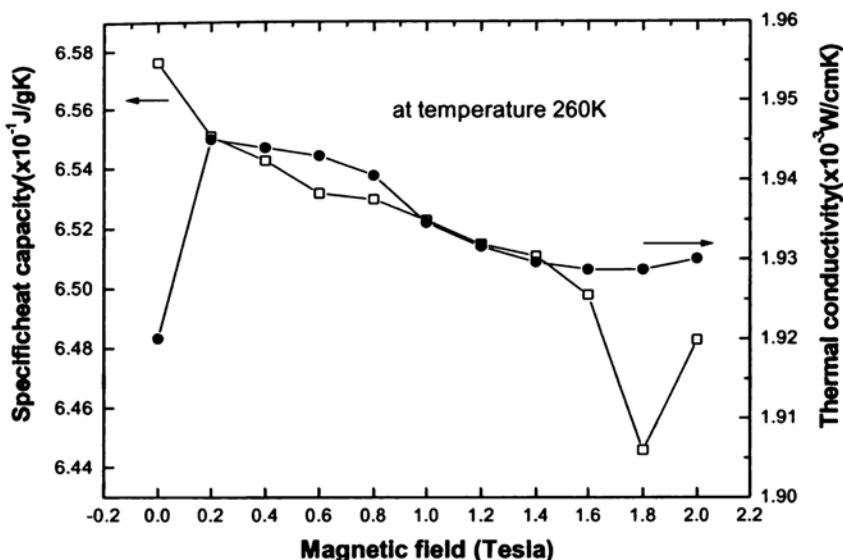


Fig.5.31: Plots showing the variation of specific heat capacity and thermal conductivity of $\text{La}_{0.85}\text{Te}_{0.15}\text{MnO}_3$ with magnetic field at 260K

5.3.2 DSC measurements

DSC curves of $\text{La}_x\text{Te}_{(1-x)}\text{MnO}_3$ crystals have been recorded following the standard procedures. The DSC curve of these samples during heating cycle is shown in Figures 5.32, 5.33, 5.34 and 5.35 respectively. The transitions of each sample can be clearly seen in the DSC plots.

The DSC plots (all recorded along heating cycle) indicate that the transitions are exothermic. Transitions are clearly visible in LaMnO_3 , $\text{La}_{0.9}\text{Te}_{0.1}\text{MnO}_3$, $\text{La}_{0.85}\text{Te}_{0.15}\text{MnO}_3$ while one can notice a small kink at 253.5K for $\text{La}_{0.8}\text{Te}_{0.2}\text{MnO}_3$ which is indicative of a transition at this temperature for this sample. However, since the transition is extremely weak, it does not get reflected in thermal conductivity or specific heat

capacity. This sample virtually does not exhibit any magnetic transition as the temperature is varied.

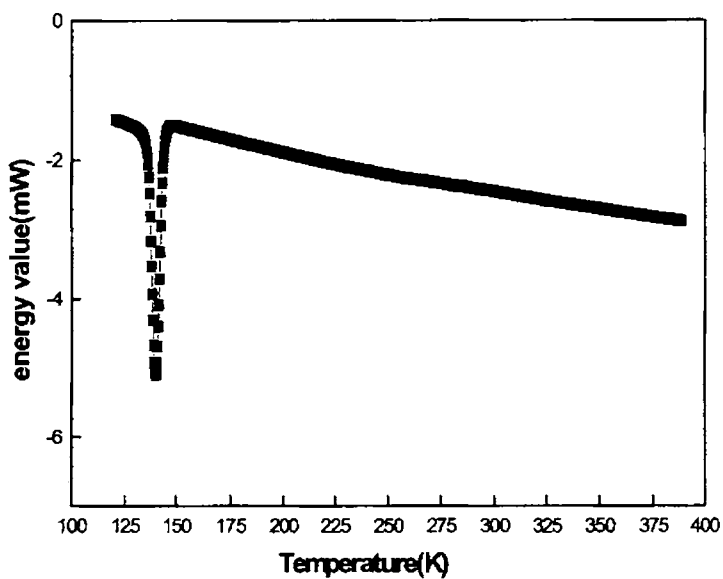


Fig. 5.32: DSC plot of LaMnO₃

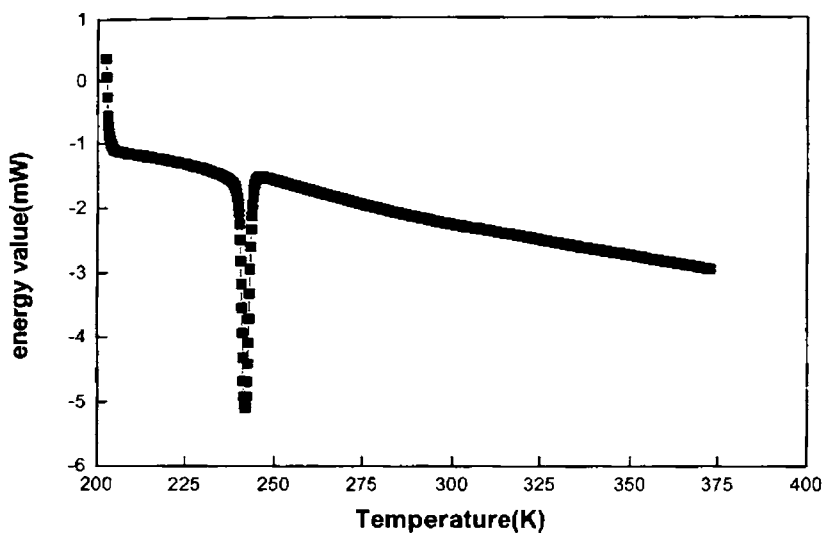


Fig. 5.33: DSC plot of $\text{La}_{0.9}\text{Te}_{0.1}\text{MnO}_3$

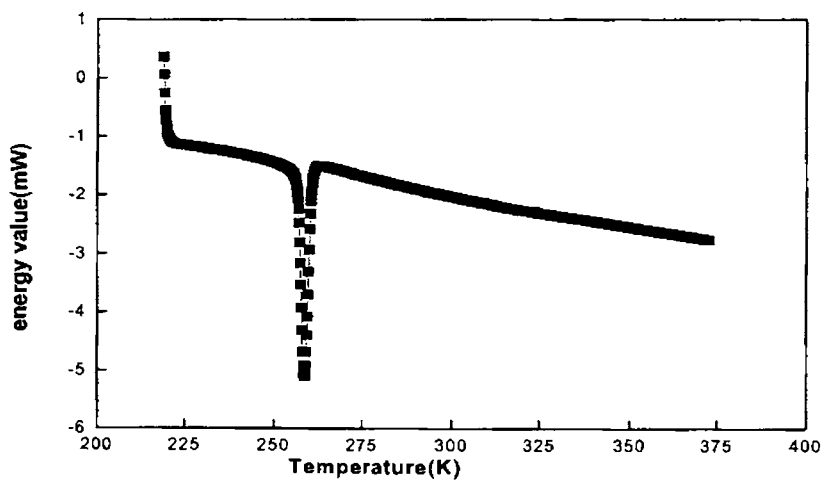


Fig. 5.34: DSC plot of $\text{La}_{0.85}\text{Te}_{0.15}\text{MnO}_3$

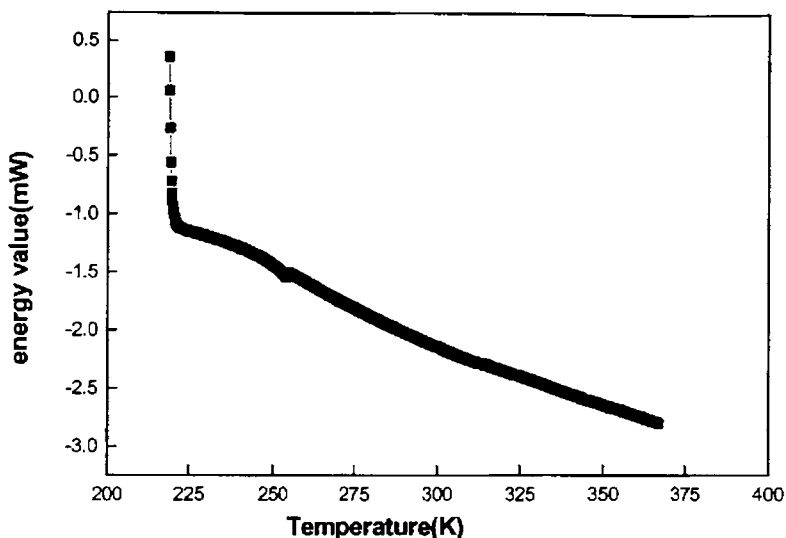


Fig. 5.35: DSC plot of La_{0.8}Te_{0.2}MnO₃

5.4 DISCUSSION OF RESULTS

5.4.1 X-Ray diffraction

The plots of X-ray diffraction patterns for these samples are shown in Fig. 5.5. As we understand, La_(1-x)Te_xMnO₃ is an electron dominant system and hence the conductivity in this may be electronic in nature. It is known that the radius of the Te⁴⁺ is about 0.097nm and that of La³⁺ is 0.1216nm. The partial substitution of Te⁴⁺ ions with La³⁺ ions will cause cell constriction and a distortion of the lattice which is evident from the XRD pattern. As can be seen from Fig. 5.5 the compound has a rhombohedral structure with space group R⁻3C.

5.4.2 PPE Measurements with sample in Magnetic field

As can be seen from figures 5.6, 5.7, 5.14 and 5.15 it is clear that the sample undergoes a phase transition at 140K which is an antiferromagnetic to paramagnetic one, with sample being an electrical insulator in both the phases. Thermal diffusivity of the sample decreases as the temperature is raised due to the reduction in phonon mean free path by phonon-phonon, electron-phonon and phonon-defect scatterings. At $T > T_c$, the thermal diffusivity decreases smoothly. The presence of the magnetic transition is to superimpose a dip in the thermal diffusivity curve, creating an analogous effect as it has on the specific heat curves. Thermal conductivity also decreases with temperature while changing from the antiferromagnetic to the paramagnetic phase. These results are in agreement with experimental results obtained by other authors [26, 29, 30].

From the thermal diffusivity, thermal effusivity, specific heat capacity and thermal conductivity plots of $\text{La}_{0.9}\text{Te}_{0.1}\text{MnO}_3$ and $\text{La}_{0.85}\text{Te}_{0.15}\text{MnO}_3$ it is clear that they undergo para to ferromagnetic transition at around 240K and 255K respectively. The increase in T_c with increase in Tellurium concentration can be attributed to the strengthening of the interactions due to lattice distortions and bond angle increases. These interactions strengthen the ferromagnetic coupling between Mn ions.

The variations of the four thermal parameters with magnetic field above and below the transition temperatures are shown in the figures from 5.20 to 5.31. It is clear from the figures that variation of all four parameters above the transition temperature is smaller than those below it. The specific heat capacity as well as thermal conductivity are found to increase with increasing magnetic field for the three samples above and below the transition temperatures.

In the perovskite manganites, the five-fold-degenerate d orbital of the manganese ion splits into a three-fold-degenerate t_{2g} orbital and a two-fold-degenerate e_g orbital in the oxygen octahedra due to the crystal field [31]. In addition, distortion of the oxygen octahedra can split the two-fold-degenerate e_g level. In the hole-doped samples the electrons in the e_g orbital get delocalized through Zener double exchange via an effective transfer integral t giving rise to electrical conductivity and ferromagnetism.

As can be seen from figures the thermal diffusivities of the samples show an anomalous decrease at the para-ferromagnetic transition temperature (Neel temperature). The thermal effusivity shows a corresponding enhancement at these temperatures. The sample $\text{La}_{0.8}\text{Te}_{0.2}\text{MnO}_3$ does not exhibit any anomaly as this sample does not undergo any magnetic transition. In all cases the thermal diffusivity decreases and thermal effusivity increases with temperature, with anomalies exhibited at the Neel temperature.

Figures 5.36-5.38 show the plots of the variation of $1/\alpha$ with Δ , where α is the thermal diffusivity and $\Delta = (T-T_N)/T_N$ where T is the temperature (in K) and T_N is the Neel temperature. In these figures it can be seen that $1/\alpha$ exhibits a λ type variation at T_N indication that these transitions are second-order in nature.

As is evident from figures 5.13 to 5.19, the thermal conductivities of all samples decrease monotonically with temperature and specific heat capacity increases with temperature. This is the general behavior exhibited by all the solids. This variation of thermal conductivity can be explained in terms of the scattering of thermal waves (phonons) by lattice phonons or electrons as well as by lattice defects and imperfections. As temperature rises the mean free path decreases resulting in a corresponding increase in the scattering rates, which is responsible for the

decrease in thermal conductivity as temperature increases .This variation follows the well known relation

$$k = 1/3 c v l$$

Where c is the heat capacity, v is the average phonon velocity and l is the mean free path. At the magnetic transition temperatures, the samples undergo lattice distortion resulting in an enhancement in scattering rates (or decrease in mean free path), which results in an anomalous decrease in thermal conductivity at these temperature. For the sample which does not undergo the magnetic transition, the decrease in thermal conductivity with temperature is smooth (See figure 5.19).

For all the samples the specific heat capacity increases with temperature as is true for all solids. Again, at the magnetic transition temperatures, the heat capacity shows an anomalous increase, which can be considered as due to the entropy of the transition. Plots showing the variation of c with Δ for the three samples that exhibit para-ferromagnetic transition are shown in Figures 5.39-5.41. Again, sample with no magnetic transition does not show any anomaly in the specific heat curve. The variations of c with Δ also show a λ -type behavior indicating that the phase transition is of second order.

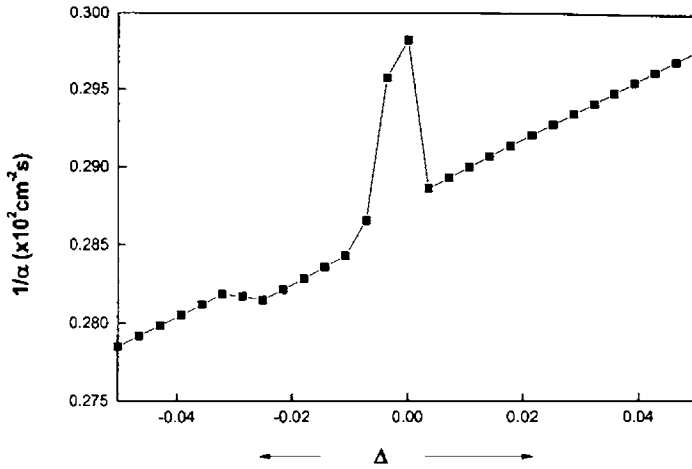


Fig.5.36: Plots showing of the variation of $1/\alpha$ with Δ for LaMnO_3

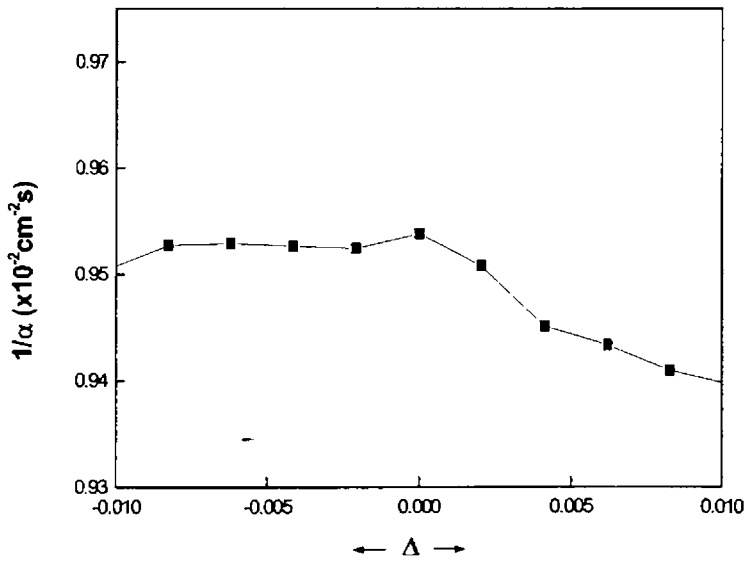


Fig.5.37: Plots showing of the variation of $1/\alpha$ with Δ for $\text{La}_{0.9}\text{Te}_{0.1}\text{MnO}_3$

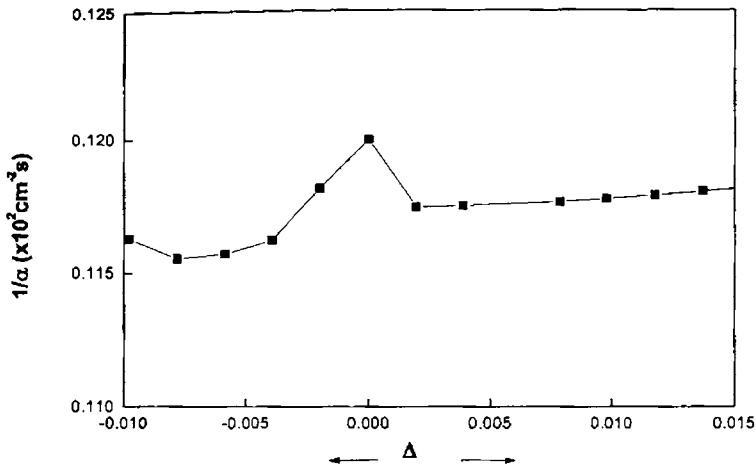


Fig.5.38: Plots showing of the variation of $1/\alpha$ with Δ for $\text{La}_{0.85}\text{Te}_{0.15}\text{MnO}_3$

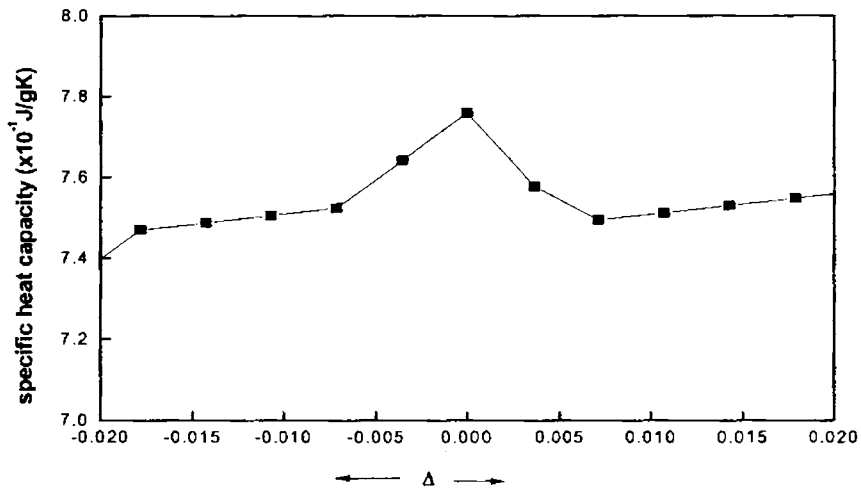


Fig.5.39: Plots showing of the variation of C_p with Δ for LaMnO_3

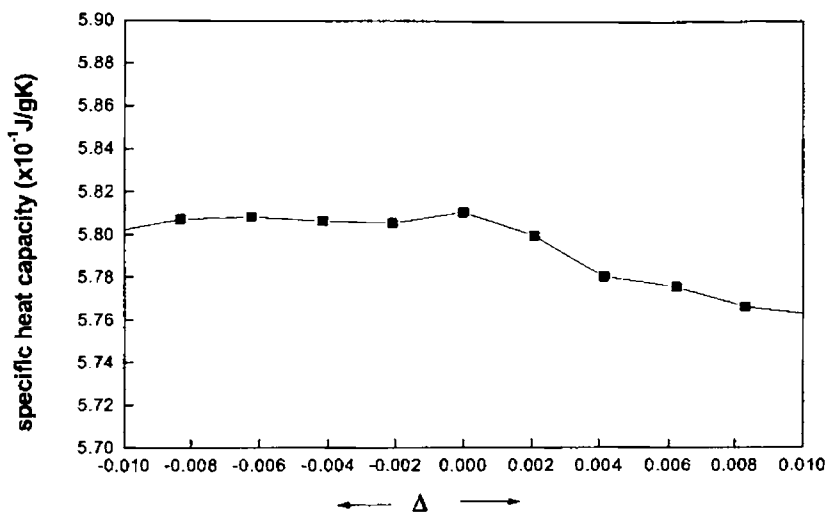


Fig.5.40: Plots showing of the variation of Cp with Δ for La_{0.9}Te_{0.1}MnO₃

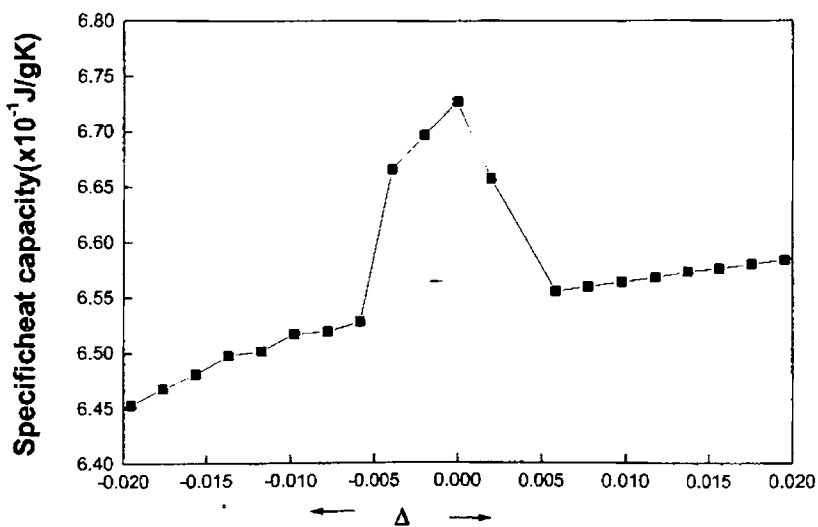


Fig.5.41: Plots showing of the variation of Cp with Δ for La_{0.85}Te_{0.15}MnO₃

Pure LaMnO_3 exhibits magnetic transition around 140K. In order to investigate the variations of thermal properties with magnetic field in the paramagnetic and antiferromagnetic states of this material, we have carried out these measurements at 135K as well as at 145K. The temperatures were kept constant, and magnetic fields applied to the sample were varied. These results for pure LaMnO_3 are shown in figures 5.20 - 5.23. At 145K as the magnetic field increase from 0T to 2T, the thermal diffusivity decreases from $3.4 \times 10^{-2} \text{cm}^2/\text{s}$ to $3.0 \times 10^{-2} \text{cm}^2/\text{s}$ resulting in a percentage change of about 13%. The corresponding changes in thermal diffusivity at 135K are about 64%. If we look at the corresponding variations in thermal conductivity, it can be seen that thermal conductivity increases by only about 6% at 145K for a magnetic field increase by 2T, whereas the corresponding increase in thermal conductivity is about 75% at 135K. At both these temperatures, the heat capacity increases with magnetic field, but the percentage increases in much more at 135K (nearly 33%) compared to the corresponding increase at 145K (nearly 2%). These results are similar for Tellurium doped samples (See Figures 5.25, 5.27, 5.29 and 5.31).

So, we can see that in the ferromagnetic phase of these samples, the thermal conductivity as well as specific heat increase significantly with externally applied magnetic field. The significant increase in thermal conductivity with magnetic field in the ferromagnetic phase can qualitatively be explained in terms of the alignment of the spins and the corresponding decrease in thermal wave scattering. The corresponding spin ordering that sets in decreases the entropy of the system resulting in a corresponding increase in specific heat of the system. These phenomena are being explained quantitatively in terms of Double Exchange model and Jahn-Teller distortion effects associated with colossal magnetoresistance phenomenon in perovskite manganites.

REFERENCE

1. W Thomson, *Proceedings of the Royal Society of London*, **8**, 546 (1857).
2. M. N. Baibich, J. M. Broto, A. Fert, F. Nguyen Van Dau, and F. Petroff, *Phys. Rev. Lett.*, **61**, 2472 (1988).
3. G. Binasch, P. Grünberg, F. Saurenbach, and W. Zinn., *Phys. Rev. B*, **39**, 4828 (1989).
4. S. Jin, T. H. Tiefel, M. Mc Cormack, R. A. Fastnacht, R. Ramesh, L. H. Chen, *Science*, **264**, 413 (1994).
5. H. Y. Hwang, S. W. Cheong, N. P. Ong and B. Batlogg, *Phys. Rev. Lett.*, **77**, 2041(1996).
6. C. Zener, *Phys. Rev.*, **81**, 440 (1951).
7. C. Zener, *Phys. Rev.*, **82**, 403 (1951).
8. E. Pollert, S. Krupicka, E. Kuzwiczova, *J. Phys. Chem. Solids*, **43**, 1137 (1982).
9. G. Zhao, K. Conder, H. Keller and K. A. Muller, *Nature*, **381**, 676 (1996).
10. J. B. Goodenough and J. Longho, *Landholdt-Boörnstein*, Vol. **4a** (Springer, Berlin 1970).
11. G. Jonker and J. H. van Santen, *Physica*, **16**, 337 (1950).
12. J. H. van Santen, C. H. Jonker, *Physica*, **16**, 599 (1950).
13. G. H. Jonker, *Physica*, **22**, 707 (1956).
14. J. Volger, *Physica*, **20**, 49 (1954).
15. P. G De Gennes, *Phys.Rev.***118**, 141 (1960).
16. A. Maignan, C. Martin and B. Raveau, *Z.Phys.B*, **102**, 19 (1997).
17. S. Das and P. Mandal, *Z. Phys.B.*, **104**, 7 (1997)
18. P. Mandal and S. Das, *Phys. Rev. B* **56**, 15073 (1997).
19. J. R. Gebharbt, S. Roy and N. Ali, *J. Appl. Phys.*, **85**, 5390 (1999).

20. P. Raychaudhuri, S. Mukherjee, A.K.Nigam , J. John, U. D. Vaisnav, R. Pinto and P. Mandal , *J. Appl. Phys* **86**, 5718 (1999).
21. C. Mitra, P. Raychaudhuri, J. John, S.K Dhar, A. K. Nigam and R. Pinto, *J. Appl. Phys.*, **89**, 524 (2001)
22. C. Mitra, P. Raychaudhuri, G. Kobernik, K. Dorr, Muller K-H, L Schultz and R. Pinto, *Appl. Phys. Lett.*, **79**, 2408 (2001)
23. C. Mitra, G. Kobernik, K. Dorr, Muller K-H, L Schultz, P. Raychaudhuri , R. Pinto and E. Wieser , *J. Appl. Phys.*, **91**, 7715 (2002)
24. S. Roy and N. Ali, *J. Appl. Phys.*, **89**, 7425 (2001).
25. G. T. Tan, S. Y. Dai, P. Duan, Y. L. Zhou , H. B. Lu and Z.H Chen, *J. Appl. Phys.*, **93**, 5480 (2003)
26. A. Oleaga, A. Salazar, B. Prabhakaran and A. T. Boothroyd, *J. Phys.; Condens.Matt.*, **17**, 6729 (2005)
27. H. Hartmann, K. Berggold, S. Jodlauk, I. Klassen, K. Kordonis, T. Fickenscher, R. Poptgen, A. Freimuth and T. Lorenz, *J.Phys.; Condens.Matt.*, **17**, 7731 (2005)
28. C. Preethy Menon, M. T. Sebastian, J. Philip and R.W. Schwartz, *J. Appl. Phys.***94**,3206 (2003)
29. J. S. Zhou and J. B. Goodenough, *Phy. Rev. B*, **64**, 024421 (2001)
30. J. L. Cohn, J. J. Neumeier and C.C. Popoviciu, *Phy. Rev. B.*, **56**, 56 (1997)
31. J. M. D. Coey, M. Viret, L. ranno and K. Ounadjela , *Phys. Rev. Lett.*, **75**, 3910 (1995)

Chapter 6

Thermal transport properties of $\text{ZnAl}_2\text{O}_4\text{-TiO}_2$ (ZAT) Ceramics

6.1 INTRODUCTION

All of us know that ceramic metal packages are extensively used for interconnections and environmental protection of active devices such as diodes and transistors. Since the inception of these packages, the number of applications has grown to such an extent that they are now also utilized for interconnections, substrate fabrication, power distribution, cooling, inputs, outputs and engineering changes. In the future, growth of the electronic industry will place new and even more demanding requirements for improved materials and processes. These needs will probably be greatest in the computer field, where the cost per computation will have to be reduced to handle the large amounts of data and their manipulation in the central processor [1-5].

The packaging of integrated circuits requires knowledge of ceramics and metals to accommodate the fabrication of modules that are used to construct subsystems and entire systems from extremely small components. The electronic component is the smallest replaceable element in the system [6]. The use of ceramics in electronic packaging has advanced to very sophisticated levels of science and engineering. The first applications were to substrates, which were needed to start the emerging microelectronics era. These technologies were used to create the next generation of packages. New materials and processes had to be developed to build these ceramic modules. The first substrates were made with steatite ceramics which were sintered in

air at temperatures in the range of 1200^o C-1350^o C. These substrates were metalized with various pastes, such as gold, silver, palladium and platinum. The steatite ceramics were soon replaced with alumina materials [18] and were metalized with Mo, W and Mo-Mn pastes. The latter three pastes had to be sintered in the reducing atmospheres. Eventually the alumina ceramics could be confired with these pastes.

The three main alumina materials [19] currently in use are listed with their properties in Table 6.1. Alumina is chosen because of its high strength and good thermal conductivity. But it has high dielectric constant and thermal expansion than silicon. So it has to be replaced with other ceramic materials. The NEC 55% Al₂O₃ and 45% glass does have a thermal expansion near that of silicon but it still has a high dielectric constant and low thermal conductivity. Therefore the need for developing other ceramic materials [20] to replace alumina has been very high. Aluminium nitride (AlN) is one such kind of material. It has strength close to that of alumina, a high thermal conductivity and an expansion close to that of silicon. But the processing of AlN has to be done at higher temperature, above 1800^oC, in nitrogen atmosphere. And also it has to be hot pressed at temperatures above 1600^oC. Also it will get oxidized and subsequently lose its substrate properties [13].

Another potential substrate material is silicon nitride, which has a high strength, matching thermal expansion to that of silicon, a low dielectric constant and low thermal conductivity. Its high strength will allow it to resist stresses in ceramic caused by various metals [14, 15]. However, it must also be sintered or hot pressed at high temperatures, above 1700^oC.

Table 6.1. Alumina materials showing their properties

Ceramic	Dielectric constant	Thermal conductivity (W/m °C)	Thermal expansion (ppm / °C)
96% alumina, 4% glass	10.2	20.9	7.1
92% alumina, 8% glass	9.5	16.7	6.9
55%alumina, 45% glass	7.5	4.2	4.2

Another material used for these applications is beryllium oxide (BeO). It has got a low dielectric constant and small thermal expansion characteristic. It is used in many high-performance semiconductor parts for applications such as radio equipment because it has good thermal conductivity while also being a good electrical insulator. Some power semiconductor devices have used beryllium oxide ceramic to insulate the silicon chip from the metallic mounting base of the package in order to achieve a low thermal resistance value than for a similar construction made with aluminium oxide [16, 17]. But Beryllia is a toxic material which constraints its wide commercial use as a packaging substrate. Glass ceramic materials such as cordierite , forsterite etc. have low strengths and low thermal conductivities.

In this perspective the development of alternative low loss ceramic substrates always catches attention as a substitute for the existing conventional ceramic insulators that are used in microelectronic packaging. Very recently Surendran et.al.[21] successfully developed a low dielectric constant, low loss substrate dielectric in the spinel-rutile system $0.83\text{ZnAl}_2\text{O}_3-0.17\text{TiO}_2$

(ZAT). This specific composition was selected for further investigation since its resonant frequency is , by and large independent of the temperature variations in the range of 20-80°C. In this present work we explored the adaptability of this material for possible application in microelectronic industry as substrates and packaging materials. In this study, the most important thermal characteristic of a substrate viz thermal conductivity is investigated.

The details of preparation of ZAT samples, measurements done, results obtained and a discussion of the results are presented in this chapter.

6.2 SAMPLE PREPARTION

The cermaic baed on ZAT specimens were prepared following solid-state reaction method. High-purity ZnO and Al₂O₃ (purity 99.9%; Aldrich chemical Co.) were used as the starting materials for the synthesis of ZnAl₂O₃ spinels. The homogenized mixture was calcined at 1100° C for 4 hours. It was then ball milled with anatase TiO₂ (Aldrih 99.9% pure) according to the formula 0.83ZnAl₂O₃-0.17TiO₂ for 24 hours using de-ionized water as the mixing medium. The finely crushed powder was then granulated and pressed into cylindrical disks of about 1-2 mm diameter. These compacts were sintered and thermally etched samples were used to measure the thermal properties by PPE methode. The samples were cut using a diamond wheel saw and optically polished to a thickness of about 0.5mm. -The density of the samples determined from the volume and weight.

(The spinels are a group of oxides that have very similar structures. The spinel group contains over twenty members, but only a few are considered common. Named after their sole gemstone representative, spinel is an important group of minerals. It includes one of the most important ores of iron, magnetite; an important ore of chromium, chromite, an important ore of lead, minium; a once important ore of manganese, iron and zinc; franklinite

and many other interesting members. The general formula of the Spinel Group is AB_2O_4 , where A represents a divalent metal ion such as Magnesium, Iron, Nickel, Manganese and/or Zinc. The quad valent lead ion can also occupy this site. B represents trivalent metal ions such as Aluminum, Iron, Chromium and/or Manganese, Titanium may also occupy this site with a +4 charge and lead at +2 can occupy this site. Solid solutioning is common in this group of minerals, meaning that they may contain certain percentages of different ions in any particular specimen. Fig.6.1. shows the diagrams of the spinel (Al) and $R-Al_2O_3$ crystals.

The structure of spinel is based on the structure of diamond, which has the same high symmetry, $4/m\bar{3}2/m$. The position of the A ions is nearly identical to the positions occupied by carbon atoms in the diamond structure. This could explain the relatively high hardness and high density, typical of this group. The arrangement of the other ions in the structure conforms to the symmetry of the diamond structure. But, they disrupt the cleavage as there are no cleavage directions in any member of this group. The arrangement of the ions also favors the octahedral crystal habit which is the predominant crystal form and is in fact the trademark of the spinels. All members of this group that share the spinel structure show the same type of twinning that is named after spinel, called the *Spinel Law*).

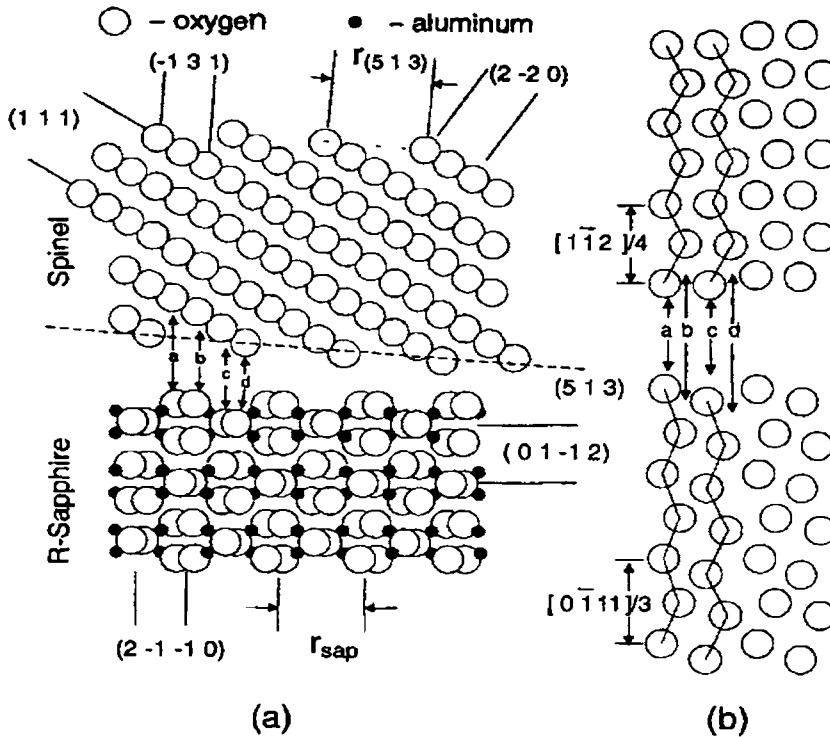


Fig.6.1: Schematic diagrams of the spinel (Al_2O_3) and $R-Al_2O_3$ crystals
(a) view along the $[011]$ axis of Al_2O_3 and
(b) top view of the arrangement of the bottommost layer of oxygen ions in the spinel and the topmost layer of oxygen ions in Al_2O_3

6.3 EXPERIMENTAL METHOD

The photopyroelectric method described in the earlier chapters has been used to determine the thermal properties of ZAT. For this measurement the sample dimensions should be such that the sample, the pyroelectric detector and the backing material should be thermally thick during the whole measurement. Photopyroelectric measurements have been carried out on the samples following the method already described in Chapter 2. The thermal thickness of ZAT sample has been verified by plotting the PPE amplitude and phase with frequency at room temperature. Since the optical absorption

in ZAT is low, a light coating of carbon black is provided on the face of the sample to enhance optical absorption and thermal wave generation.

Measurement of the PPE signal phase and amplitude enables one to determine thermal diffusivity (α) and thermal effusivity (e) respectively. Principles of this method and experimental procedures are described in detail before. From the measured values of α and e , the thermal conductivity k and specific heat capacity c_p of the samples are determined, knowing density ρ , using the following relations [22].

$$k = e [\alpha]^{1/2} \quad (1)$$

$$c_p = e / [\rho[\alpha]^{1/2}] \quad (2)$$

The calibration of the experimental set up has been done with known samples prior to carrying out the measurements.

The variations of the detected signal amplitude and phase using a lock-in amplifier as a function of frequency for ZAT samples at room temperature are shown in Fig.6.2, Fig.6.3 and Fig.6.4. In these measurements the sample has been cut and polished to such a thickness that the sample and the PVDF film detector are thermally thick at all the modulation frequencies used. We made measurements on three pieces of the ZAT samples which have got different thickness. These samples are designated as ZAT I, ZAT II and ZAT III.

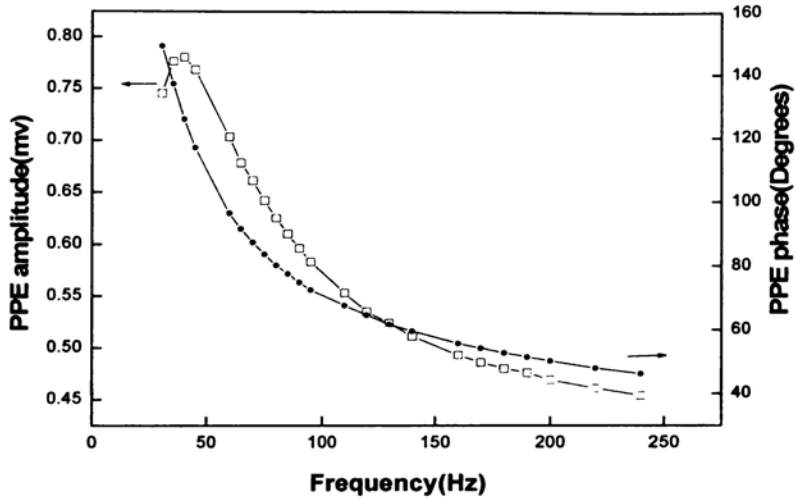


Fig. 6.2: variation of PPE amplitude and phase with modulation frequency for ZAT I

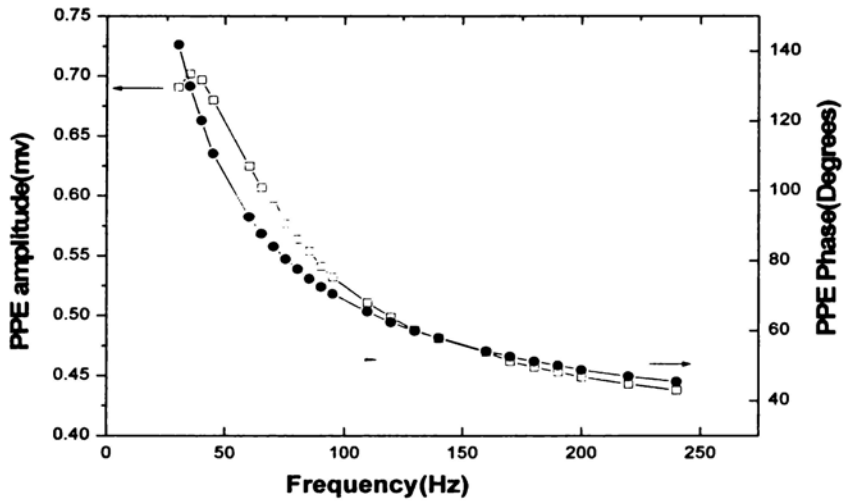


Fig. 6.3: variation of PPE amplitude and phase with modulation frequency for ZAT II

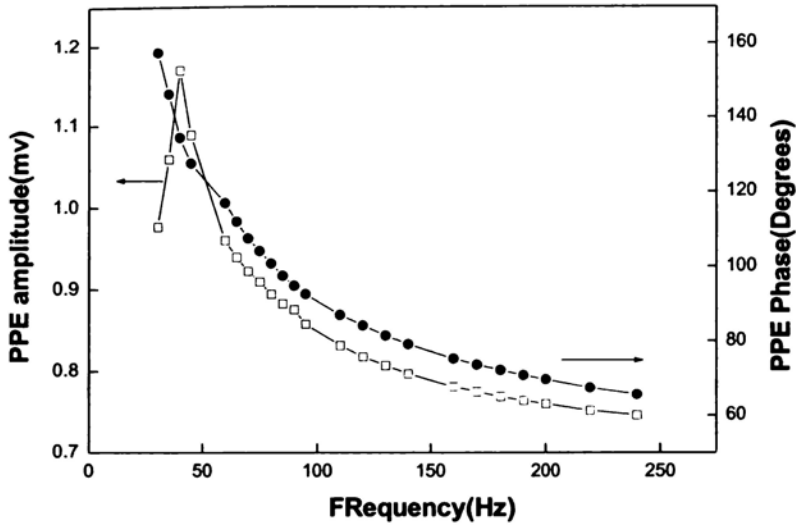


Fig. 6.4: variation of PPE amplitude and phase with modulation frequency for ZAT III

6.4 RESULTS AND DISCUSSION

From the amplitude and phase values of the photopyroelectric signal obtained we have calculated the thermal transport properties, thermal diffusivity (α), thermal effusivity (e), specific heat capacity (c_p) and thermal conductivity (k), for the three typical samples ZATI, ZAT II and ZAT III. The values obtained were tabulated in Table 6.2.

For all the measurements the chopping frequency used was 75Hz. The thermal conductivity of ZATII and ZAT III are obtained as $59 \text{ Wm}^{-1}\text{K}^{-1}$, while that of ZAT I is $55 \text{ Wm}^{-1}\text{K}^{-1}$. It should be remembered that even though all the three specimens used in the present investigation are prepared

through the same conventional mixed oxide route, the density and thickness vary slightly from sample to sample. The thermal conductivity of ZAT I is comparatively lower because of its lower densification. Table 6.3 gives a comparison of the important substrate properties of some commercially important substrate materials [24, 29]. It is evident from the table that the measured thermal conductivity of ZAT is about three times the value of alumina substrates [25]. A thorough evaluation [27, 28] of the thermal conductivity of synthetic materials reveal that most of the high thermal conductivity materials are diamond like compounds (such as BN, SiC, BeO, BP, AlN, BeS, GaN, Si, AlP, and GaP) which require stringent reducing atmospheres for their synthesis but the present material is easier to synthesize. It is worthwhile to note that contributing phases in the mixture, given by zinc aluminate (with face-centered cubic symmetry group $Fd\bar{3}m$) and rutile (with tetragonal symmetry group $P4_2/mnm$), show relatively lower thermal conductivities ($<12 \text{ Wm}^{-1}\text{K}^{-1}$) [26]. The unusually high thermal conductivity of ZAT could possibly be due to the composite like behavior of this material.

Table 6.2 Thermal Transport Properties of different ZAT samples

Sample code	Thickness (mm)	Density g/cm ³	Thermal diffusivity cm ² /s	Thermal effusivity Jcm ⁻² K ⁻¹ s ^{-1/2}	Specific heat capacity Jg ⁻¹ K ⁻¹	Thermal conductivity Wm ⁻¹ K ⁻¹
ZATI	0.65	4.39	0.33±0.03	0.96±0.04	0.37±0.01	55.1±0.1
ZATII	0.67	4.47	0.34±0.02	1.012±0.03	0.38±0.03	59.2±0.3
ZATIII	0.55	4.47	0.37±0.02	0.97±0.04	0.36±0.04	59.4±0.4

Table 6.3. Comparison of properties of ZAT with commercial substrates

Substrate	Density g/cm ³	Dielectric constant	Loss factor (at frequency) x10 ⁻³	Thermal conductivity Wm ⁻¹ K ⁻¹	Coefft. of thermal expansion (ppm/°C)	Reference
Alumina (Al ₂ O ₃)	3.97	8.9	0.2 (1MHz)	20	6.7	15&16
AlN	3.26	8.8	0.1(1MHz)	290	4.6	12&16
BeO	2.91	6.5	0.5 (1MHz)	250	7.5	16
ZAT	4.47	12.7	0.1(10GHz)	59	6.3	17

1. J. Ann, B. Schwartz and D. L. Wilcox, *U. S. Patent* **3**, 838 (1974).
2. D. Balderes and M.L. White, *Package Effects on CPU Performance of large commercial Processes*, Proc. Elect. Comp. conf., Washington, D.C., **20**, 351 (1985).
3. A. J. Blodgett, Jr. *Proc. Electron. Comp. Conf., San Francisco, California IEEE*, **30**, 283 (1980).
4. A.J. Blodgett, Jr. and D.R. Barbour. *J. Res. Dev.*, **26**,30 (1982).
5. W. G. Burger and C. W. Weigel., *J.Res.Dev*, **27**, 11 (1983).
6. D.A. Chance, *Met. Trans.*, **1**, 685 (1970).
7. D.A. Chance and D.L. Wilcox. ,Proc. IEEE 1455 (1971).
8. R. C. Chu, U.P. Hwang and R.E. Simons, *J.Res.Dev.*, **26**, 45 (1982).
9. N. Claussen, *Mater. Sci. eng.*, **71**, 23 (1985).
10. E. M. Davis, W. E. Harding, R. S. Schwartz and J. J. Corning, *J. Res. Dev.*, **8**, 109 (1964)
11. L. S. Goldmann, *J. Res. Dev.*, **13**, 251 (1969).
12. L.F. Miller, *J. Res. Dev.*, **13** , 239 (1969).
13. T.C. Rutt, *U.S. Patent* **3**, 679, 950 (1972).
14. B. Schwartz, *Elect. Ceram.* **3**, 12 (1969).
15. B. Schwartz, *Bull. Am. Ceram. Soc.*, **63** ,577 (1984a).
16. B. Schwartz, *J. phys. Chem. Solids*, **45**, 1051 (1984b).
17. H. Stetson, *U.S. Patent* **3**, 189, 978 (1965)
18. D.S. Morgan, *Electronic Packaging, Electronic Materials Handbook Vol. 1*, (American Society for Metals, Metals Park, OH, 1989).
19. R. C. Buchanan, *Ceramic Materials for Electronics* (Marcel Dekker, New York, 1996)

-
20. K. M. Nair, *Dielectric Materials and Devices* (American Ceramic Society, Columbus, OH, 2002).
 21. K. P. Surendran, N. Santha, P. Mohanan, and M. T. Sebastian, *Eur. Phys. J. B*, **41**, 301 (2004).
 22. C. P. Menon and J. Philip, *Meas. Sci. Technol.* **11**, 1744 (2000).
 23. M. Marinelli, F. Murtas, M. G. Mecozzi, U. Zammit, R. Pizzoferrato, F. Scudieri, S. Martellucci, and M. Marinelli, *Appl. Phys. A: Solids Surf.* **51**, 387 (1990).
 24. M. T. Sebastian, C. Preethy Menon, J. Philip, and R. W. Schwartz, *J. Appl. Phys.* **94**, 3206 (2003).
 25. G. A. Slack, R. A. Tanzilli, R. O. Pohl, and J. W. Vandersande, *J. Phys. Chem. Solids* **48**, 641 (1987).
 26. A. M. Hofmeister, *Am. Mineral.* **86**, 1188 (2001).
 27. D. R. Frear, *JOM*, **51**, 22 (1999).
 28. S. J. Mumby, *J. Electron. Mater.* **18**, 241, (1989).
 29. Internet Data www.microwaves101.com/hardsubstratematerials

Chapter 7

Thermal transport properties of Polytetrafluoroethylene/Sr₂Ce₂Ti₅O₁₆ Polymer/Ceramic Composites

7.1 INTRODUCTION

The effectiveness with which an electronic system performs its electrical functions as well as reliability and cost of the system, are strongly determined not only by electrical design, but also by the packaging materials. Electronic packaging refers to the packaging of integrated circuit (IC) chips (dies), their interconnections for signal and power transmission and heat dissipation. Packaging is also required for electromagnetic interference (EMI) shielding. In electronic systems, packaging materials may also serve as electrical conductors or insulators which provide structure and thermal paths, and protect the circuits from environmental factors such as moisture, contamination, hostile chemicals and radiation. As the speed and power of electronics increase, the heat dissipation problems and the signal and the signal delay caused by the capacitive effect of the dielectric material become even greater issues that need to be resolved [1-5]. The solution involves devising innovative packaging schemes and the continuing search for more advanced materials which suits the stringent requirements.

The levels of packaging or packaging architecture are often used to classify materials and required material characteristics for effective performance over time. The chip, component, printed wiring board and assembly level packaging are referred to as the zeroth, first, second and third

levels of packaging respectively. In general, each level has unique requirements on material properties. The actual applications of materials in electronic packaging include interconnections, printed circuit boards, substrates, encapsulants, interlays dielectrics, diattach materials, electrical contacts, connectors, thermal interface materials, heat sinks, solders, brazes, lids and housings [2-5].

Polymers and ceramics have extreme electrical, mechanical and thermal properties which make them suitable for use as packaging materials [4]. The electrical properties of microelectronic devices such as signal attenuation, propagation velocity and cross talk are influenced by the dielectric properties of packaging materials [2-5]. The dielectric constant of the composites cannot be increased beyond a certain value as it reduces the signal speed. Hence, for a composite material to be used in packaging and substrate applications there must be a compromise between signal speed and ϵ_r [2-4]. So for practical applications packaging materials must possess optimum dielectric constant, low dielectric loss, high thermal conductivity to dissipate heat and thermal expansion should be matching to that of silicon [1-4]. Hence, polymers filled with low loss ceramics are suitable for electronic packaging for device encapsulation and substrates.

Polytetrafluoroethylene (PTFE) has been extensively used in electronic substrates and packaging applications because of its excellent dielectric properties ($\epsilon_r = 2.1$ and $\tan \delta = 10^{-4}$ at 800 MHz) and chemical resistances [6, 7]. However, applications are limited as the polymer has low dielectric constant, low thermal conductivity ($0.265 \text{ W/m}^\circ\text{C}$) [8] and high coefficient of thermal expansion [9]. Recently, Chen et. al. [10] reported the dielectric properties of PTFE/SiO₂ composites. But the dielectric constant of the composite was as low as SiO₂ hence, the miniaturization of microwave devices by the use of PTFE/SiO₂ composites is limited. In a similar investigation Wang et al. [7] reported the dielectric properties of

$\text{Ba}_2\text{Ti}_9\text{O}_{20}$ /PTFE composites. More recently, Xiang *et al.* investigated the dielectric properties of composites involving PTFE and low loss, high ϵ_r ($\epsilon_r = 94$ at 800 MHz) Bi_2O_3 - ZnO - Nb_2O_5 ceramics. However, incorporation of high amounts of ceramics leads to poor process ability of the composites. Therefore, to improve the process ability of the composites, low loss ceramics with high dielectric constant are preferred, since addition of small amounts of such ceramics can increase the dielectric constant significantly.

Even though metals have a high thermal conductivity, they cannot be used as fillers because they affect the dielectric properties of the composites adversely. Hence, ceramics with low thermal expansion coefficients, high thermal conductivities, and low dielectric losses are the preferred fillers. $\text{Sr}_2\text{Ce}_2\text{Ti}_5\text{O}_{16}$ is a high dielectric constant, low-loss [11] material with a very low coefficient of thermal expansion (1.72 ppm/ $^{\circ}\text{C}$) and a moderate thermal conductivity.

In order to understand the influence of ceramics on the thermal properties of PTFE, PTFE/ $\text{Sr}_2\text{Ce}_2\text{Ti}_5\text{O}_{16}$ polymer-ceramic composites have been prepared and photopyroelectric measurements have been carried out on them. In this chapter we report the thermal properties of PTFE/ $\text{Sr}_2\text{Ce}_2\text{Ti}_5\text{O}_{16}$ polymer ceramic composites measured using photopyroelectric technique.

7.2 SAMPLE PREPARATION

$\text{Sr}_2\text{Ce}_2\text{Ti}_5\text{O}_{16}$ ceramics were prepared by the solid-state ceramic route. High-purity SrCO_3 and TiO_2 (99.91%, Aldrich Chemical Co., Inc.) and CeO_2 (99.99%, Indian Rare Earths, Ltd.) were used as the starting materials. Stoichiometric amounts of ceramic powders were ball-milled in a distilled water medium with yttria-stabilized zirconia balls in plastic container for 24 h. The slurry was dried and calcined at 1300 $^{\circ}\text{C}$ for 5 h. The calcined material was ground into a fine powder. $\text{Sr}_2\text{Ce}_2\text{Ti}_5\text{O}_{16}$ / PTFE (Hindustan Fluorocarbons) composites were prepared by powder processing technology.

To create an active surface for binding with the polymer, the fine powder of $\text{Sr}_2\text{Ce}_2\text{Ti}_5\text{O}_{16}$ was mixed with an acrylic acid solution for 1 h and dried [7]. Acrylic acid is a well-known polymerizing agent. The dried powder was again treated with 2 wt % tetra butyl titanate. The uses of titanate-based coupling agents provide excellent mechanical and electrical properties compared to other organic functional coupling agents such as silane. The evaporation of the solvent gave $\text{Sr}_2\text{Ce}_2\text{Ti}_5\text{O}_{16}$ powders cladded with coupling agents.

The volume fraction (Φ) of the ceramics is given by

$$\Phi = V_2 / (V_1 + V_2) \quad (1)$$

where V_1 and V_2 are the volumes of PTFE matrix and $\text{Sr}_2\text{Ce}_2\text{Ti}_5\text{O}_{16}$ ceramic, respectively. Different volume fractions (0–0.6) of treated ceramics and PTFE powders were dispersed in ethyl alcohol with an ultrasonic mixer for about 30 min. A dried powder mixture was obtained by the removal of the solvent at 70°C under stirring. The homogeneously mixed PTFE/ $\text{Sr}_2\text{Ce}_2\text{Ti}_5\text{O}_{16}$ powders were then compacted under a uni-axial pressure of 50 MPa for 1 min. The cylindrical pellets thus obtained were kept at 310°C for 2 h and were then slowly cooled to room temperature.

7.3 EXPERIMENTAL METHOD

The improved photopyroelectric method [12, 13], as has been described in Chapter 2 of this thesis, has been used to determine the thermal properties of PTFE/ $\text{Sr}_2\text{Ce}_2\text{Ti}_5\text{O}_{16}$ polymer/ceramic composites. For this measurement the sample dimensions should be such that the sample, the pyroelectric detector and the backing material should be thermally thick during the whole measurement. The sample is illuminated with an intensity- modulated beam of light, which gives rise to periodic temperature variation in the sample by

optical absorption. The thermal waves so generated propagate through the sample and are detected with a pyroelectric detector.

A 120mw He-Cd laser of wavelength $\lambda = 442\text{nm}$ has been used as the optical heating source and the intensity modulation is done with a mechanical chopper (Model SR540). A PVDF film of thickness $28\mu\text{m}$, with Ni-Cr coating on both sides, with pyroelectric coefficient $P = 0.30 \times 10^{-8} \text{ Vcm}^{-1}\text{K}^{-1}$, is used as the pyroelectric detector. The output signal is measured with a lock-in amplifier (Model SR830). Modulation frequency is kept above 30Hz in all our experiments to ensure that the detector, the sample and the backing medium are all thermally thick during measurements. The thermal thickness of the sample has been verified by plotting the PPE amplitude and phase with frequency at room temperature. Since the optical absorption in the sample is low, a light coating of carbon black is provided on the face of the sample to enhance optical absorption and thermal wave generation. Block diagram of the experimental setup and other details are given in Chapter 2 of the thesis.

Measurement of the PPE signal phase and amplitude enables one to determine thermal diffusivity (α) and thermal effusivity (e) respectively. Principles of this method and experimental procedures are described in detail elsewhere [12]. From the measured values of α and e , the thermal conductivity k and specific heat capacity c_p of the samples are determined, knowing density ρ , using the following relations.

$$k = e [\alpha]^{1/2} \quad (2)$$

$$c_p = e/[\rho[\alpha]^{1/2}] \quad (3)$$

The calibration of the experimental set up has been done with known samples prior to carrying out the measurements.

The variations of the detected PPE signal amplitude and phase as a function of frequency for this sample for some volume fractions at room temperature are shown in Fig. 7.1, Fig.7.2, Fig.7.3, Fig.7.4 and Fig.7.5.

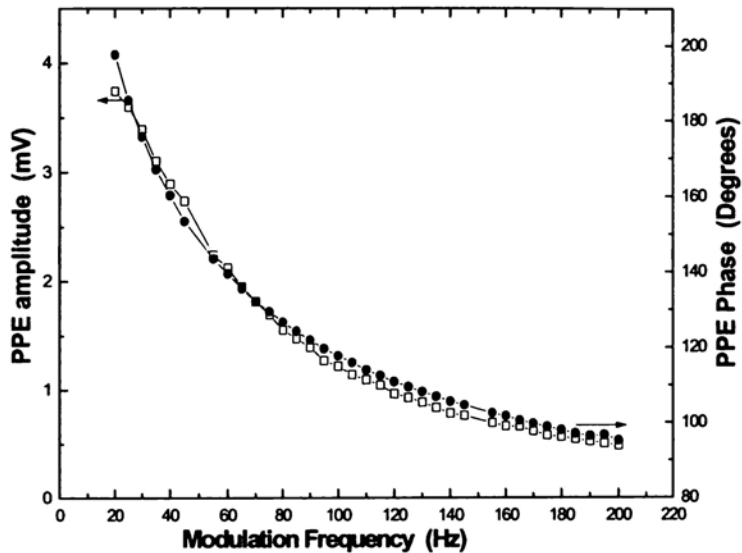


Fig.7.1 Variations of PPE amplitude and phase with frequency at room temperature for pure PTFE

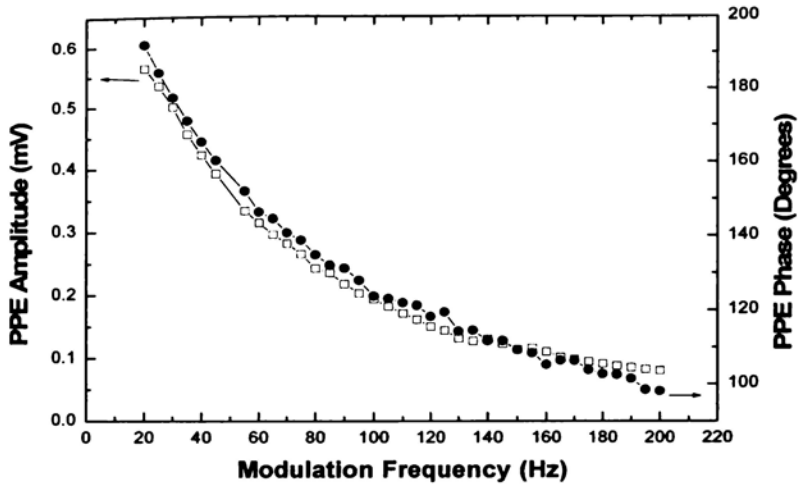


Fig.7.2 Variation of PPE amplitude and phase with frequency at room temperature for PTFE with a volume fraction 0.1% $\text{Sr}_2\text{Ce}_2\text{Ti}_5\text{O}_{16}$

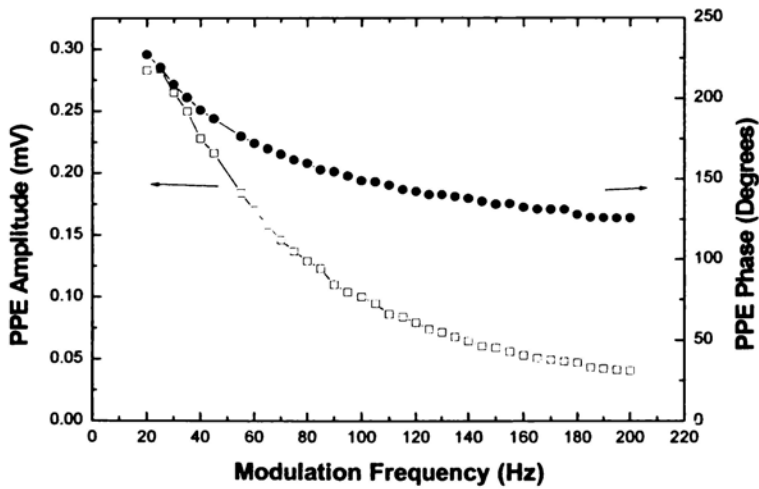


Fig.7.3 Variation of PPE amplitude and phase with frequency at room temperature for PTFE with a volume fraction 0.3% $\text{Sr}_2\text{Ce}_2\text{Ti}_5\text{O}_{16}$

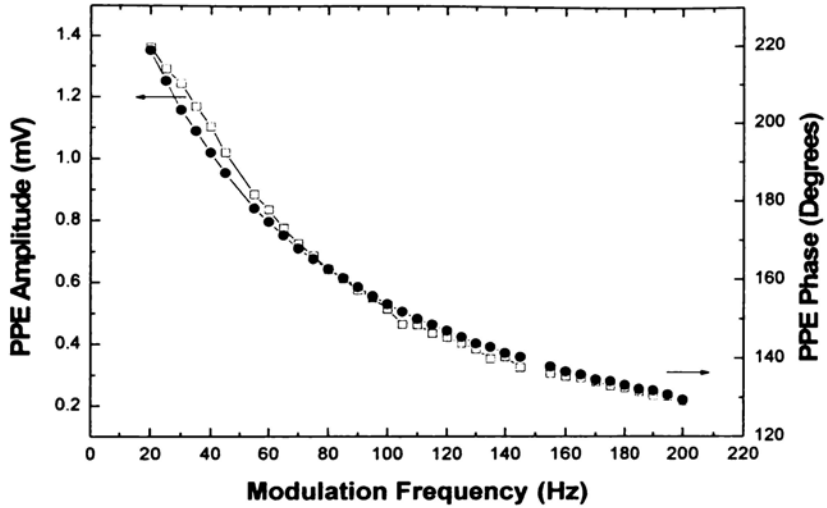


Fig.7.4 Variation of PPE amplitude and phase with frequency at room temperature for PTFE with a volume fraction 0.5% $\text{Sr}_2\text{Ce}_2\text{Ti}_5\text{O}_{16}$

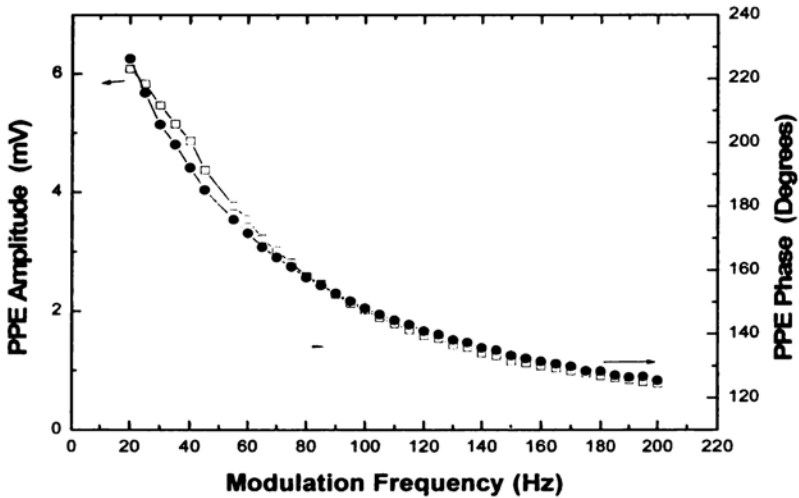


Fig.7.5 Variation of PPE amplitude and phase with frequency at room temperature for pure $\text{Sr}_2\text{Ce}_2\text{Ti}_5\text{O}_{16}$

7.6 RESULTS AND DISCUSSION

We present below a comprehensive set of results on the thermal transport properties of PTFE/ $\text{Sr}_2\text{Ce}_2\text{Ti}_5\text{O}_{16}$ polymer ceramic composites. The variations of thermal diffusivity (α), effusivity (e), thermal conductivity (k) and specific heat capacity (c_p) of the various samples are shown in Table 7.1, along with the mass density of each sample.

Figure 7.6 shows the experimental values of the thermal conductivities of PTFE/ $\text{Sr}_2\text{Ce}_2\text{Ti}_5\text{O}_{16}$ composites with different volume fractions. As the vf of $\text{Sr}_2\text{Ce}_2\text{Ti}_5\text{O}_{16}$ is increased, the thermal conductivity also increases. A sudden rise in the thermal conductivity is observed at 0.6 vf of the $\text{Sr}_2\text{Ce}_2\text{Ti}_5\text{O}_{16}$ composites. This is due to the presence of more connecting paths between the filler regions without disturbing the matrix. A similar observation was reported by Kim *et al.*[14] in Aluminium Nitride epoxy composites for 60 vol % AlN. The thermal conductivity of the PTFE/ $\text{Sr}_2\text{Ce}_2\text{Ti}_5\text{O}_{16}$ improved from 0.283 to 1.7 W/mK for the PTFE/0.6-vf $\text{Sr}_2\text{Ce}_2\text{Ti}_5\text{O}_{16}$ composite. The effective thermal conductivity of a composite is strongly affected by its composition, structure, intrinsic thermal conductivity, filler particle size, shape, and interfacial thermal resistance. The interfacial thermal resistance has a significant effect on the thermal conductivity of a composite [15, 16]. It arises from the combination of poor mechanical or chemical adherence at the interface and a mismatch in coefficient of thermal expansion [16].

Figure 7.7 shows the variations in the specific heat capacity and thermal diffusivity of the composite PTFE/ $\text{Sr}_2\text{Ce}_2\text{Ti}_5\text{O}_{16}$. with the vf of the ceramic in the composite. It increases with increasing filler content. A similar observation has also been made by Aravind *et.al.* [17] in lead titanate/polyvinylidene fluoride. The specific heat capacity of the PTFE/ $\text{Sr}_2\text{Ce}_2\text{Ti}_5\text{O}_{16}$ composites decreases with increasing ceramic content.

Table 7.1 values of thermal diffusivity (α), effusivity (e), thermal conductivity (k) and specific heat capacity (c_p) of PTFE/ $Sr_2Ce_2Ti_5O_{16}$ polymer ceramic composites with different volume fractions (vf)

Sample Code	Density g/cm^3	Thickness of the sample $\times 10^{-3} cm$	Thermal Diffusivity $\times 10^{-3} cm^2/s$	Thermal Effusivity $J/cm^2 K^{-1} s^{-1/2}$	Specific Heat capacity J/gK	Thermal Conductivity $\times 10^{-3} W/cmK$
Pure PTFE	2.189	57.8	1.351	0.07701	0.9571	2.83 ± 0.01
PTFE+0.1Volume Fraction of $Sr_2Ce_2Ti_5O_{16}$	2.523	53.5	3.38	0.0765	0.5215	4.45 ± 0.01
PTFE +0.2Volume Fraction of $Sr_2Ce_2Ti_5O_{16}$	2.781	55.3	4.87	0.0761	0.363	5.31 ± 0.01
PTFE +0.3Volume Fraction of $Sr_2Ce_2Ti_5O_{16}$	3.004	64.2	.25	0.0724	0.3326	6.24 ± 0.01

PTFE +0.4Volume Fraction of $\text{Sr}_2\text{Ce}_2\text{Ti}_5\text{O}_{16}$	3.329	54.1	6.271	0.0644	0.2443	7.09 ± 0.01
PTFE +0.5Volume Fraction of $\text{Sr}_2\text{Ce}_2\text{Ti}_5\text{O}_{16}$	3.352	65.7	6.47	0.0457	0.2094	8.68 ± 0.01
PTFE +0.6Volume Fraction of $\text{Sr}_2\text{Ce}_2\text{Ti}_5\text{O}_{16}$	3.506	7.1	7.45	0.0325	0.1973	17.2 ± 0.01
Pure $\text{Sr}_2\text{Ce}_2\text{Ti}_5\text{O}_{16}$	4.931	63.2	9.56	0.0299	0.1671	29.25 ± 0.01

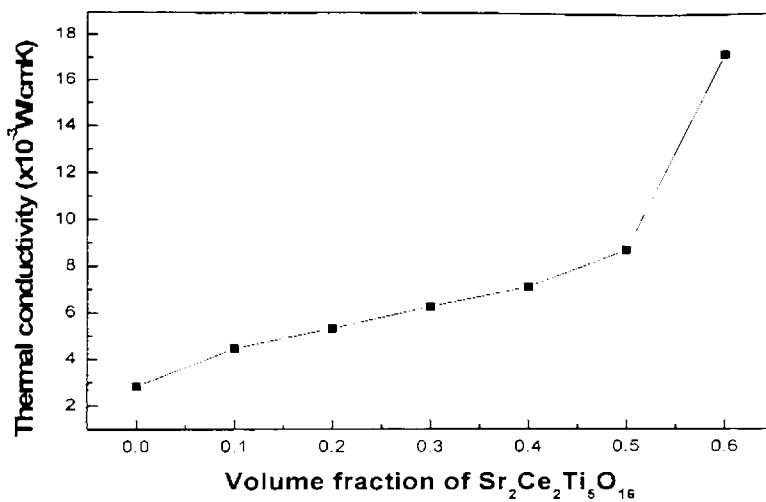


Fig. 7.8: Variation in the thermal conductivity of PTFE/Sr₂Ce₂Ti₅O₁₆ composites with volume

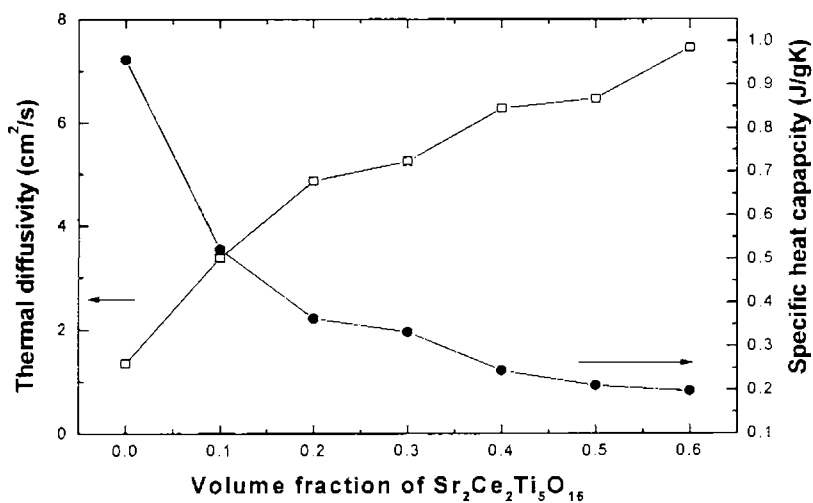


Fig. 7.9: Variation in the specific heat capacity and thermal diffusivity of the PTFE/Sr₂Ce₂Ti₅O₁₆ composites with volume

7.7 REFERNCES

1. M. G. Pecht, R. Agarwal, P. McCluskey, T. Dishongh, S. Javadpour, R. Mahajan. *Electronic Packaging Materials and Their Properties*; CRC: London, Chapter 1 (1999).
2. D. D. L. Chung, *Materials for Electronic Packaging*; Butterworth-Heinemann: Washington, DC, Chapter 1 (1995)
3. R. R. Tummala, *J. Am. Ceram. Soc.*, **74**, 895 (1991)
4. J. D. Bolt, D. D. Button, B. A. Yost, *Mater. Sci. Eng. A* **109**, 207 (1989)
5. D. D. L. Chung, *Appl. Therm. Eng.* **21**, 159 (2001)
6. J. A. Bur, *Polymer* **26**, 963 (1985)
7. F. Xiang, H. Wang, X. Yao, *J. Eur. Ceram Soc* **26**, 1999 (2006)
8. D. M. Price, M Jarralt, *Thermochim. Acta.* **392**, 231 (2002)
9. C. Y. Chen, C. H. Lin, D. Y. Lee, *J Polym. Res.* **10**, 247 (2003)
10. Y. M. Wang, D. C. Jia, and Y. Zhou, *Piezoelectrics Accoustooptics*, **24**(3), 225 (2002)
11. G. Subodh, C. Pavithran, P. Mohan and M. T. Sebastian, *J Eur Ceram Soc.*, **27**, 3039 (2007)
12. C.P. Menon And J. Philip, *Meas. Sci. &Tech.* **11**, 1744 (2000)
13. M. Marinelli, F.P. Murtas, M.G. Mecozzi, U. Zammit, R. Pizzoferrato, F. Scudierri, S. Maerwillucci, And M. Marinelli, *Appl. Phys. A: Solid Surf.* **51**, 387 (1990)
14. W. Kim, J. W. Bae, D. Choi, S. K. Yong, *Polym. Eng. Sci.* **39**, 756 (1999)
15. C. W. Nan, X. P. Li, R. Birringer, *J. Am. Ceram. Soc.* **83**, 848 (2000)
16. D. P. H. Hasselman, L. F. Johnson, *J. Compos. Mater.* **21**, 508 (1987)
17. M. Aravind, C. W. Ong, H. L. W. Chan, *Polym. Compos.* **23**, 925 (2002)

Chapter 8

Summary and Conclusions

A complete characterization of thermal properties of a material requires the determination of thermal properties such as thermal diffusivity, thermal effusivity, thermal conductivity and heat capacity. Simultaneous determination of thermal conductivity and heat capacity, as a function of temperature would be highly informative since it would allow studies of critical behaviours of thermal parameters when the material undergoes a phase transition. The work in this thesis deals with the characterization of thermal transport properties of different type of materials such as crystals, materials showing GMR properties and dielectrics.

The photopyroelectric (PPE) technique involves measurements of the temperature increase of a sample due to the absorption of radiation by placing a pyroelectric detector in thermal contact with the sample. The photopyroelectric technique has a number of advantages over other temperature detection techniques, such as its extreme simplicity, good sensitivity and non-destructive probing ability. PPE spectroscopy is less complex and less expensive than photoacoustic and photothermal deflection spectroscopies. In PPE measurements, the sample is heated by a modulated light beam on one side, and a pyroelectric detector detects the temperature oscillations on the opposite side of the sample.

In this thesis, we have taken up work on photopyroelectric investigation of thermal parameters of ferroelectric crystals such as Dicalcium lead propionate ($\text{Ca}_2\text{Pb}(\text{C}_2\text{H}_3\text{COO})_6$), Potassium selenate (K_2SeO_4) mixed valence perovskites samples such as $\text{La}_{1-x}\text{Te}_x\text{MnO}_3$ ($x= 0, 0.1, 0.15, 0.2$) which shows GMR properties and two dielectric ceramics named $0.83\text{ZnAl}_2\text{O}_3\text{-}0.17\text{TiO}_2$ (ZAT) and PTFE/ $\text{Sr}_2\text{Ce}_2\text{Ti}_5\text{O}_{16}$.

The ferroelectric crystals are grown by the well known slow evaporation technique. The Dicalcium lead propionate crystal show phase transitions at 191K which is a structural one and at 333K which is ferroelectric phase transitions. Both these transitions are reflected in the DSC measurements also. For the complete thermal characterization of this particular sample TG/DTA measurements are also taken and FTIR measurement gives the informations about the bonds formed in the formation of the crystal. The Pottassium selenate crystal is another ferroelectric crystal which under goes incommensurate phases transition in a region 93K to 129.5K. Below 93 K it is ferro electric and again it undergoes a phase transition at 745K which is a structural one. This phase transition is identified using the DSC measurement and the specific heat capacity at this transition temperature is calculated.

Thermal properties of the $\text{La}_{1-x}\text{Te}_x\text{MnO}_3$ ($x= 0, 0.1, 0.15, 0.2$) are studied by varying the magnetic field as well as temperature. We have been quite successful in finding out the nature of anomaly associated with thermal properties when the sample undergoes para to ferromagnetic phase transition under magnetic field. The structure of these materials is confirmed with XRD measurements and the transitions of these materials are also confirmed with

DSC measurements. The thermal properties of the two dielectric samples which can be used in electronic packaging are also measured using the PPE technique.

In summary, we have carried investigations of the variations of the thermal parameters during phase transitions employing photopyroelectric technique. The results obtained on different systems are important not only in understanding the physics behind the transitions but also in establishing the potentiality of the PPE tool. The full potential of PPE technique for the investigation of optical and thermal properties of materials still remains to be taken advantage of by workers in this field. There is lot of scope for doing good work to get important results on the thermal properties of materials and development of instrumentation required in this area.

